Electrical Detection of the Spin Hall Effect in Ferromagnet-Semiconductor Heterostructures

A DISSERTATION
SUBMITTED TO THE FACULTY OF THE GRADUATE SCHOOL
OF THE UNIVERSITY OF MINNESOTA
BY

Eric Scott Garlid

IN PARTIAL FULFILLMENT OF THE REQUIREMENTS
FOR THE DEGREE OF
Doctor of Philosophy

June, 2010

© Eric Scott Garlid 2010
ALL RIGHTS RESERVED

Acknowledgements

I joined Paul Crowell's group in the summer of 2005. It did not take long for me to earn the nickname "honorary theorist" from some of my fellow group members. My undergraduate work at St. John's University had been predominantly theoretical, but the nickname mostly reflected my general inexperience with many rudimentary laboratory skills an experimentalist should have. One of those early weeks, Paul sat with me in the prep room and taught me how to solder wires to a connector and fit the heat shrink tubing. Paul is always willing to instruct his students, and he will meet them at whatever level they are at. His door is always open. If you have a physics question, he will take the time to explain the answer to you, or he will help you puzzle it through. These qualities make Paul an excellent advisor, and I am very grateful to have had the opportunity to work in his lab. Paul has a reputation for being something of a workaholic, but this only comes from the fact that he is passionate about and dedicated to his research. Paul has very high standards, but more importantly, he is committed to the success of his graduate students.

I owe a debt of gratitude to Xiaohua Lou, who was my mentor when I joined the group. He was instrumental in helping me get started in our lab and in the cleanroom. His efforts were responsible for the initial success of the electrical spin detection measurements. I owe many thanks to all of the other members of the Crowell group, especially Mike Erickson, Mun Chan, Te-Yu Chen, Chad Geppert, and Rob Compton. They were always happy to help troubleshoot problems or discuss physics, even if it was completely unrelated to their respective experiments.

The members of the Crowell group have been not only colleagues, but also friends. They provided a great deal of personal support and companionship over the years. I can only hope that in my future I will have the good fortune to work with people as talented and friendly as they have been. I feel confident leaving the future of the spin transport project in the very capable hands of Chad Geppert, who has shown himself to be both curious and dedicated to solving the frequent and often unexpected challenges that arise while doing research.

In addition to the members of the Crowell group, I have also had the pleasure of working directly with Qi Hu before he moved with Chris Palmstrøm to UCSB. All of the samples studied in my thesis were grown by Qi Hu. He has always been eager and excited to try new ideas, and he has been a great source of knowledge for material science concerns. Qi Hu has always grown new samples extremely rapidly when Palmstrøm's growth chamber has been up. When Palmstrøm's growth chamber is not up (which can be often), Qi Hu works even harder to bring it back online. It is unfortunate that future members of the Crowell group will not have the opportunity to work within a block of Palmstrøm's lab.

My many classmates have also been excellent friends over the years, especially Mike Erickson, Matt Loth, Tanner Schulz, Tom Kelley, Seth Cooper, Dan Sword, Steve Snyder, Jolene Johnson, and Feng Guo. We may have TA training and Jackson problems to thank in part for our initial bonds of friendship, but those bonds persisted as we all went off into our own research worlds. Your friendship has been invaluable to me. I am very disappointed that you will no longer be down the hall or up a few floors from me.

When I began searching for a job, the former members of the Crowell group were very quick to jump to my assistance. I would especially like to thank Xiaohua Lou, Rob Compton, Jooho Park, and Jonathan Strand. Jooho and I overlapped for only about a month, while he was frantically writing his thesis. Years later, when I was looking for a job, he was happy to discuss his work at Intel with me. Jonathan and I had never met, but he was equally happy to discuss his work experiences with me. Both Johoo and Jonathan were instrumental in helping me

prepare for job interviews. I hope that I will be in a position to offer similar assistance to the current and future members of the Crowell group.

Finally, I would like to thank my wife, Andreona Garlid. She is wonderful beyond words, and I am blessed to have her with me at my side in life. She has always supported and encouraged me, and she has believed in me at times when I felt uncertain. She has sacrificed a great deal for our family, and without her I would not have made it through. Her love and kindness have been a great inspiration to me. I have also been inspired, in ways they do not yet realize, by my daughter Temperance, born September 24th, 2008, and by my son, who is due on July 27th 2010. I must thank my parents for getting me to where I am today, and I hope that I will be as good a father to my children as my parents have been to me.

To Andreona Garlid, the love of my life.

Abstract

This thesis describes the effects of spin-orbit coupling on electron transport in Fe/ $In_xGa_{1-x}As$ heterostructures. Spin-orbit coupling is a relativistic phenomenon that couples the spin of an electron to its momentum by means of a momentum-dependent effective magnetic field. The spin-orbit coupling in bulk $In_xGa_{1-x}As$ is determined by measuring the direct spin Hall effect. In the direct spin Hall effect, an applied charge current induces a spin current due to spin-orbit coupling. The spin current flows in a direction that is perpendicular to the charge current, with a spin orientation that is perpendicular to the flow direction of both the charge current and the spin current. The spin Hall effect leads to an out-of-plane spin accumulation that is opposite in sign at opposite edges of the channel.

Lateral Fe/$In_xGa_{1-x}As$ devices are fabricated using standard semiconductor processing techniques. The interface between the Fe and $In_xGa_{1-x}As$ is a highly doped Schottky tunnel barrier for efficient electrical spin injection and detection. Measurements of the spin valve and Hanle effect are performed in the non-local geometry to confirm that the Fe electrodes are sensitive to spin polarization in the $In_xGa_{1-x}As$ channel and its dephasing by precession in an applied magnetic field. The spin accumulation due to the spin Hall effect is identified through the observation of a Hanle effect in the Hall voltage measured by pairs of ferromagnetic contacts at the channel edges. The data are fit using a model which includes spin diffusion, precession, and relaxation. We use the parameters determined from the fit to calculate the spin Hall conductivity. We find that the magnitude of the spin Hall conductivity is in agreement with models of the extrinsic SHE due to ionized impurity scattering. By analyzing the dependence of the spin Hall signal on channel conductivity we determine the contributions of both skew and side jump scattering to the total spin Hall conductivity. We calculate that the spin-orbit coupling parameter is larger than predicted by standard $\mathbf{k} \cdot \mathbf{p}$ perturbation theory.

Contents

Acknowledgements **i**

Abstract **ii**

List of Tables **vi**

List of Figures **vii**

1 Introduction to Electrical Spin Detection **1**

1.1 Introduction to Spintronics 1

1.2 Spin Dependent Transport 2

1.3 Non-Local Electrical Spin Detection 6

1.4 Experimental Details 10

1.4.1 Sample Growth and Fabrication 10

1.4.2 Experimental Setup 13

1.5 Non-Local Spin Valve and Hanle Measurements 18

1.6 Bias Dependence of Spin Injection 23

1.7 Bias Dependence of Spin Detection 26

1.8 Three Terminal Spin Detection 31

2 Spin-Orbit Coupling **35**

2.1 Introduction to Spin-Orbit Coupling 35

2.2 Spin-Orbit Coupling in the Vacuum 36

2.2.1 Spin-Orbit Coupling and the Hydrogen Atom 36
2.2.2 Spin-Dependent Scattering in Vacuum 38
2.3 Spin-Orbit Coupling in Solids 41
2.3.1 Semiconductor Band Structure 41
2.3.2 Spin-Orbit Coupling in GaAs and InAs 45
2.4 The Anomalous Hall Effect 48
2.5 Skew and Side-Jump Scattering 51

3 The Spin Hall Effect 55
3.1 The Family of Spin Hall Effects 56
3.2 The Inverse Spin Hall Effect 57
3.2.1 Optically Pumped Inverse Spin Hall Effect 57
3.2.2 All-Electrical Inverse Spin Hall Effect in Metals 58
3.2.3 All-Electrical Inverse Spin Hall Effect in Semiconductors . 60
3.3 The Direct Spin Hall Effect 64
3.3.1 Spin Orientation From the Direct Spin Hall Effect 66
3.3.2 Optical Measurement of the Direct Spin Hall Effect 67
3.4 All-Electrical Measurement of the Direct Spin Hall Effect 72
3.4.1 Device Design and Measurement Procedure 72
3.4.2 Background Subtraction and Fitting 75
3.4.3 Determining the Spin Hall Conductivity 84
3.4.4 Bias Dependence of the Spin Hall Conductivity 88
3.4.5 Temperature Dependence of the Spin Hall Conductivity . . 95

4 Intrinsic Effects and Future Spintronic Devices 97
4.1 Intrinsic Spin-Orbit Effects 97
4.2 Spin Field Effect Transistor Designs 103
4.3 A Path to Future Experiments 109

5 Summary 115

References **117**

Appendix A. Details of Spin Transport Device Fabrication **126**

A.1 Sample Preparation 126

A.2 Details of the Device Fabrication Procedure 127

Appendix B. Glossary **133**

B.1 List of Abbreviations 133

B.2 List of Symbols 135

List of Tables

1.1 Doping profile of samples in Fig. 1.10 and Fig. 1.12. 25
2.1 Semiconductor Parameters. 45
3.1 Fit parameters for σ_{SH} vs. σ_{xx}. 94
B.1 List of Abbreviatons 133
B.2 List of Symbols 135

List of Figures

1.1 Tunneling Magneto-resistance. 4
1.2 Conductivity Mismatch Model. 6
1.3 Non-Local Detection Scheme. 8
1.4 Schematic of Sample Structure. 11
1.5 Illustration of Device Fabrication Process. 14
1.6 Photomicrograph of a Non-Local Spin Transport Device. 15
1.7 Rotator Board Sample Mounts. 16
1.8 Block Diagram of Experimental Setup. 17
1.9 Non-local spin valve and non-local Hanle field sweeps. 20
1.10 Measured Spin Injection Bias Dependence. 24
1.11 Injection Bias Dependence Explanation. 27
1.12 Bias Dependence of Spin Detection Measurement Setup. 28
1.13 Bias Dependence of Spin Detection. 30
1.14 Dependence of ΔV_d on Drift Effects. 32
1.15 Three Terminal Hanle Measurements. 34
2.1 Spin-Orbit Coupling in the Hydrogen Atom. 37
2.2 Effective Spin-Orbit Magnetic Field. 39
2.3 Mott Scattering. 40
2.4 Zinc Blende Semiconductor Band Structure. 42
2.5 E_g for $In_{1-x}Ga_xAs$. 44
2.6 λ_{SO}^{eff} and g^* for $In_{1-x}Ga_xAs$. 47
2.7 Anomalous Hall Effect. 49

2.8 Temperature Dependence of ρ_{AH} and σ_{AH}. 50
2.9 Skew Scattering and Side-Jump Scattering. 53
3.1 Optically Pumped Inverse Spin Hall Effect. 59
3.2 All-Electrical Inverse Spin Hall Effect in Metals. 61
3.3 Fringe Fields and Local Hall Effects. 63
3.4 Vertical Device Geometry for Detecting iSHE. 65
3.5 Cartoon Representation of the Spin Hall Effect. 68
3.6 Optical Detection of the Direct Spin Hall Effect. 70
3.7 Position Dependence of the Direct Spin Hall Effect. 71
3.8 Device Geometry for Electrical Detection of the Direct Spin Hall Effect. 74
3.9 Expected Signal from dSHE Measurement. 75
3.10 Cartoon of Fringe Fields in dSHE Measurement Geometry 77
3.11 Removal of Background Voltages from dSHE Measurement. 78
3.12 Fitting of $P(B_y)$ for dSHE Measurement. 81
3.13 Cartoon of D'yakonov-Perel Spin Relaxation. 84
3.14 Dependence of τ_s on In Concentration. 85
3.15 Cartoon of Skew and Side-Jump Contributions. 88
3.16 Bias Dependence of the Spin Hall Signal. 89
3.17 Donor Impact Ionization. 91
3.18 Bias Dependence of σ_{SH}. 93
3.19 Temperature Dependence of the dSHE. 96
4.1 Intrinsic Spin-Orbit Effects. 100
4.2 Intrinsic Spin Hall Effect. 102
4.3 Datta and Das Spin Field Effect Transistor. 106
4.4 Resonant Spin Lifetime Transistor. 108
4.5 Calculated Band Structure for Proposed 2DEG Samples. 111
4.6 Calculated Band Structure for Proposed 2DEG Samples. 112
4.7 Proposed Device Geometry for 2DEG Samples. 114

Chapter 1

Introduction to Electrical Spin Detection

1.1 Introduction to Spintronics

Conventional MOSFET (Metal-Oxide-Semicondcutor Field Effect Transistor) technology utilizes the charge of the electron to perform information processing by using a gate electrode to modulate the resistance state of a semiconductor heterostructure. The current flow through the device is therefore controlled by the gate electrode, and the two device states lend themselves naturally to computation. The advancements in computational power over the past decades have largely come from the minimization of MOSFET feature sizes, thereby increasing the density of transistors on a chip. Although this approach has been quite successful, there are challenges on the horizon for the further minimization of MOSFET devices [1]. Power dissipation from leakage currents becomes increasingly problematic with decreasing feature size. In recent years, there has been a growing interest in the field of spintronics, which studies the electron's spin degree of freedom with an ultimate view toward using the spin state of the electron to perform information processing.

Although there are many challenges yet to be overcome, proposed spintronic

devices have the potential to out-perform both current and future MOSFET technology in a number of ways [2–4]. A successful spintronic device will require three properties: spin injection or generation, spin manipulation, and spin detection. This chapter will introduce a number of the fundamental concepts required to understand spin injection, transport, and detection in ferromagnet/semiconductor (FM/SC) heterostructures. Chapter 2 will introduce spin-orbit coupling, a relativistic effect which couples an electron's spin state to its velocity. Spin-orbit coupling allows for the generation and manipulation of an electron's spin state utilizing electric fields rather than magnetic fields. Chapter 3 will discuss electrical measurements of spin polarizations generated via the spin Hall effect, a phenomenon that results from spin-orbit coupling. Finally, Chapter 4 will explore potential future directions for the exploitation of spin-orbit coupling in spintronic devices.

1.2 Spin Dependent Transport

The field of spintronics has received a great deal of research interest since the discovery of the giant magnetoresistance effect (GMR) in 1988 [5, 6]. It was found that the resistance of a multilayer ferromagnet/normal metal/ferromagnet (FM/NM/FM) stack depended strongly on the relative orientation of the two ferromagnetic layers, and therefore the electron's spin state is important in determining the total resistance of the device. This effect can be understood qualitatively using a two spin channel resistance model. We define the total current as the sum of the spin up and spin down charge currents:

$$j_{tot} = j_{\uparrow} + j_{\downarrow}. \tag{1.1}$$

Because the effective resistances of the spin up and spin down bands in a ferromagnet are unequal, a charge current passing through a FM/NM interface will inject spin polarized electrons from the FM into the NM. When the two ferromagnetic layers are oriented anti-parallel, increased spin-dependent scattering at the

FM/NM interface causes the device resistance to go up. This scattering occurs due to the exchange interaction:

$$H_{exch} = J\mathbf{S}_1 \cdot \mathbf{S}_2, \tag{1.2}$$

where $\mathbf{S}$ is the spin of an electron and J is the exchange coupling. In a ferromagnet, $< \mathbf{S} > \neq 0$, so the exchange term must be added to the scattering potential. We will see later, in Chapters 2 and 3, that spin-dependent scattering can also result from the spin-orbit interaction, which involves only one spin.

Another effect closely related to GMR is tunneling magnetoresistance (TMR). As the name implies, TMR relies on the tunneling of electrons through an insulating layer placed between two ferromagnetic layers. In this case, the current flow depends directly on the density of states in the ferromagnets (see Fig. 1.1) [7]:

$$j^{\uparrow,\downarrow}_{FM1\rightarrow FM2} = \int T^{\uparrow,\downarrow}(E) N^{\uparrow,\downarrow}_{FM1}(E - eV_b) f(E - eV_b) N^{\uparrow,\downarrow}_{FM2}(E)(1 - f(E))dE, \tag{1.3}$$

where $T^{\uparrow,\downarrow}(E)$ is the tunneling probability for spin up or spin down electrons, $N^{\uparrow,\downarrow}_{FM}$ is the density of states in the spin up or spin down band in the ferromagnet, and $f(E)$ is the Fermi-Dirac distribution describing the fractional occupancy of the density of states. TMR devices can exhibit much larger magnetoresistance, because both $T^{\uparrow,\downarrow}(E)$ and $N^{\uparrow,\downarrow}(E)$ can lead to highly spin selective tunneling currents. Both GMR and TMR devices have been exploited for numerous commercial applications for several years. In particular, because the resistance depends on the orientation of the two ferromagnetic layers, these devices are well suited for non-volatile memory storage and are widely used in hard drive read heads and more recently MRAM. On the other hand, these devices are limited by the fact that a magnetic field is needed to change the state of the device, which leads to lower switching frequencies and higher switching powers.

Semiconductor spintronics seeks to combine the use of the spin degree of freedom to store information, as in GMR and TMR devices, with the high tunability of semiconductors by applying electric fields, as in MOSFET devices. The first challenge involved in building a useful semiconductor spin logic device is injecting

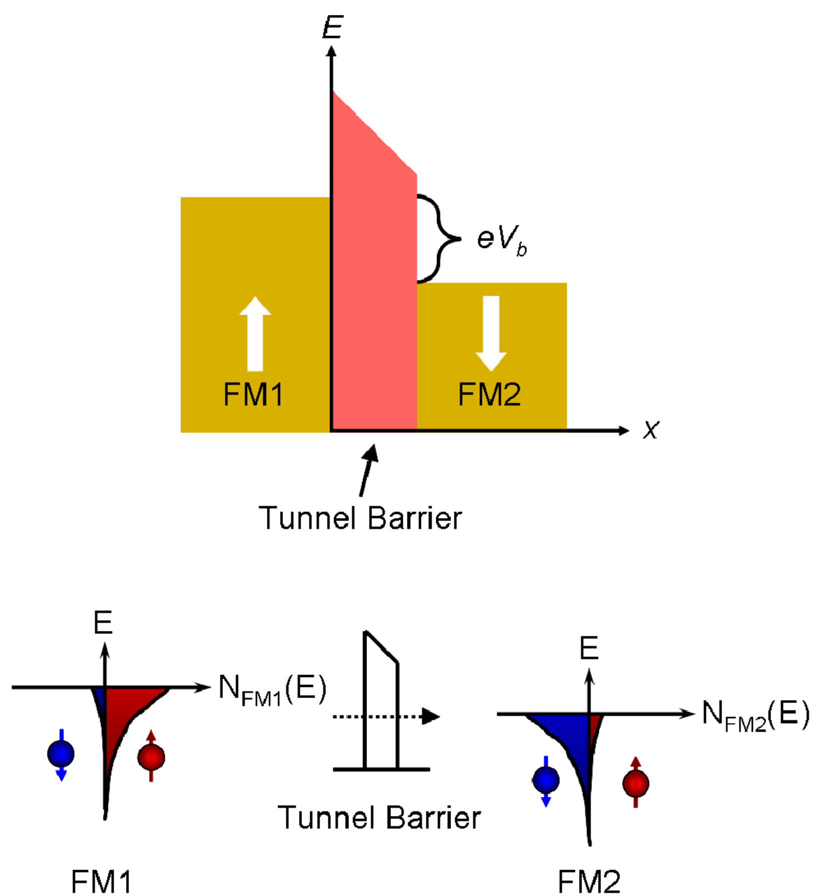

Figure 1.1: Schematic illustration of tunneling process leading to tunneling magnetoresistance. Electrons tunneling across an insulating barrier must retain their spin state, so a tunnel barrier placed between two ferromagnets leads to a large magnetoresistance.

spin polarized electrons into the semiconductor. A natural approach is to place a ferromagnetic metal on a semiconductor, anneal it to make an ohmic electrical contact, and to try to inject spin polarized electrons from the ferromagnet into the semiconductor. These spins would then relax in the semiconductor with a characteristic time τ_s, the spin lifetime. Unfortunately, the injected spin polarization achieved in the semiconductor using this approach is extremely small. The spin accumulation in the semiconductor is suppressed by a factor of approximately 10^7 due to the large mismatch in the resistivities of the ferromagnet and semiconductor in combination with a spin lifetime that is much shorter in the ferromagnet than in the semiconductor [8]. In semiconductors doped around $n = 1\times10^{16}$ cm^{-3}, this timescale is approximately 10 ns, whereas in ferromagnetic systems it is of the order 10 ps. The suppression of the spin polarization in the semiconductor can be understood in terms of a two spin channel resistance model, where the spin lifetime is represented by resistors connecting the two spin channels, as illustrated in Fig. 1.2. This issue has come to be known as the "conductivity mismatch" argument. It was proposed that a tunnel barrier inserted between the ferromagnet and the semiconductor could solve this problem, as the tunneling current depends only on the tunneling matrix elements and the density of states in the ferromagnet and the semiconductor [9]. This was first implemented convincingly in 2002 by Hanbicki *et al.* in a Fe/AlGaAs/GaAs spin LED structure [10]. A Schottky barrier naturally forms at a metal/semiconductor interface due to the pinning of the Fermi energy at the interface. This creates a depletion layer of thickness:

$$d = \sqrt{\frac{2\epsilon\phi_B}{ne}}, \tag{1.4}$$

where ϕ_B is the barrier height, ϵ is the dielectric constant in the semiconductor, and n is the doping level of the semiconductor near the interface. It was found that a doping level of $n \approx 10^{18}$ to 10^{19} cm^{-3} created a Schottky barrier sufficiently thin for efficient spin injection. Spin polarized electrons could then be injected from the ferromagnet into the semiconductor by applying a bias across the interface. In the study by Hanbicki *et al.* the spin injection efficiency was determined by measuring

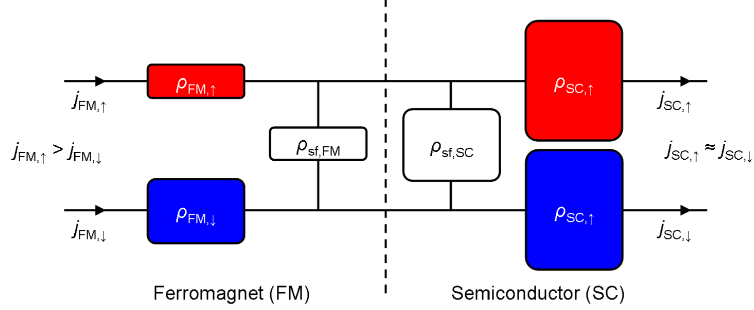

Figure 1.2: Schematic representation of the conductivity mismatch model. The spin polarization injected into the semiconductor is suppressed by a combination of two factors: $\rho_{SC} \approx 10^4 \rho_{FM}$ and $\rho_{sf,FM} \approx 10^{-3} \rho_{sf,SC}$. The $\rho_{sf,FM}$ acts as a short between the spin up and spin down channels in comparison to the much larger resistance of ρ_{SC}; thus, the resulting current in the semiconductor is essentially unpolarized.

the polarization of the emitted light from electrons and holes recombining in the GaAs quantum well. The polarization of the emitted light can be related to the electron spin polarization using the selection rules for optical transitions, where the angular momentum of the electrons is transferred to the emitted photons. A thorough discussion of spin LED devices and the design of the Fe/GaAs interface can be found in the Ph.D. thesis of Jonathan Strand [11].

1.3 Non-Local Electrical Spin Detection

In the previous section, we saw that electrical spin injection into semiconductors was first demonstrated by using optical techniques to detect spin polarization. However, for a fully functioning spin-logic device it is necessary to have an electrical detection scheme. A natural approach is to use a second ferromagnetic contact as an electrical spin detector. In a two terminal device geometry, as in the GMR and TMR structures discussed earlier, the spin polarized electrons are always traveling with a charge current. In a FM/SC/FM structure it is challenging to interpret data taken in a two-terminal device geometry because the spin-dependent

voltage can be obscured by other effects when a charge current is flowing into or in close proximity to a ferromagnetic electrode. The first of these effects is anisotropic magnetoresistance (AMR), where the resistance of the ferromagnetic contact will change depending on the relative orientation of the magnetization and the direction of current flow. A similar effect is tunneling anisotropic magnetoresistance (TAMR), where the tunneling resistance between the semiconductor and ferromagnet can change depending on the relative orientation between the magnetization of the ferromagnetic electrode and the crystal axes [12, 13]. Additionally, in low doped semiconductors, where Hall effects are large, stray fields from ferromagnetic contacts can lead to local Hall effects when a charge current flows nearby [14]. In this section, we will see that it is possible to decouple the spin polarization from the charge current by performing what is referred to as a non-local measurement, in which the voltage measurement used to measure the spin polarization is performed outside of the charge current path.

Non-local electrical spin detection was first implemented in metallic systems in 1985, when Johnson and Silsbee used the technique to measure permalloy/ aluminum/permalloy devices [15]. A schematic of a non-local measurement setup is shown in Fig. 1.3(a). In this geometry, a charge current j is passed through a ferromagnetic electrode FM1 into the normal metal, flowing down the normal metal channel to the left. This injects spin polarized electrons into the normal metal, thereby creating an imbalance in the spin-up and spin-down electrochemical potentials, shown in Fig. 1.3(b). This non-equilibrium spin polarization will then diffuse away from the injection electrode to both the left and the right in the normal metal channel. To the left of the injector, the motion of the spin polarized electrons is governed by both diffusion and drift along with the charge current with drift velocity v_d. To the right of the injector, however, their motion is governed by diffusion alone. Therefore, although there is no net charge current, there will still be a spin current defined as:

$$q_{x,y} = \frac{j_{x,\uparrow} - j_{x,\downarrow}}{e}, \tag{1.5}$$

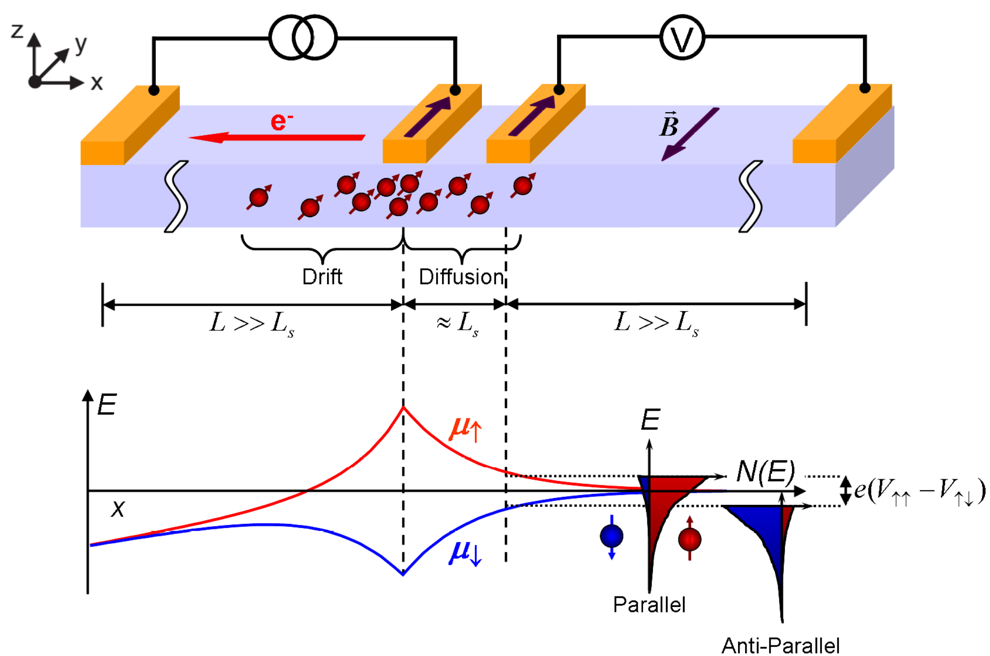

Figure 1.3: (a) Cartoon of the non-local measurement geometry. (b) Plot of spin up and spin down electrochemical potentials vs position in the normal metal.

where x indicates the direction of flow and y indicates the axis of spin polarization. The length scale over which the spin diffuses, called the spin diffusion length, is $L_s = \sqrt{D\tau_s}$, where D is the electron diffusion constant in the normal metal. The voltage is measured between a nearby ferromagnetic electrode to the right of the injection electrode, FM2, and a reference electrode far away from the spin injection point. The ferromagnetic detection electrode must be located within approximately a spin diffusion length of the injection electrode in order to measure a significant non-local signal, because the spin polarization decays exponentially on the length scale L_s. In metallic systems, this length scale is typically a few hundred nanometers. In semiconductors, due to the longer spin lifetime at low temperatures, this length scale can be several microns. For simplicity, we will assume that FM2 is an idealized half-metal, with 100% spin polariation at the Fermi level. If the magnetization of FM2 is oriented parallel to FM1, the Fermi level of FM2 will align with the spin up band in the normal metal. If the magnetization of FM2 is flipped so that it is anti-parallel to FM1, its Fermi level will align with the spin down band in the normal metal. Therefore, a voltage jump ΔV_{NL} is measured when the orientation of FM1 and FM2 is changed from parallel to anti-parallel. We find $\Delta V_{NL} = (\mu_\uparrow - \mu_\downarrow)/e$. In reality, the situation is somewhat more complicated. The detailed relationship between ΔV and the spin polarization will be discussed later in this chapter.

The non-local measurement scheme has become a widely used tool for the detection of spin polarizations in the time since Johnson and Silsbee's initial publication [16–23]. The first demonstration of non-local spin detection in semiconductors was published by Paul Crowell's group in 2007, and it is discussed extensively in Xiaohua Lou's Ph.D. thesis [24, 25]. In the following sections we will discuss two kinds of non-local measurements: the spin valve effect and the Hanle effect. The measurement techniques and analysis of the resulting data will be crucial in understanding the spin Hall effect, which will be discussed in Chapter 3.

1.4 Experimental Details

1.4.1 Sample Growth and Fabrication

The gallium arsenide (GaAs) and indium gallium arsenide ($In_xGa_{1-x}As$) heterostructures studied in this thesis were grown in ultra high vacuum at pressures near 10^{-10} Torr, using molecular beam epitaxy. Multiple pure elemental sources (Ga, As, Si, or In) are heated until they begin to sublimate. At these pressures the mean free path of a gas molecule is on the order of 10 km, so individual atoms travel on an uninterrupted path from the source to the growth wafer. By controlling the temperatures of the various sources the growth rate and composition can be controlled with a high degree of accuracy. A schematic of a typical sample structure is shown in Fig. 1.4(a). First, a 500 nm undoped GaAs buffer layer is grown on top of a (001) semi-insulating GaAs substrate. This is followed by a 2.5 μm silicon doped n-GaAs channel. The channel doping for most samples in this thesis is $n \approx 5 \times 10^{16}$ cm^{-3}, which is just above the metal-insulator transition in GaAs ($\approx 1 \times 10^{16}$ cm^{-3}). This doping level is chosen as a compromise between the need for a conductive channel and the desire for a long spin lifetime, which is largest for dopings near the metal-insulator transition [26]. The doping is then ramped up from $n = 5 \times 10^{16}$ cm^{-3} to $n^{+} = 5 \times 10^{18}$ cm^{-3} over a 15 nm region, and then kept at $n^{+} = 5 \times 10^{18}$ cm^{-3} for another 15 nm. The GaAs surface is typically As terminated, and a 5 nm epitaxial Fe layer is then deposited. The lattice constant of GaAs is very nearly twice that of Fe ($< 2\%$ lattice mismatch), so the Fe is also single crystal. Due to the surface-induced crystalline anisotropy the Fe has an easy axis along the [110] GaAs crystal direction and a hard axis along the $[1\bar{1}0]$ direction, with a saturation field $B_{sat} \approx 1.5$ kOe. Because the Fe is a thin film, the out of plane saturation field is $4\pi M_s \approx 2.1$ T. Finally, the structure is capped, first with Al and then Au, to prevent sample oxidation. A Schottky barrier with a barrier height $\phi_B \approx 0.8$ eV and width $d \approx 15$ nm forms at the Fe/GaAs interface, as illustrated in Fig. 1.4(b).

Each heterostructure is typically grown on a 10×20 mm^2 wafer of GaAs.

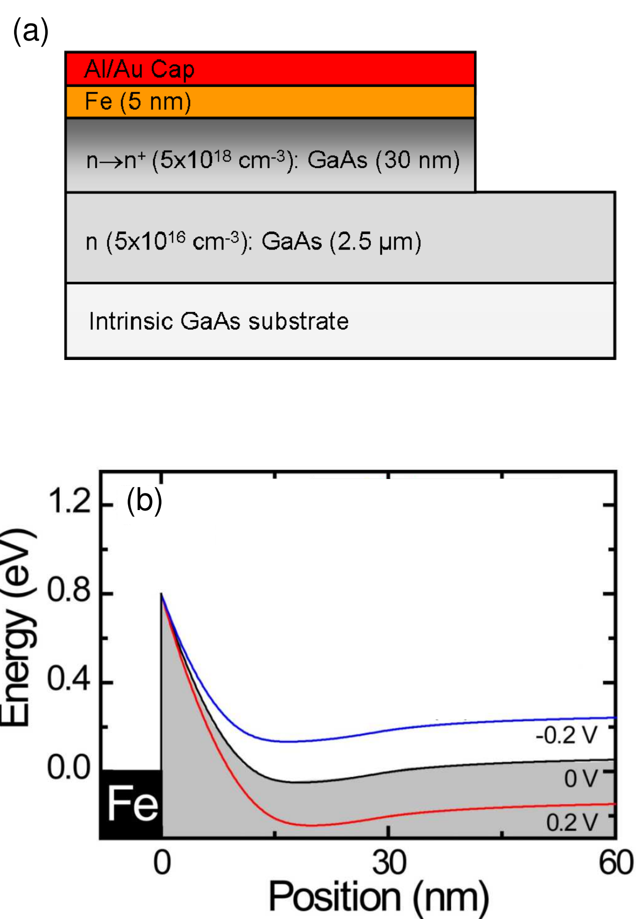

Figure 1.4: (a) Cross-sectional schematic of the Fe/GaAs heterostructures used in this thesis. (b) Plot of conduction band vs. distance from the Fe/GaAs interface under zero bias, forward bias and reverse bias, derived from Ref. [27].

These wafers are cleaved along the [110] and $[1\bar{1}0]$ directions into 5×5 mm^2 pieces which are processed separately into devices. The processing procedure involves four separate "layers", where a pattern from a photomask is transferred to the sample using photolithography, and each lithography step is followed by either an etch or a deposition and lift-off. The device layout changes depending on the details of the experiment, but the process is the same for all devices. Appendix A gives a detailed list of the steps involved in this process. Here we will discuss a general overview of the fabrication procedure, which is illustrated schematically in Fig. 1.5. A photomicrograph of a finished device is shown in Fig. 1.6. The general steps are:

I. Define Fe contacts: Argon ion milling is used to define the Fe contacts by removing the capping layers, iron layer, and highly doped layer from the rest of the structure. It is important to etch through the highly doped layer so that the electron transport in the GaAs is constrained to the n doped GaAs channel. Because GaAs etches much more quickly than Fe, this typically results in etching away $\approx$ 100 nm of the n-doped channel. Ar implantation defects are not a concern because the Ar implantation depth is $\sim$ 1 nm, whereas a surface depletion layer $\approx$ 100nm is formed at the n-GaAs/Vacuum interface. Fe injection and detection contacts are typically $\sim 5 \times 50$ μm, whereas reference electrodes are often much larger.

II. Define n-GaAs channel: The n-GaAs channel is defined by wet etching in a dilute ammonium hydroxide : hydrogen peroxide : water mixture. The channel is typically $\sim$ 50 μm wide and hundreds of μm long. It is important that the n-GaAs is etched down through the entire 2.5 μm, and that the channel be only slightly wider than the Fe contacts. This serves two functions. It constrains the charge current path, which minimizes any background voltages due to charge transport in the non-local measurement. It also ensures a uniform spin polarization

across the channel width, which allows us to interpret our results using a 1D spin diffusion model. The GaAs will be etched laterally as well as vertically, so when designing small GaAs features the mask must be adjusted accordingly. The etch is anisotropic, such that the edge perpendicular to the [110] direction will have a 45° slope and the edge perpendicular to the $[1\bar{1}0]$ direction will be nearly vertical. It is easier to run Au leads (step IV) up the graded edge.

III. Define SiN insulator: The Fe electrodes are too small to be contacted directly, so Au leads are deposited to make electrical contact to the device. To ensure that there is no shorting from the Au leads to the n-GaAs channel, a 200 nm thick insulating layer of SiN is deposited using Plasma Enhanced Chemical Vapor Deposition (PECVD) at 100 °C. This deposition is isotropic, which makes it difficult to lift-off regions of SiN smaller than $\approx 100\ \mu\text{m}^2$ without using a bi-layer recipe.

IV. Define Au leads and bonding pads: Ti/Au leads and bonding pads are deposited to to make electrical contact to the Fe electrodes. The Ti acts as a wetting layer to improve the adhesion of the Au. Au leads are typically run up the mesa edge along the [110] direction, and right angles near small features ($\lesssim 10\ \mu$m) should be avoided to prevent difficulties during lift-off.

1.4.2 Experimental Setup

Finished devices are mounted on Quantum Design rotator board and wirebonded. Devices typically have many more contacts than the number of available wirebonding pads, so it is often necessary to wirebond a device multiple times before a complete set of data is obtained. Two kinds of rotator boards are used, shown in Fig. 1.7. Universal rotator boards allow the field to be applied either in or out of the sample plane; samples are typically mounted so that the field is applied along

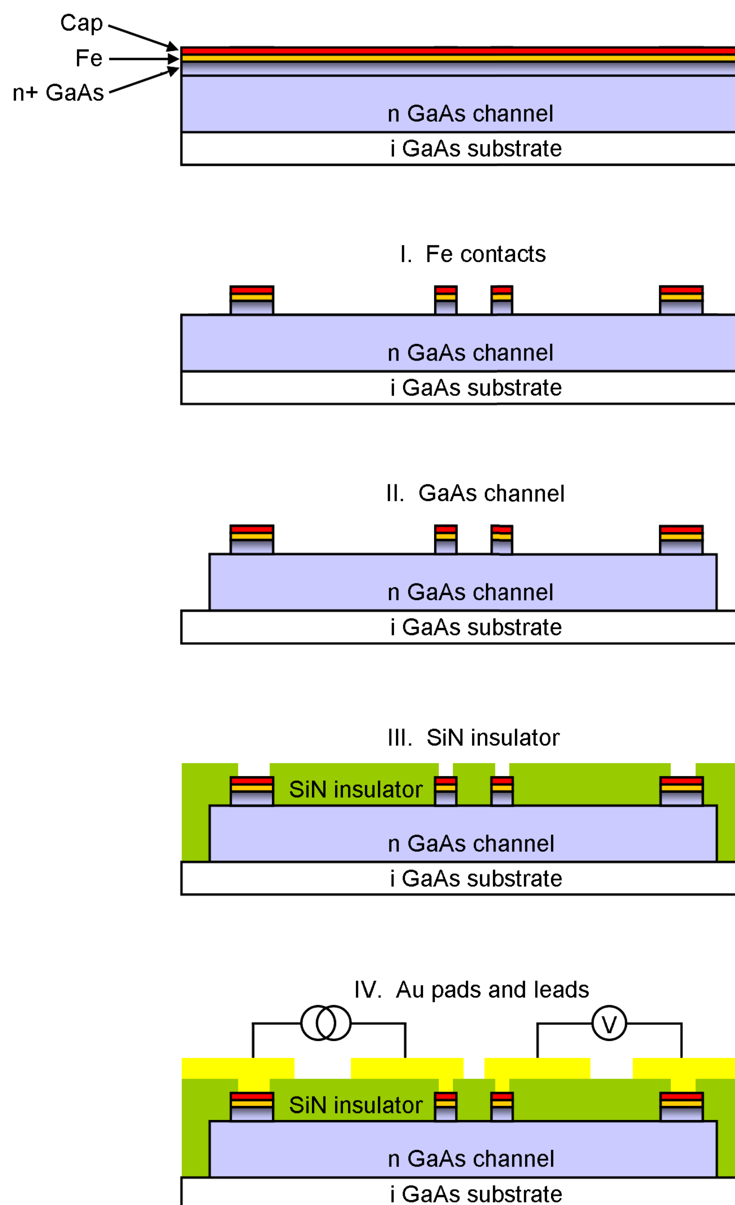

Figure 1.5: Illustration of sample fabrication process. Roman numeral labels correspond to the steps described in Sec. 1.4.1.

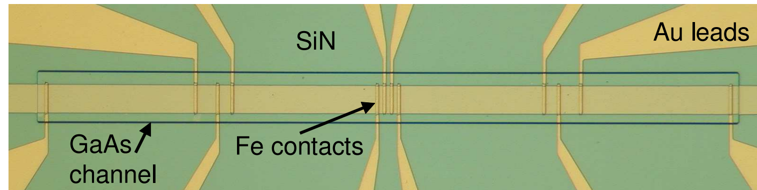

Figure 1.6: A photomicrograph of a finished non-local spin transport device.

the [110] Fe easy axis when the field is in the plane of the sample. Field-in-plane rotator boards allow the field to be applied along any direction in the sample plane.

Samples are loaded into a rotator probe, which allows for rotation between $-10°$ and $370°$, which is in turn inserted into a ^{4}He cryostat, a Quantum Design PPMS, for low temperature magneto-transport measurements. (Occasionally a Janis cryostat is used instead - the details of this cryostat are described in Mun Chan's Ph.D. thesis [28].) The temperature range of the cryostat is $T = 2$ to 300 K; however measurements are often limited to somewhat higher temperatures because the cooling power is limited by the high power dissipated by a device under large bias. This is especially true for the data presented in Chapter 3, where power dissipation from Joule heating can be as large as 40 mW. The resistance of the samples depends strongly on temperature, because they are doped near the metal insulator transition. It is therefore necessary to maintain temperature stabilities of $\lesssim 3$ mK for successful data analysis. A magnetic field is applied using a superconducting magnet which is capable of producing fields up to 9 T using a PPMS controller and power supply. The magnet can also be controlled by a bipolar amplifier power supply at fields less than ≈ 5 kOe, which allows for higher resolution and better sweep rate control at low fields. Nearly all of the data presented in this thesis are taken using the bipolar amplifier to control the magnetic field. A Keithley 220 DC current source is typically used to current bias the sample. A Keithley 2182 nanovoltmeter is used to measure the device voltage. A switching matrix is used to enable automated switching of the current and voltage leads. Specific measurement configurations will be discussed

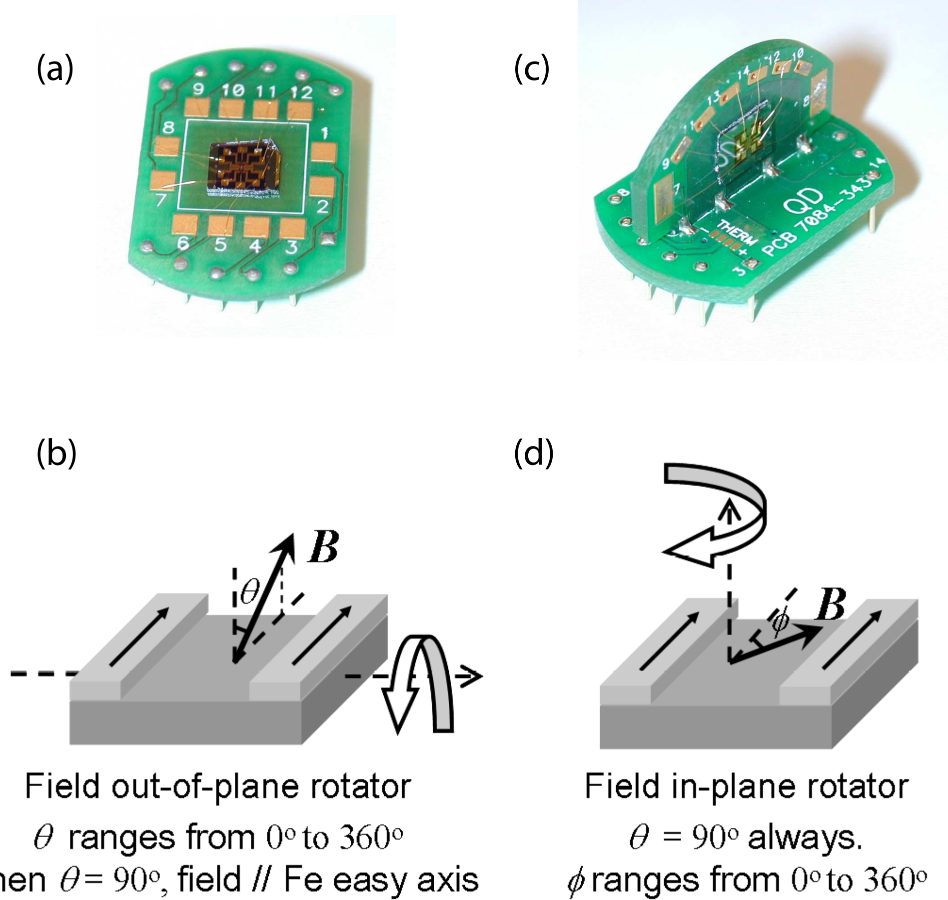

Figure 1.7: Pictures of the different rotator board sample mounts used in magneto-transport measurements, along with corresponding rotation diagrams.

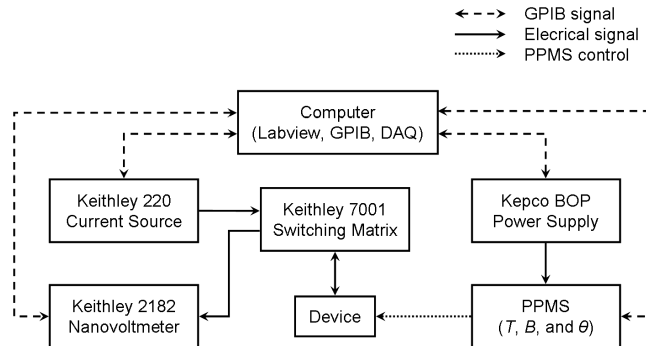

Figure 1.8: Block diagram of the experimental setup, showing electrical and GPIB connections.

in more detail in the relevant sections of this thesis. A desktop computer with LabView software and GPIB and DAQ cards is used to control and automate the experimental apparatus. Figure 1.8 shows a block diagram of the experimental setup.

Low temperature transport measurements discussed in this thesis can be divided into three categories. The first consists of various spin-independent measurements including resistivity measurements, interface IV curves, and Hall measurements. These measurements are used to characterize the electrical properties of the device, such as the mobility and carrier concentration. The second involves electrical spin injection and detection measurements, which will be described in this chapter. These measurements are used to characterize the spin injection and detection efficiencies of the ferromagnetic electrodes, as well as the spin transport properties of the semiconductor channel. The third involves electrical detection of spin polarizations generated by the spin Hall effect, a phenomenon which occurs due to spin-orbit coupling in the semiconductor. These measurements will be discussed in Chapter 3.

1.5 Non-Local Spin Valve and Hanle Measurements

Two different kinds of non-local measurements are performed to characterize the spin injection and detection properties of the ferromagnetic electrodes and the spin transport properties of the semiconductor. These measurements, called non-local spin valve and non-local Hanle measurements, are shown schematically in Fig. 1.9(a) and (d) respectively. In both measurements, spin polarized electrons are either injected or extracted from the semiconductor channel by applying a current bias between an iron electrode and a reference electrode many spin diffusion lengths away. The voltage is then measured between a nearby iron electrode and another reference electrode at the opposite edge of the channel, also many spin diffusion lengths away. In the spin valve measurement, a magnetic field is applied along the ferromagnetic easy axis. As the magnetic field is swept, the orientation of the injector relative to the detector is flipped from parallel to anti-parallel, and a voltage jump $V_{\uparrow\uparrow} - V_{\uparrow\downarrow}$ is observed. Raw data from a spin valve measurement are shown in Fig. 1.9(b). Despite the fact that the detector electrode is nominally located outside of the charge current path, we observe a spin-independent background voltage that occurs due to charge transport. This background is typically of order ≈ 1 mV, and can be removed by subtracting a linear offset from the raw data. Background subtracted data are shown in Fig. 1.9(c). The spin-dependent voltage jump can be related to the electrochemical potential shift between the spin up and spin down bands in the semiconductor by the following expression:

$$V_{\uparrow\uparrow} - V_{\uparrow\downarrow} = \eta P_{Fe} \frac{\Delta\mu}{e}, \tag{1.6}$$

where $P_{Fe} = 0.42$ is the polarization of Fe at the Fermi level, and η is the zero-bias spin detection efficiency, a dimensionless parameter between 0 and 1. It was found that the spin injection efficiency was ≈ 0.5 in measurements on spin LEDs at finite bias [29]. We assume that the the zero-bias spin detection efficiency is

comparable, $\eta \approx 0.5$. We define the spin polarization in the semiconductor to be:

$$P_{SC} = \frac{n_\uparrow - n_\downarrow}{n_\uparrow + n_\downarrow}, \tag{1.7}$$

where $n_\uparrow$ and $n_\downarrow$ are the densities of spin up and spin down electrons in the semiconductor. We can then relate the voltage jump to the spin polarization in the semiconductor using the relationship between $\Delta\mu$ and the density of states in the semiconductor, assuming $\Delta\mu$ is small relative the Fermi level in the semiconductor:

$$\Delta\mu = \frac{nP_{SC}}{N(E_F)}, \tag{1.8}$$

where $N(E_F)$ is the density of states in the semiconductor at the Fermi energy. Assuming a free electron gas model for the semiconductor, we find

$$N(E_F) = \frac{3}{2}\frac{n}{E_F}, \tag{1.9}$$

where

$$E_F = \frac{\hbar^2}{2m^*}(3\pi^2 n)^{2/3}. \tag{1.10}$$

Here m^* is the effective mass for conduction band electrons in the semiconductor, which will be discussed in more detail in Chapter 2. For GaAs, $m^* \approx 0.067m_0$, where m_0 is the rest mass of the electron in the vacuum. Finally, we arrive at the following expression relating the voltage jump to the spin polarization in the semiconductor:

$$V_{\uparrow\uparrow} - V_{\uparrow\downarrow} = \eta P_{Fe}\frac{\Delta\mu}{e} = \frac{2\eta P_{Fe}P_{SC}E_F}{3e}. \tag{1.11}$$

In Fig. 1.9(c) we find $V_{\uparrow\uparrow} - V_{\uparrow\downarrow} \approx 50\ \mu$V, leading to an estimated spin polarization of $P_{SC} \approx 5\%$ underneath the detector electrode.

A far more rigorous demonstration of electrical spin detection is given by the measurement of the Hanle effect, which relies on spin precession. In the Hanle effect, a magnetic field is applied out of the plane of the sample, as illustrated in

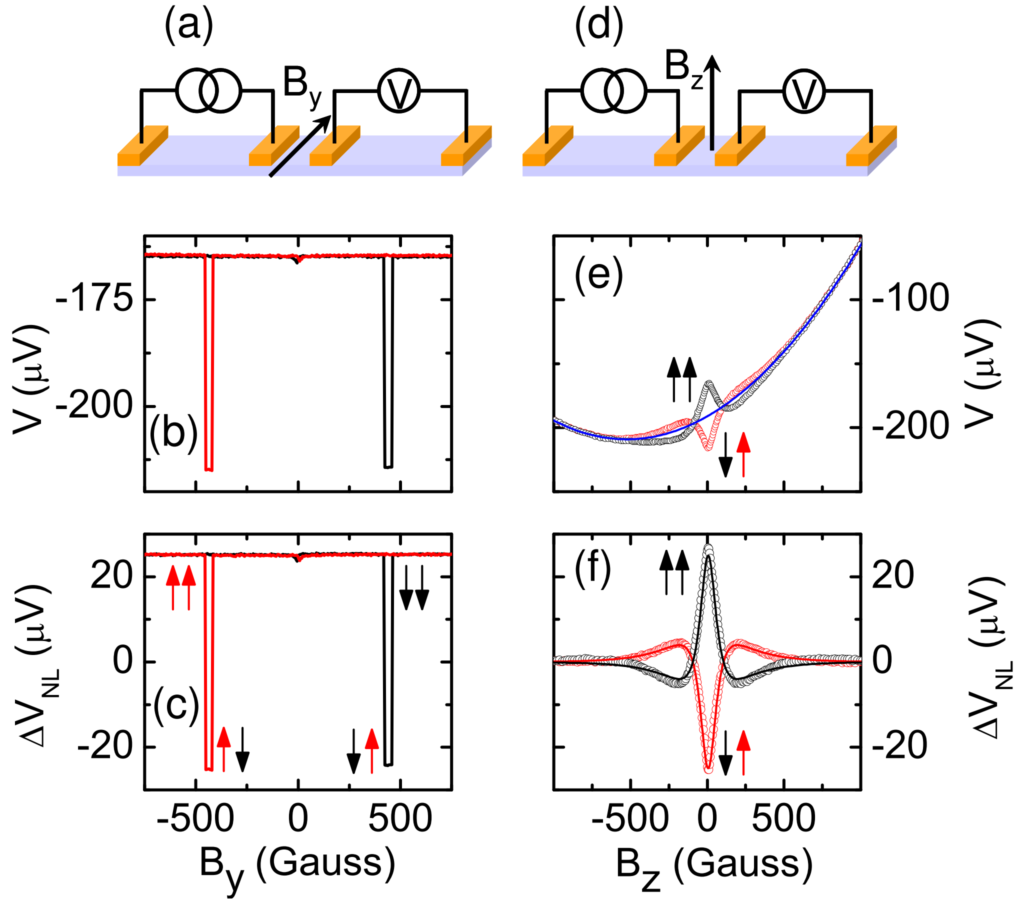

Figure 1.9: (a) NLSV measurement schematic. (b) NLSV raw data. (c) NLSV background subtracted data. (d) NL Hanle measurement schematic. (e) NL Hanle raw data. (f) NL Hanle background subtracted data. These data were taken at $T = 60$ K, with a current bias $j = 10^3$ A/cm^2, corresponding to an interface voltage $V_{int} = -360$ mV. The fit parameters to the Hanle data correspond to a spin lifetime $\tau_s \approx 4$ ns, $L_s \approx 4$ μm, and $P_{SC} \approx 5\%$. Data in this figure were taken by Mun Chan [28].

Fig. 1.9(d). The in-plane spin polarized electrons precess about the applied field at a rate given by the Larmor precession frequency

$$\mathbf{\Omega}_L = \frac{g^* \mu_B \mathbf{B}}{\hbar}, \tag{1.12}$$

where μ_B is the Bohr magneton and g^* is the effective electron g-factor in the semiconductor, which will be discussed in greater detail in Chapter 2. For GaAs, $g^* = -0.44$. At a given applied field, the total angle precessed by a spin as it travels from the injector to the detector depends on the transit time. The motion of the spins toward the detector is diffusive, therefore there will be a distribution of arrival times given by:

$$P(t) = \frac{1}{\sqrt{4\pi Dt}} e^{-\frac{L^2}{4Dt}}, \tag{1.13}$$

where $P(t)$ is the probability of a spin arriving at time t, and L is the distance between the injector and the detector. In the above expression we have ignored the process of spin relaxation, which decreases $P(t)$ by a factor of e^{-t/τ_s}. Due to the distribution of arrival times of spins at the detector electrode, the *ensemble* spin polarization at the detector is dephased as the spins precess more quickly with increasing magnetic fields. The magnetic field required to dephase the spin polarization can be roughly characterized by:

$$\frac{g^* \mu_B B_{1/2}}{\hbar} t_0 \approx 1, \tag{1.14}$$

where $B_{1/2}$ is the half-width of the Hanle curve and t_0 is the shorter of either τ_s or L^2/D.

Raw data from a Hanle measurement with the injector and detector in both the parallel and anti-parallel configurations are shown in Fig. 1.9(e). The two curves meet when the spin polarization is completely dephased. Once again we see that there is a significant spin-independent background due to charge transport effects that must be subtracted from the data. This is accomplished by subtracting a second order polynomial fit to the high field regime where the spin polarization has been completely dephased. The resulting background subtracted

Hanle data are shown in Fig. 1.9(f). At zero field, the voltage difference between the parallel and anti-parallel Hanle curves is equal to the voltage jump measured in the spin valve effect. Due to the large field (≈ 2.1 T) required to saturate the magnetization out of the plane of the sample, the magnetization of the injector and detector electrodes remains fixed during the Hanle measurement, which rules out any spurious effects such as local Hall effects.

It is possible to model and fit the resulting spin signal analytically using a model that incorporates spin diffusion, drift, relaxation and precession. The full differential equation that accounts for these effects is:

$$\frac{\partial \mathbf{S}}{\partial t} = -v_d \frac{\partial \mathbf{S}}{\partial x} + D \frac{\partial^2 \mathbf{S}}{\partial x^2} - \frac{\mathbf{S}}{\tau_s} - \mathbf{\Omega}_L \times \mathbf{S} + \mathbf{S}_0, \tag{1.15}$$

where $\mathbf{S}_0$ is a source term which generates spins at a rate S_0 per unit length over the length of the injector electrode, with a spin orientation parallel to the magnetization of the injector. The spin polarization is uniform across the width of the channel, so we will restrict our discussion to the case of 1D spin transport. The ferromagnetic electrode is sensitive only to spin polarization parallel to the magnetization direction, so the steady state spin signal at the detector electrode is given by:

$$S_y(B) = \int dx_1 \int dx_2 \int_0^\infty \frac{S_0}{\sqrt{4\pi Dt}} e^{-\frac{(x_2 - x_1 + v_d t)^2}{4Dt}} e^{-\frac{t}{\tau_s}} \cos(\Omega_L t) dt, \tag{1.16}$$

where the finite spatial extent of the injection and detection electrodes are taken into account by integrating over x_1 and x_2 respectively. In the non-local configuration we may take the drift velocity to be zero. The diffusion constant can be determined using from independent charge transport measurements of the mobility and carrier concentration using the Einstein relation [30]. This leaves S_0 and τ_s as the only free fitting parameters. For the data shown in Fig. 1.9, we find $\tau_s \approx 4$ ns.

In the remainder of this chapter, we will investigate the bias dependence of spin injection and spin detection in Fe/GaAs samples. In Chapter 3, we will build on the analysis presented here to measure and quantify the spin Hall effect, which will be detected by using the Hanle effect.

1.6 Bias Dependence of Spin Injection

We have performed non-local measurements at many different current biases to better understand the spin injection properties of the Fe/GaAs interface. Figure 1.10(a) shows the measured non-local spin signal for 4 different samples as a function of injector bias. The detailed doping profile of these samples is listed in Table 1.1. There are three striking features of these data. The first is the fact that both the magnitude and sign of the detected spin signal vary greatly from sample to sample for the same injector bias. The second is that, for all samples, the detected spin signal is the same sign for both positive and negative injector biases. Under reverse bias, where spin polarized electrons are being injected from the Fe into the GaAs, one would expect the injected electrons to have the polarization of Fe majority spins. It is somewhat surprising that under the opposite bias polarity (forward bias), where electrons are traveling from the GaAs into the Fe, the spin accumulation in the semiconductor has the same sign. From linear response theory, one would expect that Fe majority spin polarized electrons would more readily tunnel from the GaAs to the Fe. It has been confirmed by optical Kerr rotation measurements that the spin polarization in the GaAs at both large reverse and large forward bias corresponds to Fe majority spins [31, 32]. (See Xiaohua Lou's Ph.D. thesis for a more thorough discussion of Kerr microscopy [25].) Thus, we see that linear response theory is only valid over a very narrow voltage range, $\lesssim$ 100 mV. In practice it is often difficult to resolve a region of injector bias where there is a minority spin accumulation in the GaAs; only sample A shows a clear reversal of the sign of the spin accumulation at zero injector bias. The final significant feature of Fig. 1.10 is the fact that, normalized to signal magnitude, all four samples show a very similar dependence on V_{Int}. The locations of maxima and minima are at roughly the same values of V_{Int} for all four samples. This suggests that the interfacial spin injection properties of these devices are quite similar, despite the variations in magnitude and sign of the detected spin signal.

Two different theories have been put forward to explain the unexpected bias

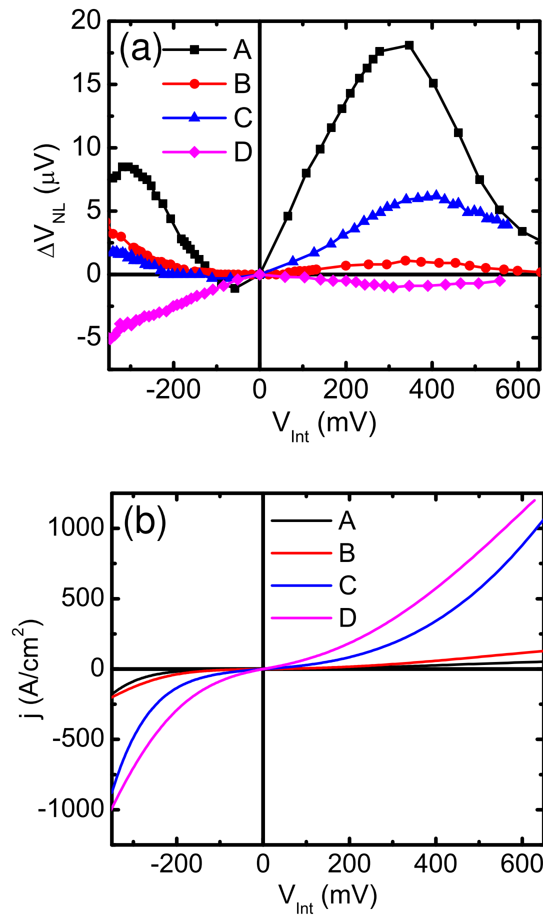

Figure 1.10: (a) Bias dependence of detected spin signal as a function of injector voltage for 4 different Fe/GaAs samples. (b) IV curves for the 4 different samples. All data in this figure was taken at $T = 10$ K.

Sample	Schottky Barrier Profile ($n^+ = 5 \times 10^{18}$ cm^{-3})	Channel Doping n (10^{16} cm^{-3})
A	15 nm n^+ / 15 nm $n^+ \rightarrow n$	3.5
B	20 nm n^+	3.5
C	25 nm n^+	3.5
D	15 nm n^+ / 15 nm $n^+ \rightarrow n$	5.0

Table 1.1: Doping profile of samples in Fig. 1.10 and Fig. 1.12.

dependence observed in Fig. 1.10(a), both of which depend on detailed arguments about the **k**-dependence of the tunneling process. The first was published by Dery and Sham in 2007 [33], and is illustrated schematically in Fig. 1.11(a). There is a narrow quantum well near the Fe/GaAs interface due to the doping profile near the highly doped region that forms the Schottky barrier. This quantum well is deep enough to have several bound states which will localize electrons. Dery and Sham calculated the escape time for electrons tunneling from bound states in this quantum well into the majority and minority spin bands in the Fe on the other side of the Schottky barrier. They used a simplified model of the Fe density of states assuming a free electron mass with $k_{Fe,\uparrow} \approx 3k_{Fe,\downarrow}$. They found that the escape rate from each of the bound states into minority spin band was about twice that of the escape rate into the majority spin band due to closer matching of k_{QW} with $k_{FM,\downarrow}$. They argued that at sufficiently large forward bias ($\approx$ 100 mV) the tunneling current from localized states in the quantum well would be the dominant contribution to the total current. This results in minority spin polarized electrons being extracted from the quantum well. These electrons are replaced quickly by minority spin polarized electrons in the bulk via energy relaxation, which occurs much more rapidly than spin relaxation in either the bulk or the quantum well. This results in a majority spin accumulation in the bulk GaAs.

The second argument was published by Chantis *et al.* in 2007 [34]. Chantis *et al.* performed a first principles calculation of the detailed electronic band structure at the Fe/GaAs interface. From their calculation they were able to estimate the **k** resolved Fe/GaAs interfacial density of states and tunneling transmission

probabilities for spin up and spin down electrons, which are shown in Fig. 1.11(b). They found that under forward bias voltages between $\approx$ 100 to 400 mV, minority spin electrons dominate the tunneling current due to peaks in the minority spin interfacial density of states and the minority spin tunneling transmission probability at matched values of $\mathbf{k}$. It is likely that the different mechanisms described by Dery and Sham and Chantis are both in play in determining the total spin injection bias dependence.

1.7 Bias Dependence of Spin Detection

To better understand the variation in magnitude and sign of the detected spin signal from sample to sample, we have also studied the bias dependence of spin detection on these samples. This requires a modification to the experimental setup described in section 1.4.2. In order to study the bias dependence of spin detection independently from the bias dependence of spin injection, we apply a DC bias to the detector electrode while now applying a unipolar AC bias to the injection electrode. The voltage is measured at the detector electrode using a lock-in amplifier and therefore measures the change in voltage at the detector due to the additional spin packet from the injector. This setup is shown schematically in Fig. 1.12(a). Detector bias measurements were performed at several different injector biases to confirm that the measured detector bias dependence was independent of injector bias (see Fig. 1.12(b)). For a given injected spin polarization, the voltage induced at the detector electrode depends strongly on the voltage bias across the detector and can even change sign. It was found that the detector's spin sensitivity could be significantly enhanced under forward bias.

The spin detection sensitivity depends on a combination of effects at the Fe/GaAs interface and charge transport effects in the GaAs channel. These two effects can be disentangled by considering a 1D model that includes drift effects in the semiconductor channel and bias dependent tunneling conductances at the Fe/GaAs interface [32, 35]. The voltage drop across the detector can be written

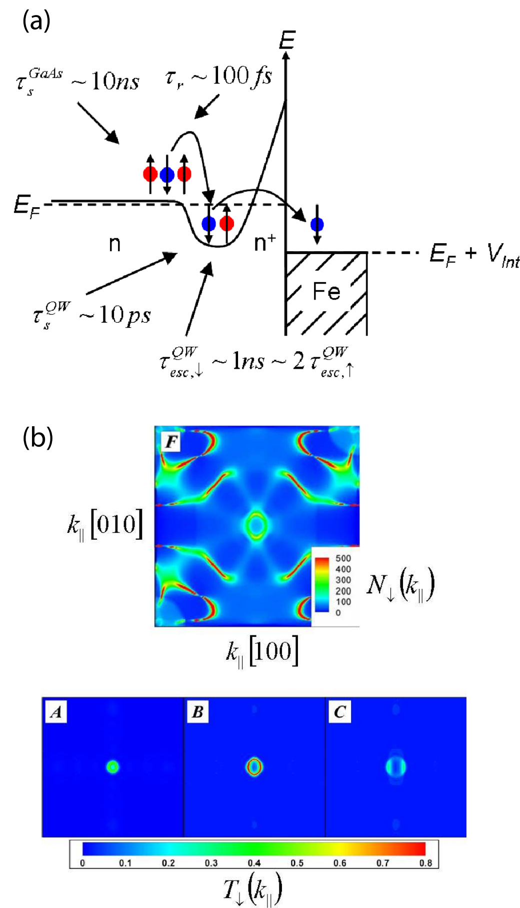

Figure 1.11: (a) Cartoon schematic of tunneling mechanism proposed by Dery and Sham. Minority spin polarized tunneling from bound states in the quantum well near the Fe/GaAs interface could lead to a majority spin accumulation in the GaAs under forward bias [33]. (b) Plot of **k** dependent minority spin DOS at the Fe/GaAs interface and the **k**-dependent minority spin tunneling transmission probability as calculated by Chantis *et al.* [34]. (Figures are adapted from Fig. 2 and 3 in Ref. [34].) They found that minority spin polarized electrons dominate the tunneling current under a wide range of forward biases.

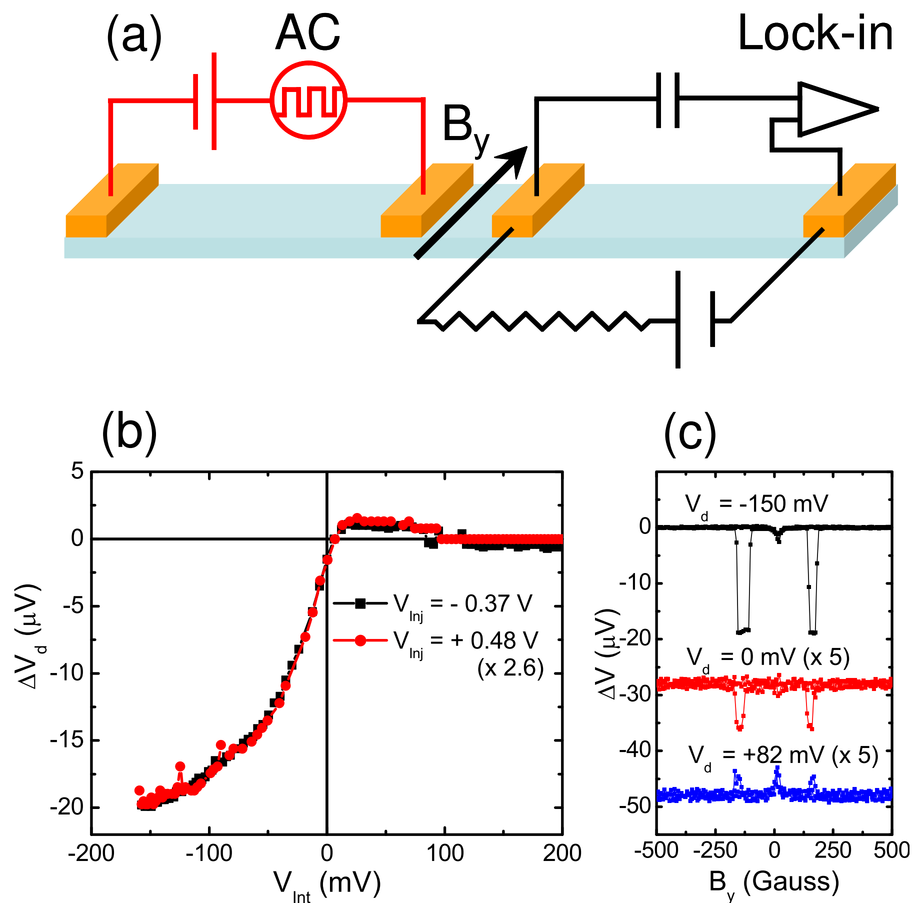

Figure 1.12: (a) Experimental setup for measurement of bias dependence of spin detection. (b) Measured bias dependence of spin detection under two different injector biases shows identical behavior. (c) Spin valve measurements show a significant enhancement in the detected spin signal under forward detector bias. All data in this figure was taken at $T = 10$ K.

as [35]:

$$V_d = \frac{j}{4}\left[\left(\frac{1}{G_\uparrow} + \frac{1}{G_\downarrow}\right) + \left(\frac{1}{G_\uparrow} - \frac{1}{G_\downarrow}\right) P_j\right], \tag{1.17}$$

where $P_j = (j_\uparrow - j_\downarrow)/(j_\uparrow + j_\downarrow) \propto P/j$ is the spin polarization of the tunneling current and $G_{\uparrow,\downarrow}$ are the spin up and spin down tunneling conductances, which in general can depend on bias. The voltage measured in the experiment depicted in Fig. 1.12 can be interpreted as the change in the voltage at the detector due to a change in the spin polarization of the current due to the additional spin packet injected at the detector. Therefore:

$$\Delta V_d \propto \frac{\partial V_d}{\partial p} = \frac{e}{4}\left(\frac{1}{G_\uparrow} - \frac{1}{G_\downarrow}\right) j \frac{\partial P_j}{\partial p}, \tag{1.18}$$

where p is the additional spin polarization due to the AC injector bias.

Figure 1.13 shows the detector bias dependence for samples A-D. All four samples show a maximum in ΔV_d near zero bias. This peak corresponds to the detector bias at which additional spin polarized electrons in the semiconductor will induce the largest voltage change at the detector, which suggests that the Fermi level may be pinned near a peak in the majority spin density of states at the Fe/GaAs interface. Moving away from this peak toward forward bias, ΔV_d changes sign in all four samples. The zero crossing occurs near the voltage where $P_j = 0$, as can be seen in Fig. 1.14(c) and (d), which shows both P_j and ΔV_d for two samples similar to samples A and D that were measured by our collaborator Scott Crooker [32]. For these figures, P_j was measured using optical Kerro microscopy (see Fig. 1.14(a)) and ΔV_d was measured using optical spin injection (see Fig. 1.14(b)). Under large forward bias (negative interface voltages), ΔV_d shows significant enhancement from the zero-bias detector sensitivity in multiple samples. This can be attributed to drift effects. To take into account transport effects in the GaAs channel, we note that $j\partial P_j/\partial p$ can be written as:

$$j\frac{\partial P_j}{\partial p} = D\frac{\partial}{\partial p}\left[\frac{\partial(n_\uparrow - n_\downarrow)}{\partial x}\right] + \mu E\frac{\partial}{\partial p}(n_\uparrow - n_\downarrow), \tag{1.19}$$

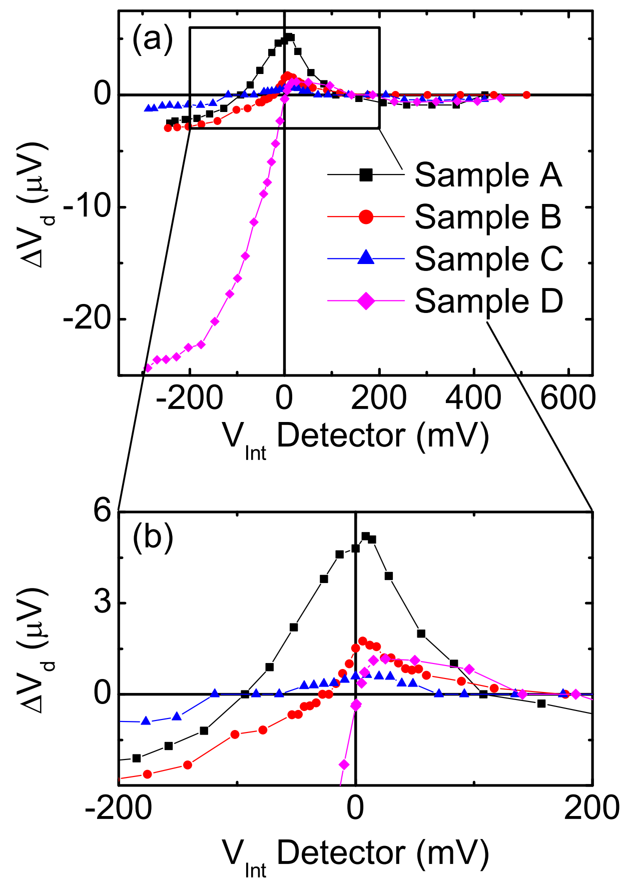

Figure 1.13: (a) Measured bias dependence of spin detection on all four samples shows similar behavior. (b) Zoomed in plot near zero detector bias shows a peak in ΔV_d for all samples, and a sign change of ΔV_d as V_{Int} moves away from this peak toward forward bias. Data were taken at $T = 10$ K under forward injector bias for all samples.

where D is the electron diffusion constant, E is the channel electric field, and $n_\uparrow - n_\downarrow$ and its gradient are evaluated at the interface. Here we see that under forward bias both the drift and diffusion terms move p toward the detector electrode, leading to an enhancement in the detector bias sensitivity. Under reverse bias, however, the drift and diffusion terms oppose each other, which leads to a suppression of the spin signal at the detector.

It is possible to calculate the bias dependence of $G_\uparrow$ and $G_\downarrow$ from the spin injection bias dependence and the interface IV curve (shown in Fig. 1.10). The solid lines in Fig. 1.14(c) and (d) show the detector bias dependence predicted using the values of $G_\uparrow$ and $G_\downarrow$ determined from P_j for different mobilities in the GaAs, which show reasonable agreement with the data for mobilities around $\approx$ 1500 cm^2/Vs. Measured channel mobilities in these samples were $\approx$ 3000 to 8000 cm^2/Vs under the bias conditions of the measurements. It is important to note that the mobility near the Fe/GaAs interface may be substantially lower than the channel mobility, due to the higher doping level near the interface.

1.8 Three Terminal Spin Detection

Section 1.3 discussed the difficulties in interpreting the spin-dependent voltage at a FM/SC interface when a charge current is flowing through the detection electrode. Here we return to this issue, and we show that it is possible to interpret the spin-dependent voltage change at the FM/SC interface using the knowledge gained by studying the spin injection and spin detection bias dependences separately. We perform a measurement of the spin dependent voltage at the Fe/GaAs interface using the measurement configuration shown in Fig. 1.15(a). In this three terminal configuration, a spin accumulation is generated in the GaAs by passing a current through the injector electrode. The voltage is then measured between the injector electrode and another reference electrode. By applying a magnetic field out of the plane of the device, we use the Hanle effect to dephase the spin accumulation in the GaAs. The orientation of the magnetization remains fixed during the

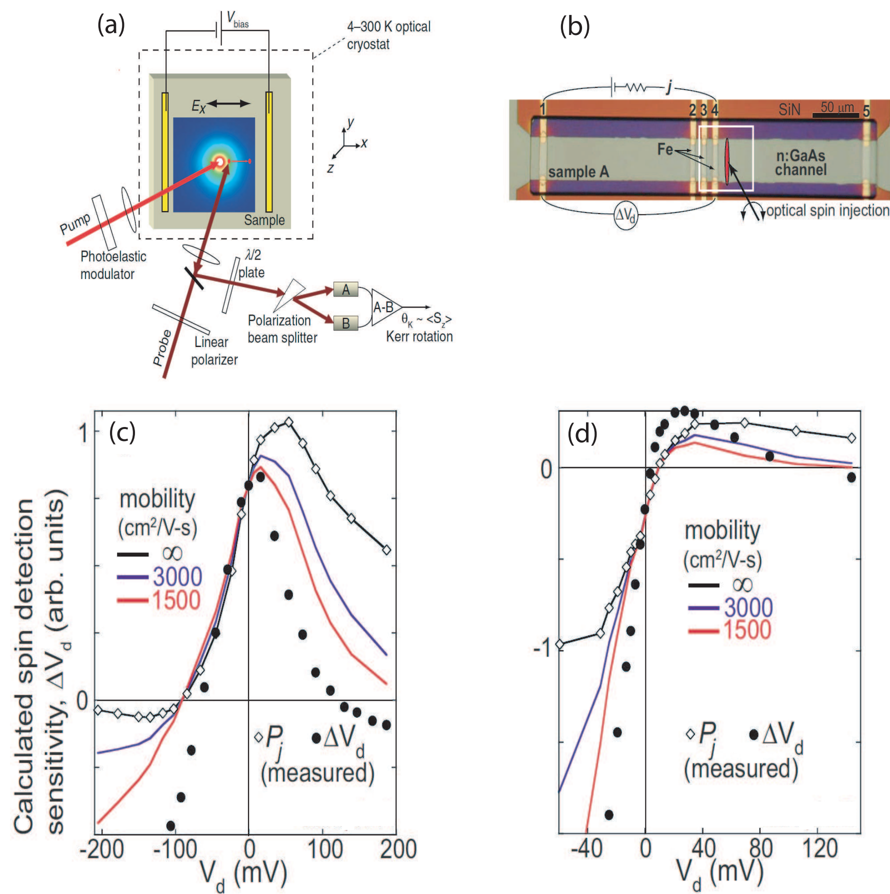

Figure 1.14: (a) Schematic of experimental setup to optically detect P_j using the Kerr effect, derived from Ref. [36]. (b) Schematic of experimental setup to measure ΔV_d by optically injecting spin polarized electrons. (c) P_j and ΔV_d measured on a sample similar to sample A. (d) P_j and ΔV_d measured on a sample similar to sample D. Panels (b)-(d) derived from Ref. [32]. All data in this figure were taken at $T = 10$ K.

measurement, so we are able to rule out any spurious effects due to AMR or fringe fields. The voltage at the injector is only sensitive to the spin polarization in the GaAs when it is forward biased. Under reverse bias, spin polarized electrons are injected into empty states well above the Fermi level, so the voltage at the injector is not sensitive to the spin accumulation in the GaAs. Figure 1.15(b) shows the measured change in voltage vs applied field. Similar to the non-local Hanle data, there is a spin-independent background that can be removed by fitting a second order polynomial to the data at large fields where the spin polarization has been completely dephased. The spin-dependent voltage change, shown in Fig. 1.15(c) can be interpreted using Eq. 1.17, where P_j is being decreased to zero by the applied magnetic field. We can estimate this voltage change as a function of interface voltage using the measured bias dependencies of spin injection and spin detection discussed in the previous sections:

$$\Delta V_{3T}^{Est} = \Delta P \times \frac{\partial V_d}{\partial p} = \frac{\Delta V_{NL}(V_{Int})}{2e^{-L/L_s}} \times \frac{\Delta V_d(V_{Int}, V_0)}{\Delta V_{NL}(V_0)}, \tag{1.20}$$

where $\Delta V_{NL}(V_{Int})$ is the measured non-local voltage when the injector is biased at V_{Int} and $\Delta V_d(V_{Int}, V_0)$ is the measured voltage change at the detector electrode when the detector is biased at V_{Int} and the AC modulated injector is biased at V_0. The data can be modeled reasonably well with no free parameters by using the same spin lifetime determined from the non-local Hanle fitting, shown as the solid line in Fig 1.15(c). Figure 1.15(d) shows the predicted and measured three terminal signal, which shows good agreement over the voltage range studied. It is important to note that the estimate made in Eq. 1.20 assumes that $\partial V_d/\partial p$ is linear with respect to p. Although this assumption appears to be valid for voltage ranges studied here, it is clear from the non-linear bias dependence of $\Delta V_d(V_{Int})$ that this assumption will break down if the spin accumulation in the semiconductor is large enough ($>$ mV).

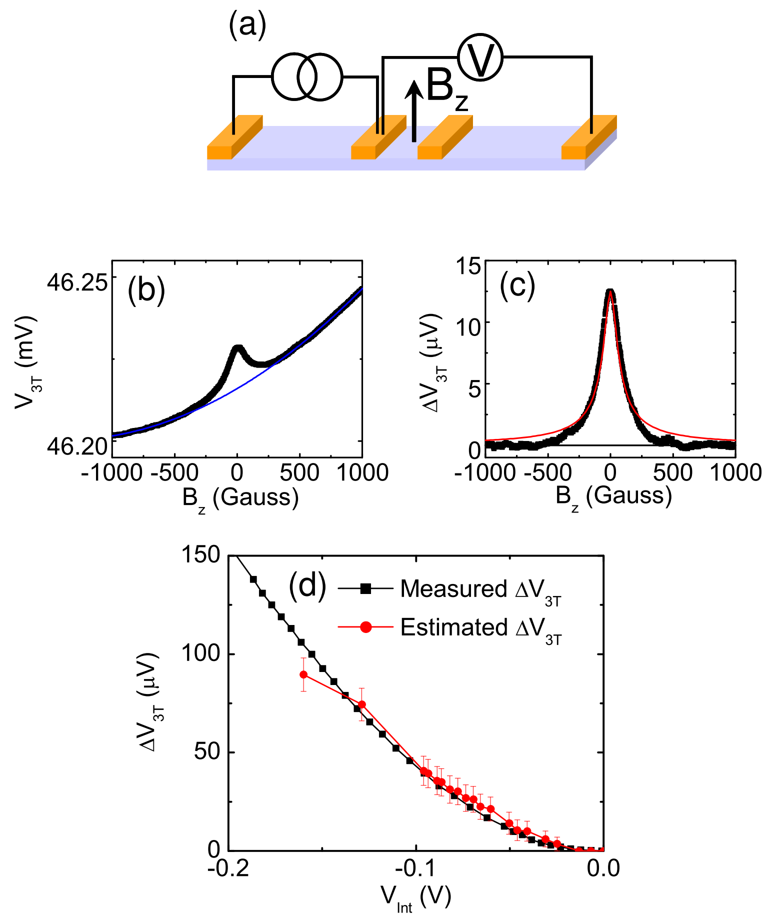

Figure 1.15: (a) Three terminal Hanle effect measurement setup. (b) Raw three terminal data at $T = 60$ K, with a current bias $j = 25$ A/cm^2, corresponding to an interface voltage $V_{int} = -53$ mV. (c) Background subtracted three terminal data with fit using no free parameters (τ_s is determined from non-local Hanle measurements at $T = 60$ K). (d) Plot showing the magnitude of the measured three terminal spin signal at $T = 60$ K and the predicted signal estimated from the bias dependence of spin injection and spin detection at $T = 10$ K.

Chapter 2

Spin-Orbit Coupling

2.1 Introduction to Spin-Orbit Coupling

Spin-orbit coupling describes an interaction that couples the electron's momentum to its spin state. This topic is of great interest in semiconductor spintronics for two primary reasons. First, it provides a means to manipulate the electron's spin state by applying electric fields rather than magnetic fields, as were used in the experiments described in Chapter 1. Second, the spin orbit interaction determines the rate of spin relaxation in the semiconductor channel. Both of these effects will manifest themselves in the measurements of the spin Hall effect presented in Chapter 3, which occurs due to spin dependent scattering. In this chapter, in order to arrive at a better fundamental understanding of spin-orbit coupling, we will first investigate its effects on an electron bound to a hydrogen atom in the vacuum. We will then discuss spin-dependent scattering from charged nuclei in the vacuum, and we will extend this discussion to spin-dependent scattering in solids. Finally, in Chapter 4 we will show that spin-orbit coupling can be used to manipulate electron spin states even in the absence of impurity scattering, due to spin-orbit effects that are "intrinsic" to the material structure.

2.2 Spin-Orbit Coupling in the Vacuum

2.2.1 Spin-Orbit Coupling and the Hydrogen Atom

To first order, the Hamiltonian of an electron orbiting a hydrogen atom in a vacuum involves only the kinetic energy from the electron's momentum and the potential energy due to the Coulomb potential:

$$H = \frac{\mathbf{p}^2}{2m_0} - e\Phi(r) = -\frac{\hbar^2}{2m_0}\boldsymbol{\nabla}^2 - \frac{e^2}{r}, \tag{2.1}$$

where $e > 0$ is the elementary charge. Because the electron will be orbiting the nucleus with a momentum $\mathbf{p}$, there is an additional term that arises due to spin-orbit coupling. In the rest frame of the electron, the nucleus is orbiting the electron with a velocity $\mathbf{v}_p = -\mathbf{p}/2m_0$. (The factor of 2 in the denominator, called the Thomas factor, is due to the fact that the electron is in an accelerating reference frame [37].) From the Biot-Savart law, the circular motion of the nucleus about the electron produces a magnetic field:

$$\mathbf{B}_{SO} = \frac{1}{c}\mathbf{v}_p \times \mathbf{E} = -\frac{1}{2m_0ec}\mathbf{p} \times \boldsymbol{\nabla}V(r) = -\frac{e}{2m_0c}\frac{\mathbf{p}\times\mathbf{r}}{r^3}. \tag{2.2}$$

This spin-orbit magnetic field interacts with the spin of the electron through the Zeeman interaction:

$$H_{SO} = -\boldsymbol{\mu}_s \cdot \mathbf{B_{SO}} = \frac{e}{2m_0cr^3}\boldsymbol{\mu}_s \cdot (\mathbf{p}\times\mathbf{r}), \tag{2.3}$$

where:

$$\boldsymbol{\mu}_s = -\frac{g_0\mu_B}{\hbar}\mathbf{S} \tag{2.4}$$

is the magnetic moment of the electron spin in the vacuum. Therefore, the spin-orbit Hamiltonian can be written in terms of the electron's spin state and the electron's angular momentum about the nucleus:

$$H_{SO} = \frac{g_0\mu_B^2}{r^3}\frac{\mathbf{S}\cdot\mathbf{L}}{\hbar^2}. \tag{2.5}$$

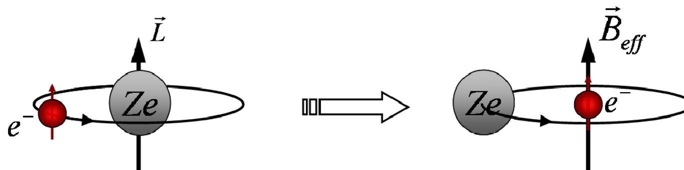

Figure 2.1: (a) Cartoon of electron orbiting nucleus of charge Ze with angular momentum **L**. (b) Cartoon when transformed to the rest frame of the electron. The charged nucleus orbiting the electron creates a magnetic field. The electron spin is in the low energy eigenstate when its spin points in the same direction as the effective magnetic field.

This is the form in which the spin-orbit interaction is typically written in introductory quantum mechanics. However, looking back at Eq. 2.2 and Eq. 2.3 it is clear that the spin-orbit interaction can be written in a much more general form:

$$H_{SO} = \lambda_{SO}^{eff} \boldsymbol{\sigma} \cdot (\mathbf{k} \times \boldsymbol{\nabla} V(r)). \tag{2.6}$$

Here $\boldsymbol{\sigma}$ is a Pauli spin matrix, $\mathbf{k} = \mathbf{p}/\hbar$ and where:

$$\lambda_{SO}^{vacuum} = -\frac{g_0 \hbar^2}{8m_0^2c^2} \approx -\frac{\hbar^2}{4m_0^2c^2} \tag{2.7}$$

is defined as the spin-orbit coupling constant in the vacuum. In the vacuum, we find $\lambda_{SO}^{vacuum} = -3.7 \times 10^{-6}$ Å^2. We will see later that this spin-orbit coupling parameter can be many orders of magnitude larger in solids.

The strength of the spin-orbit interaction depends very strongly on the atomic number of the nucleus. If, instead of orbiting a hydrogen nucleus, the electron is orbiting a nucleus of charge Ze, a factor of Z is introduced into the Coulomb potential in Eq. 2.1. Following this factor of Z through the derivation of the spin-orbit interaction, there will clearly be a factor of Z in the numerator of Eq. 2.5. However, if we also calculate the expectation value of $1/r^3$ we find [38]:

$$< \frac{1}{r^3} >= \int \Psi^* \frac{1}{r^3} \Psi r^2 dr d\Omega \propto Z^3, \tag{2.8}$$

for atomic wave functions Ψ. Therefore, the total spin-orbit Hamiltonian (Eq. 2.5) is proportional to Z^4. The dramatic dependence of the spin-orbit coupling strength

on atomic number will appear again later, when we consider the spin-orbit interaction in solids later in this chapter.

2.2.2 Spin-Dependent Scattering in Vacuum

Thus far we have only discussed spin-orbit coupling in the context of an electron bound to a nucleus. However, a free electron approaching a nucleus will also experience a magnetic field that is described by Eq. 2.2. The magnetic field seen by the electron curls around the nucleus in the direction that is perpendicular to the electron's momentum, as illustrated in Fig. 2.2(a). The electron experiences a force $\mathbf{F} = -\boldsymbol{\nabla}(-\boldsymbol{\mu} \cdot \mathbf{B})$ due to the gradient in the effective magnetic field. An incoming electron with a spin in the $+z$ direction will be scattered to the left, regardless of which side it approaches the nucleus on (see Fig. 2.2(c)). This leads to a scattering cross section that depends on the incoming electron's spin orientation.

Mott first solved for the scattering cross section of an incoming plane wave of electrons incident on a charged nucleus in 1929 [39]. He found that, for an incoming beam of electrons with spin polarization P, two detectors placed at the same angle on opposite sides of the beam would measure different scattering intensities. The measured scattering intensities could be related to the polarization of the incident beam using the relation:

$$\frac{I_R - I_L}{I_R + I_L} = S(\theta) P_{Incident}, \tag{2.9}$$

where $S(\theta)$ is the Sherman function [40, 41]. Alternatively, an unpolarized incident beam would be partially spin separated, such that a spin-sensitive detector at an angle θ would detect a polarization $P = S(\theta)$ in the z direction. It is this separation of unpolarized electrons by way of spin-dependent scattering that gives rise to the extrinsic spin Hall effect that will be discussed in the next chapter.

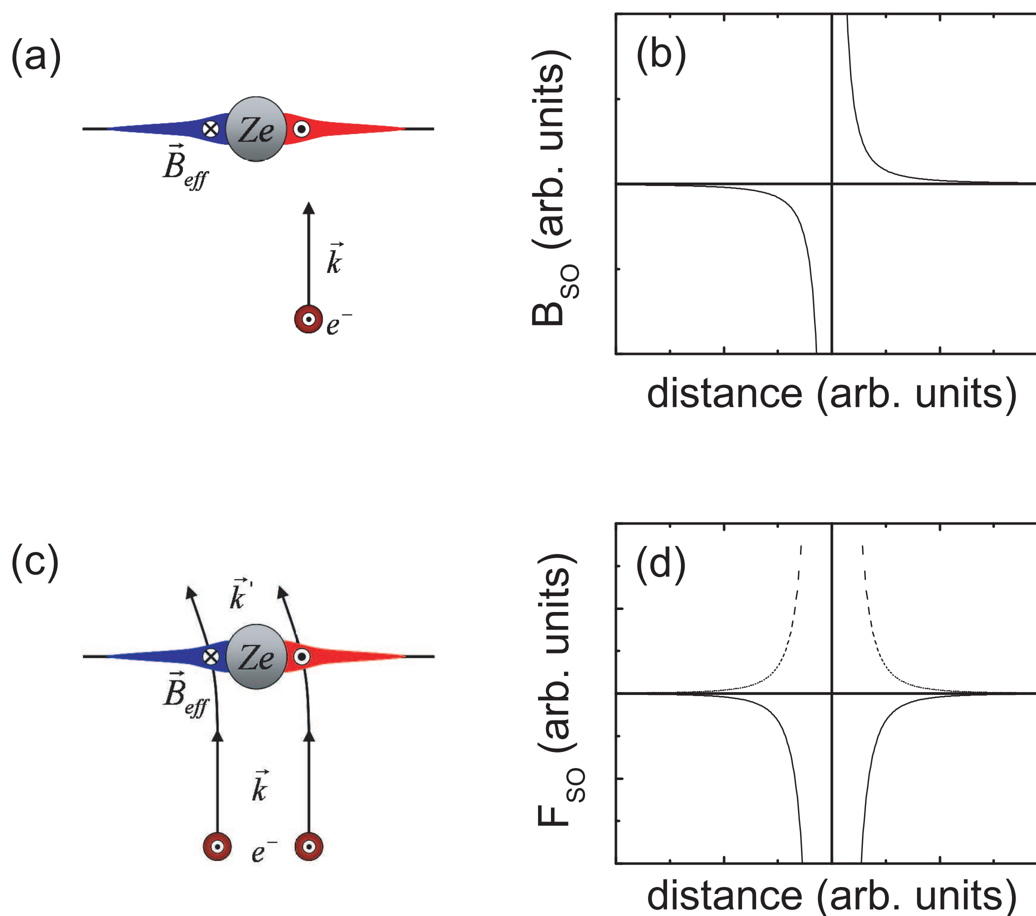

Figure 2.2: (a) Cartoon of magnetic field experienced by electron with incoming momentum **p** approaching a nucleus of charge Ze. (b) Effective magnetic field vs distance from scattering site. (c) Cartoon of incoming spin-up electron on either side of the nucleus being scattered to the left. (d) Force experienced by electron vs distance from scattering site for spin up (solid line) and spin down (dashed line).

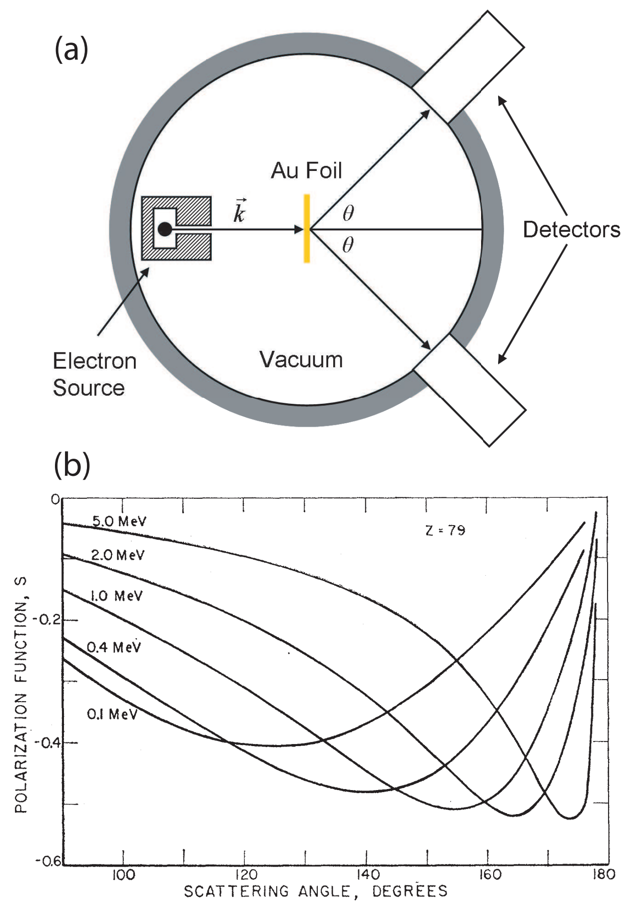

Figure 2.3: (a) Schematic of the experimental setup of a Mott scattering measurement. Energetic electrons are fired at a target (typically a thin gold film due to gold's large spin orbit coupling). Detectors at an angle θ from the incident electron beam detect scattered electrons. (b) Calculated electron polarization vs scattering angle for an initially unpolarized beam of electrons scattering off of gold nuclei at various kinetic energies. The polarization is given as $S(\theta)$, the Sherman function. Figure is derived from Motz *et al.* [42].

2.3 Spin-Orbit Coupling in Solids

Up to this point, we have only discussed the effects of spin-orbit coupling on electron scattering in the vacuum. This section will discuss how the spin-orbit interaction must be modified to take into account the multiple energy bands in crystalline solids. Although this section will focus specifically on semiconductor materials, the general techniques introduced here can be applied to metallic systems as well. We will see that the spin orbit Hamiltonian can be written in the same form as in Eq. 2.6, but with a modified spin-orbit coupling parameter that will depend on the details of the material band structure. This effective spin-orbit coupling parameter can be many orders of magnitude larger than the vacuum value of $\lambda_{SO}^{vacuum} = -3.7 \times 10^{-6}$ Å^2. In GaAs, for example, it has been calculated to be $\lambda_{SO}^{GaAS} \approx 5.3$ Å^2, approximately 6 orders of magnitude larger than the vacuum value [43]. In order to understand this drastic increase, we first need to understand some basics of semiconductor band structure.

2.3.1 Semiconductor Band Structure

A cartoon sketch of the band structure of a direct-gap zinc blende semiconductor such as GaAs or InAs is shown in Fig. 2.4. To a first approximation, there are four relevant bands for electrical transport in GaAs: a conduction band, which has s-like symmetry ($L = 0$), and three valence bands, which have p-like symmetry ($L = \hbar$). Each of these bands is doubly spin degenerate. Near the Γ-point, these bands are approximately parabolic, and the dispersion relation for each band can be written as:

$$E_n(\mathbf{k}) = E_n(0) + \frac{\hbar^2\mathbf{k}^2}{2m^*}, \tag{2.10}$$

where $E_n(0)$ is the energy of the band at the Γ-point, and m^* is an effective mass. The effective mass can be calculated using $\mathbf{k} \cdot \mathbf{p}$ theory and the 8×8 Kane Hamiltonian, which takes into account the coupling between the conduction band

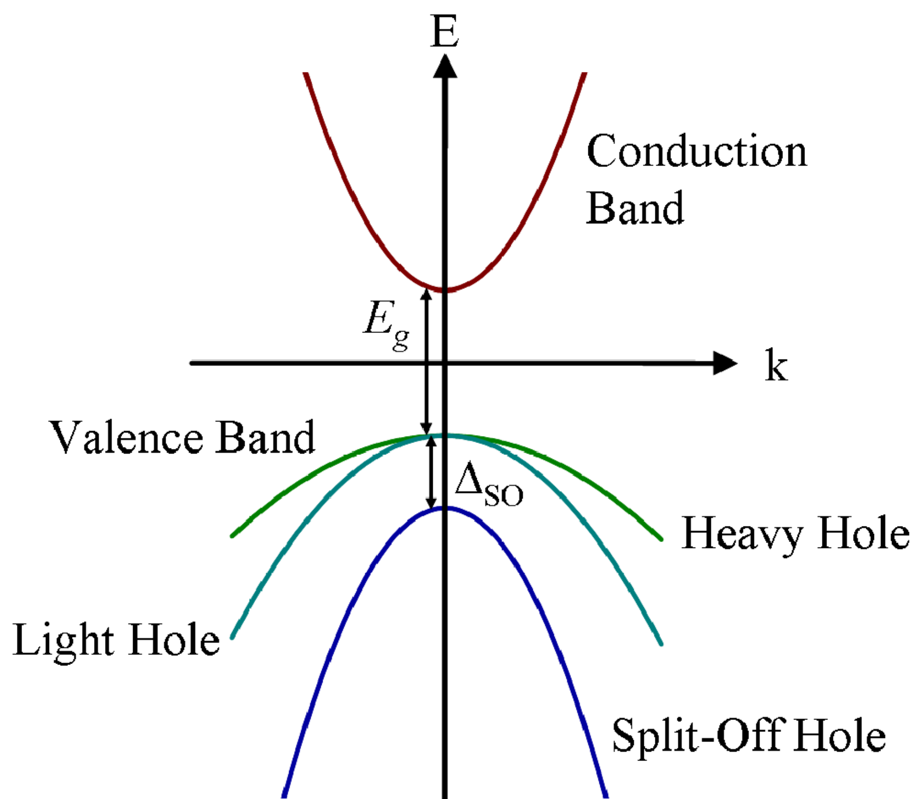

Figure 2.4: Cartoon sketch of the band structure of a zinc blende direct gap semiconductor near the Γ-point. For GaAs, $E_g \approx 1.5$ eV and $\Delta_{SO} \approx 0.34$ eV.

and the 3 valence bands [44, 45]:

$$\frac{1}{m^*} = \frac{1}{m_0} + \frac{2}{\hbar^2}\sum_{n' \neq n} \frac{P_{nn'}^2}{E_n(0) - E_{n'}(0)}, \tag{2.11}$$

where $\mathbf{P}_{nn'} = \frac{-\mathbf{i}\hbar}{m_0} < \Psi_n|\mathbf{p}|\Psi_{n'} >$. Summing over the four bands shown in Fig. 2.4, we find:

$$\frac{1}{m^*} \approx \frac{1}{m_0}\left[1 + \frac{2m_0P^2}{\hbar^2 E_g}\left(1 - \frac{\xi}{3}\right)\right], \tag{2.12}$$

where P^2 is the weighted average of $\mathbf{P}_{nn'}^2$, E_g is the energy gap between the top of the valence band and the bottom of the conduction band, and $\xi = \Delta_{SO}/(E_g + \Delta_{SO})$. Here Δ_{SO} is the energy splitting of the split-off hole band from the heavy and light hole bands, which will be discussed in more detail later in this section. The energy scale of $m_0P^2/\hbar^2$ corresponds approximately to the atomic Rydberg energy, and it is found that $2m_0P^2/\hbar^2 \approx 20$ eV for most semiconductors [44]. The band gap energy is typically ≈ 1 eV, and it depends roughly inversely on the lattice constant of the semiconductor, with larger lattice constants corresponding roughly to smaller band gaps [46]. This is due to the larger overlap of the atomic wave functions for heavier elements. For GaAs, $E_g \approx 1.5$ eV. Figure 2.5 shows the evolution of E_g with increasing In concentration for $In_{1-x}Ga_xAs$. We then find an effective mass for GaAs conduction band electrons $m^* \approx 0.074m_0$; the accepted value is $m^* \approx 0.067m_0$. As m^* is an experimentally well known quantity, in the remainder of this chapter we will use Eq. 2.12 to define P^2 [47].

The valence bands are somewhat more complicated due to their p-like character with orbital angular momentum $L = \hbar$. Taking in to account the spin angular momentum ($S = \hbar/2$), the total angular momentum J of theses states can be either $3\hbar/2$ (four states) or $\hbar/2$ (two states). The $J = 3\hbar/2$ states are degenerate at the Γ-point, and form the heavy and light hole bands. The $J = \hbar/2$ states are lower in energy due to the spin orbit interaction, and form the split-off hole band. The splitting can be calculated from Eq. 2.5, noting that $\mathbf{L} \cdot \mathbf{S} = (J^2 - L^2 - S^2)/2$. As was discussed in Sec. 2.2.1, the atomic spin orbit coupling energy increases

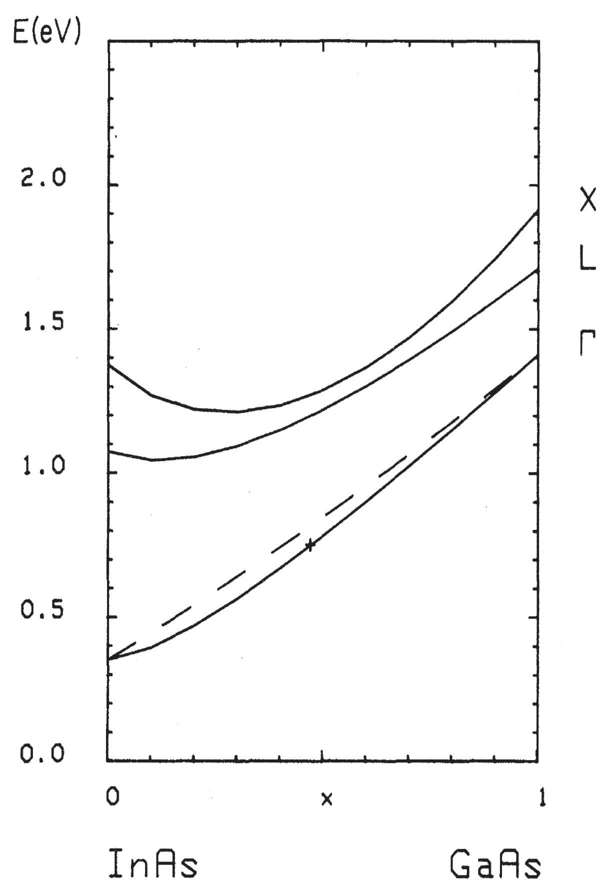

Figure 2.5: E_g vs concentration (x) for $In_{1-x}Ga_xAs$ shows an approximately linear dependence on alloy concentration. The conduction band minimum remains at the Γ-point for all x. Figure derived from Porod and Ferry [48].

	GaP	InP	AlAs	GaAs	InAs	AlSb	GaSb	InSb
a (Å)	5.451	5.869	5.660	5.653	6.058	6.136	6.096	6.479
E_g^{0K} (eV)	2.35	1.42	2.23	1.52	0.42	1.69	0.81	0.23
Δ_{SO} (eV)	0.08	0.11	0.28	0.34	0.38	0.67	0.75	0.98

Table 2.1: Experimentally determined lattice constants, gap energies, and spin-orbit splitting energies of various III-V semiconductor compounds.

roughly as Z^4. To find the energy of the splitting, Δ_{SO}, in an binary semiconductor compound (such as GaAs or InAs), we must weight the atomic spin-orbit energies of the elements A and B according to their contributions to the valence bands [49]:

$$\Delta_{SO}(AB) = \frac{1}{2}(1 - f_i)\Delta_A + \frac{1}{2}(1 + f_i)\Delta_B, \tag{2.13}$$

where Δ_A and Δ_B are the atomic spin-orbit energies of the cation and anion, respectively, and f_i is the ionicity. The anions are weighted more heavily because a greater fraction of the wavefunction overlaps with the anion. For GaAs we find $\Delta_{Ga} = 0.18$ eV, $\Delta_{As} = 0.43$ eV, and $f_i = 0.310$, giving us $\Delta_{SO}^{GaAS} = 0.34$ eV. Table 2.1 lists the lattice constant, gap energy, and spin-orbit splitting energies for several different semiconductors (listed in order of increasing spin-orbit coupling) [46].

2.3.2 Spin-Orbit Coupling in GaAs and InAs

We will now discuss how the semiconductor band structure gives rise to the large spin-orbit coupling parameter in GaAs. The spin-orbit interaction has the same form as in Eq. 2.6, but the spin orbit coupling parameter λ_{SO}^{eff} must be renormalized in a way similar to the renormalization of the effective mass. Again, using the 8×8 Kane Hamiltonian, λ_{SO}^{eff} is found to be [49]:

$$\lambda_{SO}^{eff} = \frac{P^2}{3E_g^2}\left[1 - (1 - \xi)^2\right]. \tag{2.14}$$

This expression can be rewritten in a more dimensionally transparent form:

$$\lambda_{SO}^{eff} = -\lambda_{SO}^{vacuum} \times \frac{2m_0c^2}{E_g} \times \frac{m_0}{\hbar^2 E_g/2P^2} \times \frac{1}{3}\left[1-(1-\xi)^2\right]. \tag{2.15}$$

In the above expression, origin of the factor of 10^6 enhancement in λ_{SO}^{GaAs} from the vacuum value is more clear. The small parameter in perturbation theory controlling the spin-orbit interaction in the vacuum is:

$$\frac{\hbar^2 k^2/2m_0}{2m_0c^2}, \tag{2.16}$$

where $\hbar^2 k^2/2m_0$ is the kinetic energy of the electron and $2m_0c^2$ is the total energy difference between the electron and positron states in the vacuum [50]. In a semiconductor, the kinetic energy of the electron is enhanced by a factor of m_0/m^*. From Eq. 2.12 we find:

$$\frac{m_0}{m^*} \approx \frac{m_0}{\hbar^2 E_g/2P^2}. \tag{2.17}$$

Additionally, rather than comparing the electron's kinetic energy to $2m_0c^2 \approx$ 1 MeV, we must now compare it to $E_g \approx 1$ eV, the energy difference between the conduction and valence bands in the semiconductor. The combination of these two factors leads to the 10^6 enhancement in λ_{SO}^{GaAs} over the vacuum value. Semiconductors with smaller gap energies and larger spin-orbit splitting energies will exhibit much larger spin-orbit coupling. It is also apparent that in the limit $\xi \to 0$, then $\lambda_{SO}^{eff} \to 0$.

The electron g-factor is also renormalized in a similar way. Roth *et al.* arrived at the following expression for the effective electron g-factor [49, 51]:

$$g^* = g_0\left[1 - \frac{4}{3}\frac{m_0P^2}{\hbar^2 E_g}\xi\right]. \tag{2.18}$$

Figure 2.6 shows both λ_{SO}^{eff} and g^* as a function of increasing In concentration for $In_{1-x}Ga_xAs$. Both parameters increase by more than an order of magnitude from GaAs to InAs. This difference can be attributed to the fact that in GaAs $E_g \approx 1.5$ eV, whereas in InAs $E_g \approx 0.4$ eV, while $\Delta_{SO} \approx 0.35$ eV for both GaAs and InAs. Note that in both GaAs and InAs, λ_{SO}^{eff} and g^* are opposite in sign from their values in the vacuum.

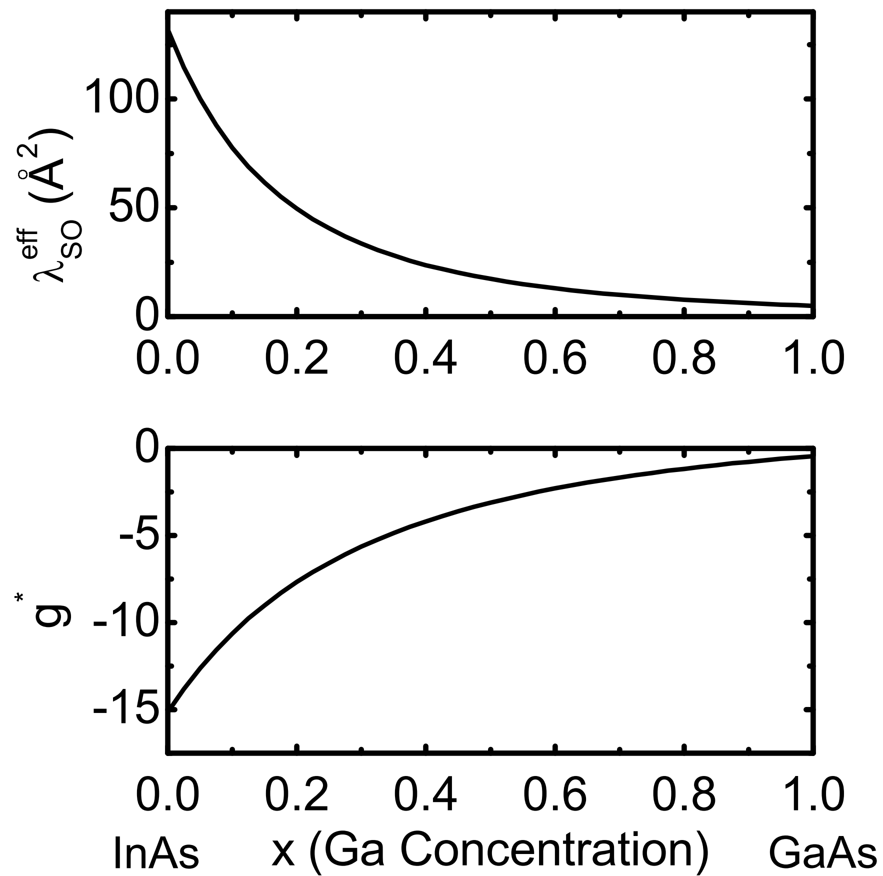

Figure 2.6: (a) λ_{SO}^{eff} vs concentration (x) for $\mathrm{In}_{1-x}\mathrm{Ga}_x\mathrm{As}$. The spin-orbit coupling parameter increases quadratically with increasing In concentration, leading to drastically larger spin-orbit coupling in InAs than in GaAs. (b) g^* vs concentration (x) for $\mathrm{In}_{1-x}\mathrm{Ga}_x\mathrm{As}$. The effective electron g-factor increases by more than a factor of 30 between GaAs and InAs.

2.4 The Anomalous Hall Effect

The earliest evidence of spin-dependent scattering effects was a measurement of the anomalous Hall effect performed by Hall himself in 1880 [52]. In a typical Hall measurement geometry, shown in Fig. 2.7, a charge current flows down a sample in the x direction. A magnetic field is applied in the z direction, perpendicular to the plane of the sample. The Hall voltage is then measured between opposite edges of the sample in the y direction. For a magnetic field applied in the $\hat{z}$ direction, the Lorentz force deflects electrons in y direction. This causes a voltage to build up across the edges of the sample. In non-magnetic materials, this voltage is proportional to the strength of the applied magnetic field.

Hall found that in ferromagnetic metals, the measured Hall voltage depended strongly on the magnetization of the ferromagnet, and that the voltage was approximately constant for applied fields large enough to saturate the the magnetization. It was not until 1929 that it was proposed that the Hall resistivity could be written as the sum of two parts, one that was proportional to the applied magnetic field and one that was proportional to the magnetization [53]:

$$\rho_{AH} = -\rho_{xy} = R_0 B_z + 4\pi R_S M_z. \tag{2.19}$$

The value of R_S, the 'anomalous' Hall constant, is usually much larger than the value of R_0, the 'ordinary' constant, as can be seen for nickel in Fig. 2.7 [54]. If $T < T_C$, ρ_{AH} increases rapidly when $B_z < 4\pi M_S$, due to the increase in M_z with increasing B_z. The magnetization is saturated when $B_z > 4\pi M_S$, and the slope of ρ_{AH} vs B_z returns to that of the ordinary Hall effect. If $T > T_C$, then ρ_{AH} increases linearly with B_z, but with a slope that represents both the ordinary Hall effect and the anomalous Hall effect due to the paramagnetic susceptibility of the ferromagnet.

It was also found that ρ_{AH}, normalized to $M_S(T)$, increases greatly with temperature (see Fig. 2.8). In 1930 Albert Perrier noted that the temperature dependence of the Hall conductivity, defined as $\sigma_{AH} \approx \rho_{AH}/\rho_{xx}^2$, was much smaller and

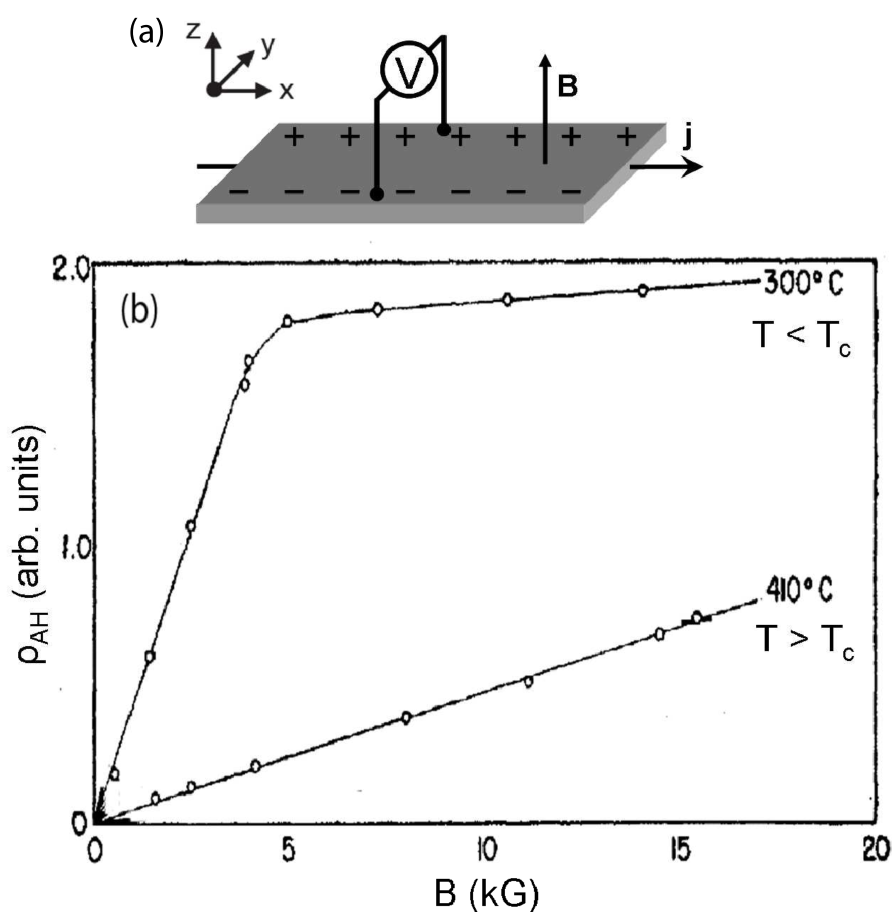

Figure 2.7: (a) Hall measurement geometry. (b) ρ_{AH} vs. applied field for Ni above and below T_C. For $T < T_C$, ρ_{AH} increases dramatically with increasing field, due to the increase in M_z. The slope above $B \approx 5$ kG is the ordinary Hall slope. For $T > T_C$ Ni is paramagnetic, so the ordinary and anomalous Hall effects are superimposed. Figure derived from Pugh and Rostoker [54].

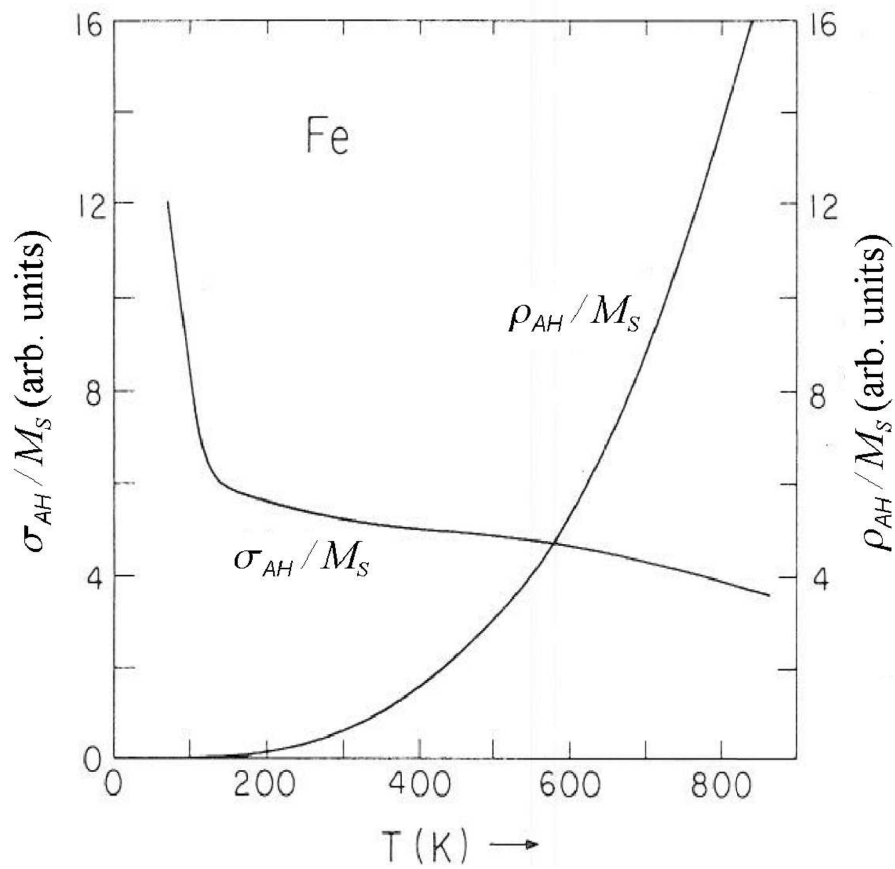

Figure 2.8: Plot of ρ_{AH}/M_S vs Temperature (right axis) and σ_{AH}/M_S (left axis) for iron. Classical scattering theory predicts that $\rho_{AH}/M_S \propto \rho_{xx}(T)$, whereas data show that for iron $\rho_{AH}/M_S \propto (\rho_{xx}(T))^2$ [55]. Plotting σ_{AH}/M_S vs Temperature shows that σ_{AH}/M_S is approximately constant above 100 K.

simpler than that of ρ_{AH} [56]. This suggested that the anomalous Hall effect depends on electron scattering events [55]. Since the anomalous Hall effect depends on the magnetization, which is parallel to the spin polarization of the ferromagnet, it was deduced that spin-orbit coupling must be affecting the electron scattering process. Since the charge current flowing through a ferromagnet is spin polarized, spin dependent scattering leads to a charge imbalance across the ferromagnet, giving rise to the anomalous Hall voltage. However, it was impossible to explain the strong temperature dependence of ρ_{AH} using the scattering theory developed by Mott, discussed in Sec. 2.2.2. A more accurate description of the scattering process can be found if the scattering of a wave packet is considered rather than a plane wave. This scenario will be discussed in the next section.

2.5 Skew and Side-Jump Scattering

The problem of an incident plane wave scattering from a spherical scattering potential V_0 (a reasonable approximation to a screened Coulomb potential) was solved by Smit in 1958 [57]. His solution was later expanded upon by Berger to solve the scattering problem for an incident wave packet with average wave vector k_0 [58]. The following is a summary of their results. The relevant Hamiltonian for the scattering problem can be written as $H = H_0 + H_{SO}$, where:

$$V(r) = \left\{ \begin{array}{ll} -V_0 & \text{if } r < R \\ 0 & \text{if } r > R \end{array} \right\}, \tag{2.20}$$

$$H_0 = -\frac{\hbar^2}{2m_e}\boldsymbol{\nabla}^2 + V(r), \tag{2.21}$$

$$H_{SO} = \lambda_{SO}^{eff}\boldsymbol{\sigma} \cdot (\mathbf{k} \times \boldsymbol{\nabla} V). \tag{2.22}$$

Letting $\psi = \psi_0 + \psi_{SO}$, one can first solve the scattering problem for H_0 and ψ_0, then one can use perturbation theory to find ψ_{SO}. Once this is done, one can

calculate $< y >$, the expectation value of the y position of the wave packet. Berger found that this expectation value had two terms, one which is linear in t and one which is time-independent. These two contributions are shown schematically in Fig. 2.9. The time-dependent term can be interpreted classically as a change in the wave packet's y momentum and is referred to as skew scattering. The amount of change in the electron's momentum will depend on the details of the scattering potential. The time-independent term is quantum mechanical in nature. It can be thought of as a localized motion of the electron inside the impurity potential, and has been historically termed an "anomalous current". This term is referred to as side-jump scattering, because the electron experiences a shift in its position with each scattering event. Interestingly, the side-jump term is independent of the strength, range, and sign of the scattering potential. Both the skew and side-jump terms will be discussed in greater detail in Chapter 3; for now we will treat them phenomenologically.

Let us define a scattering angle for skew scattering, $\gamma_{SS} = p_y/p_x$, and a scattering angle for side jump scattering, $\gamma_{SJ} = \Delta y/L_p$, where L_p is the mean free path between scattering events. We can then define an anomalous Hall angle as:

$$\gamma_{AH} = \frac{\rho_{AH}}{\rho_{xx}} = \gamma_{SS} + \gamma_{SJ}. \tag{2.23}$$

Since the mean free path is inversely proportional to the resistivity, we can rewrite the side-jump term as $\gamma_{SJ} = \rho_{xx}/\rho_{SJ}$. Multiplying γ_{AH} by ρ_{xx} then yields:

$$\rho_{AH} = \rho_{xx}\gamma_{SS} + \rho_{xx}^2/\rho_{SJ}. \tag{2.24}$$

Writing ρ_{AH} in this form greatly helps to explain experimental data where it was reported that $\rho_{AH}(T) \propto (\rho_{xx}(T))^n$, where n ranged from 1 to 2, depending on the material (see Fig. 2.8). The classical picture of skew scattering developed by Mott, which predicts $n = 1$, cannot explain the observed temperature dependence. The situation becomes more clear when, as was first suggested by Albert Perrier,

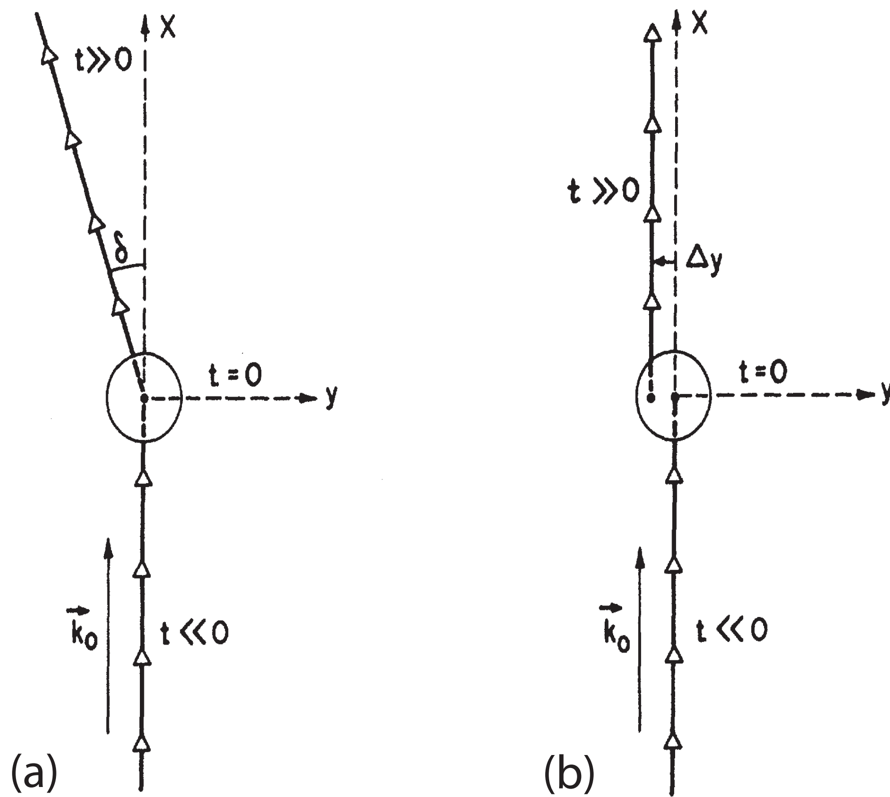

Figure 2.9: Diagram of scattering of an electron wavepacket with average wave vector $\mathbf{k}_0$ when scattering from an attractive spherical potential well [58]. The spin is oriented out of the scattering plane. Skew scattering is represented in (a), where the electron experiences a change in momentum $\delta p_y \propto s_z k_x$. Side-jump scattering is shown in (b), where the electron experiences a lateral displacement $\delta y \propto s_z k_x$ at the scattering site. Although these effects are shown separately here, they are actually always superimposed.

we look at the anomalous Hall conductivity rather than the resistivity. Dividing ρ_{AH} by ρ_{xx}^2, we find:

$$\sigma_{AH} = \frac{\rho_{AH}}{\rho_{xx}^2} = \gamma_{SS}\sigma_{xx} + \sigma_{SJ}. \tag{2.25}$$

From this expression the temperature dependence of σ_{AH} (see Fig. 2.8) becomes clear. At low temperatures, when σ_{xx} is large, the skew scattering term dominates σ_{AH}. Above $T \approx 100$ K, however, σ_{xx} is small, and σ_{AH} approaches a constant value corresponding to σ_{SJ}.

In the next chapter, we will discuss the spin Hall effect, a phenomena closely related to the anomalous Hall effect. Measurements of the spin Hall effect in semiconductors will allow us to quantify the relative magnitudes of skew and side-jump scattering, as well as to estimate the magnitude of the spin-orbit coupling parameter.

Chapter 3

The Spin Hall Effect

In Chapter 2 we discussed how spin-orbit coupling gives rise to the spin-dependent scattering of electrons from impurity potentials. The first observations of spin-dependent scattering in solids were measurements of the anomalous Hall effect in ferromagnetic metals. Although this effect was first discovered in the late 1800's, its microscopic origin was not well understood until the mid 1900's. In 1971, D'yakonov and Perel predicted from a phenomenological model that spin-orbit coupling should lead to a new family of Hall effects that have come to be known generally as the spin Hall effect (SHE) [59, 60]. In this chapter we will discuss this family of effects, and we will focus specifically on the electrical measurement of the direct spin Hall effect (dSHE) which will provide substantial insight into the effects of spin-dependent scattering and spin-orbit coupling in semiconductor systems. Spin-orbit effects which arise due to scattering are generally classified as "extrinsic" effects, because they arise from scattering off of impurity potentials. Later, in Chapter 4, we will discuss a class of spin-orbit effects called "intrinsic" effects, which arise due to the inherent band structure of a crystalline material.

3.1 The Family of Spin Hall Effects

Here we will summarize D'yakonov and Perel's phenomenological description of the SHE [59]. From Ohm's law and Fick's law we can write an expression for the charge current density as:

$$\frac{\mathbf{j}^0}{e} = \mu n \mathbf{E} + D \boldsymbol{\nabla} n, \tag{3.1}$$

where μ is the mobility, n is the carrier density, $\mathbf{E}$ is the electric field, and D is the diffusion constant. The superscript ^{0} indicates that spin-orbit effects have not yet been taken in to account. We now define a spin current density $q_{i,j}$, where i is the direction of flow and j is the axis of spin polarization:

$$q_{i,j} \equiv -\frac{j_{i,+j} - j_{i,-j}}{e}. \tag{3.2}$$

Now we can write an expression very similar to Eq. 3.1 for the spin current $q_{i,j}$:

$$q^0_{i,j} = -\mu E_i p_j - D \frac{\partial p_j}{\partial x_i}, \tag{3.3}$$

where p_j is the spin polarization density.

As we saw in Chapter 2, the spin-orbit interaction (Eq. 2.6) causes electrons traveling in the x direction with spins polarized in the z direction to be deflected in the y direction. This leads to a coupling of the charge current and spin current that can be written as:

$$\frac{\mathbf{j}}{e} = \frac{\mathbf{j}^0}{e} - \gamma \epsilon_{ijk} q^0_{j,k}, \tag{3.4}$$

$$q_{i,j} = q^0_{i,j} + \gamma \epsilon_{ijk} \frac{j^0_k}{e}, \tag{3.5}$$

where γ is a dimensionless parameter proportional to the spin-orbit coupling strength that corresponds to the average angle of deflection of a spin polarized electron. Replacing $\mathbf{j}^0$ and $q^0_{i,j}$ with Eqs. 3.1 and 3.3 we find:

$$\frac{\mathbf{j}}{e} = \mu n \mathbf{E} + D \boldsymbol{\nabla} n + \gamma \mu \mathbf{E} \times \mathbf{p} + \gamma D \boldsymbol{\nabla} \times \mathbf{p}, \tag{3.6}$$

$$q_{i,j} = -\mu E_i p_j - D\frac{\partial p_j}{\partial x_i} + \gamma\mu\epsilon_{ijk}E_k + \gamma D\epsilon_{ijk}\frac{\partial n}{\partial x_k}. \tag{3.7}$$

For the charge current, we use the typical continuity equation:

$$\frac{\partial n}{\partial t} + \mathbf{\nabla} \cdot \mathbf{j} = 0. \tag{3.8}$$

However, because spin is not conserved, for the spin current we must use a modified continuity equation to take into account the effects of spin relaxation:

$$\frac{\partial p_j}{\partial t} + \frac{\partial q_{i,j}}{\partial x_i} + \frac{p_j}{\tau_s} = 0. \tag{3.9}$$

The terms in Eqs. 3.6 and 3.7 can describe all of the phenomena in the family of spin Hall effects. The anomalous Hall effect, which was discussed in Sec. 2.4, is described by the third term in Eq. 3.6, $\gamma\mu\mathbf{E} \times \mathbf{p}$. In the geometry shown in Fig. 2.7, there is an electric field applied along the x-direction, and there is a spin polarization in the z-direction due to the applied magnetic field. Therefore $\mathbf{E} \times \mathbf{p}$ is in the y-direction, and a voltage builds up across the sides of the sample. The fourth term in Eq. 3.6 and the third term in Eq. 3.7 give rise to the inverse spin Hall effect (iSHE) and direct spin Hall effect (dSHE), respectively. These last two effects will be discussed in more detail in the following sections.

3.2 The Inverse Spin Hall Effect

The fourth term in Eq. 3.6, $\gamma D\mathbf{\nabla} \times \mathbf{p}$ is known as the inverse spin Hall effect (iSHE). In a way similar to the anomalous spin Hall effect, the inverse spin Hall effect causes a charge current that is perpendicular to the direction of spin polarization. However, unlike the anomalous Hall effect, a longitudinal electric field is not necessary to observe the effect. Rather, it is driven by a diffusive spin current.

3.2.1 Optically Pumped Inverse Spin Hall Effect

The inverse spin Hall effect was first observed by Bakun *et al.* in 1984 by optically pumping spin polarized electrons in semiconductors [61]. The experimental

geometry used by Bakun *et al.* is shown in Fig. 3.1. Two indium contacts were placed on the surface of an $Al_{0.27}Ga_{0.73}As$ crystal to serve as voltage detectors. Circularly polarized light was used to optically pump spin polarized electrons with the spin oriented in the z-direction. These spin polarized electrons are generated at the sample surface, and so there is a spin polarization gradient which is also in the z-direction. When the applied field is zero, the spin polarization and the spin gradient point in the same direction, so $\nabla \times \mathbf{p} = 0$. A magnetic field is applied along the x-axis, which precesses the z-oriented spins into the y-direction. This induces a charge current flowing in the x-direction due to the spin-orbit scattering of spin polarized electrons diffusing in the z-direction. This current can be detected by measuring the voltage between the two indium contacts on the sample surface, and is plotted in Fig. 3.1(b). The resulting curve is the odd component of the Hanle curves discussed in Chapter 1, where a maximum signal is observed when on average the spins have precessed through approximately 90 degrees. The authors showed that this curve exhibited the same dephasing time as an independent optical measurement of the dephasing of the electron spin polarization due to the Hanle effect.

3.2.2 All-Electrical Inverse Spin Hall Effect in Metals

The inverse spin Hall effect was first detected in an all-electrical measurement configuration in metallic systems in 2006 by Valenzuela and Tinkham [62]. A SEM image of a device used to measure the iSHE is shown in Fig. 3.2(a). Samples were prepared by using electron beam lithography to define a shadow mask, and a two-angle deposition technique to first grow an aluminum Hall cross, and then to grow two $Co_{0.80}Fe_{0.20}$ ferromagnetic contacts. The surface of the aluminum was oxidized to form a tunnel barrier and thus provide a high spin injection efficiency [18]. Electrical spin injection was confirmed by performing a non-local Hanle measurement as described in Chapter 1. The measurement geometry and the resulting data are shown in Fig. 3.2(a) and (b). In this geometry, at zero

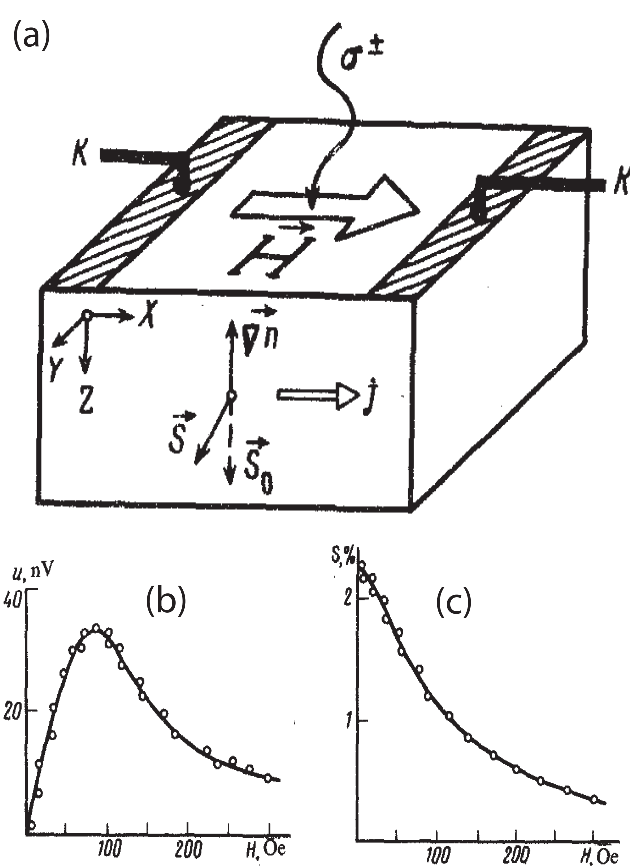

Figure 3.1: (a) Inverse spin Hall effect measurement geometry used by Bakun *et al.* [61]. (b) Plot of electrically measured Hanle signal as a function of applied magnetic field. (c) Plot of Hanle signal measured using optical Kerr rotation shows the same half-width. Figures derived from Ref. [61].

applied field, electrons are injected with a spin polarization that is in the plane of the device, along the easy axis of the ferromagnetic contact. A magnetic field is applied out of the plane of the device to precess and dephase the electron spins. The voltage is measured between a nearby ferromagnetic contact and a reference electrode, and from the resulting signal the injected spin polarization and spin diffusion length in the aluminum can be determined.

To measure the inverse spin Hall effect, Valenzuela and Tinkham measured the voltage across the aluminum Hall bar while injecting spin polarized electrons from a nearby ferromagnetic contact, as shown in Fig. 3.2(c). In this geometry, the spin polarization must be oriented out of the plane of the device in order to measure a non-zero Hall voltage. The magnetization of the ferromagnetic contacts (and hence the injected spin polarization) is tilted out of plane by applying a large magnetic field. This induces a voltage across the aluminum Hall cross that is proportional to the z component of the magnetization. To provide further evidence that the measured voltage is due to the inverse spin Hall effect, the authors also varied the distance between the ferromagnetic injection contact and the Hall cross. They found that the Hall signal decays exponentially over the length scale of the spin diffusion length, indicating that the measured Hall voltage depends on the diffusion of the non-equilibrium spin polarization.

3.2.3 All-Electrical Inverse Spin Hall Effect in Semiconductors

The approach used by Valenzuela and Tinkham to measure the inverse spin Hall effect in metals seems like a natural approach to try in semiconductors. The principles of electrical spin injection and spin transport in semiconductors, discussed in Chapter 1, are relatively well understood. However, the much smaller carrier concentration in semiconductors complicates the measurement for two reasons. First, in metallic systems, voltages from Hall effects are often negligible, whereas

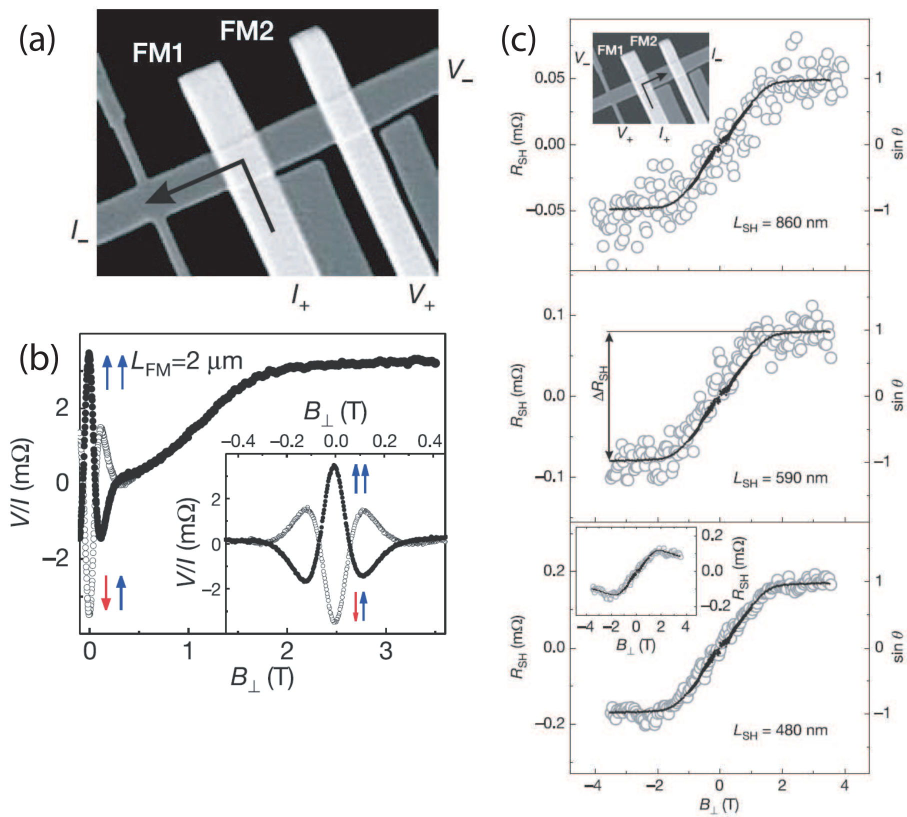

Figure 3.2: (a) SEM image of the inverse spin Hall device used by Valenzuela and Tinkham [62] (b) Plot of voltage observed as a function of applied magnetic field in non-local Hanle measurement configuration. (c) Plot voltage measured across the aluminum Hall cross as a function of applied magnetic field at various separations.

in semiconductors they can be quite large. Secondly, the small carrier concentration in semiconductors means that a significant fraction of the electrons will be bound to donor atoms at low temperatures. This leads to a coupling between the electron spin and the nuclear spins in GaAs [11, 28, 63]. The induced magnetic field due to spin polarized nuclei can make interpretation of field dependent data significantly more complicated.

The ordinary Hall effect is inversely proportional to the carrier concentration in a sample. In metallic systems, the electron concentration is $\approx 10^{22}$ cm^{-3}, whereas the semiconductor heterostructures discussed in Chapter 1 are doped at $n \approx 5 \times 10^{16}$ cm^{-3}. This leads to Hall effects that are roughly 6 orders of magnitude larger than in metallic systems. Hall voltages will arise not only from the external out-of-plane applied field, but also from the fringe fields of nearby ferromagnetic contacts. The fringe fields resulting from a thin film magnetized in the z-direction as shown in Fig. 3.3(b) can be calculated using the following expression:

$$\mathbf{H}(\mathbf{r}) = \frac{1}{4\pi} \iint d^2r' \mathbf{n}' \cdot \mathbf{M}(\mathbf{r}') \frac{(\mathbf{r} - \mathbf{r}')}{|\mathbf{r} - \mathbf{r}'|^3}. \tag{3.10}$$

These fringe fields can be on the order of 100 Oe, and the corresponding voltages are referred to as "local Hall effects," because they vary strongly with distance from the ferromagnetic contact. These local Hall effects make it extremely difficult to interpret a Hall voltage if the magnetization of the spin injection electrode is rotating, as in the Valenzuela and Tinkham geometry [14, 64–68].

An alternative vertical device geometry was suggested by Zhang in 2001 [69] and is pictured in Fig. 3.4(a). In this device, spin polarized electrons are injected from a ferromagnetic contact into the semiconductor and travel away from the ferromagnet/semiconductor interface by both drift and diffusion. In this geometry both the anomalous Hall effect and intrinsic spin Hall effect terms in Eq. 3.6 will contribute to a transverse charge current due to spin-dependent scattering. Under steady state conditions, $j_x = j_y = 0$, and Hall voltage measured across the sample edges can be related to the electron spin polarization. If a magnetic field is applied

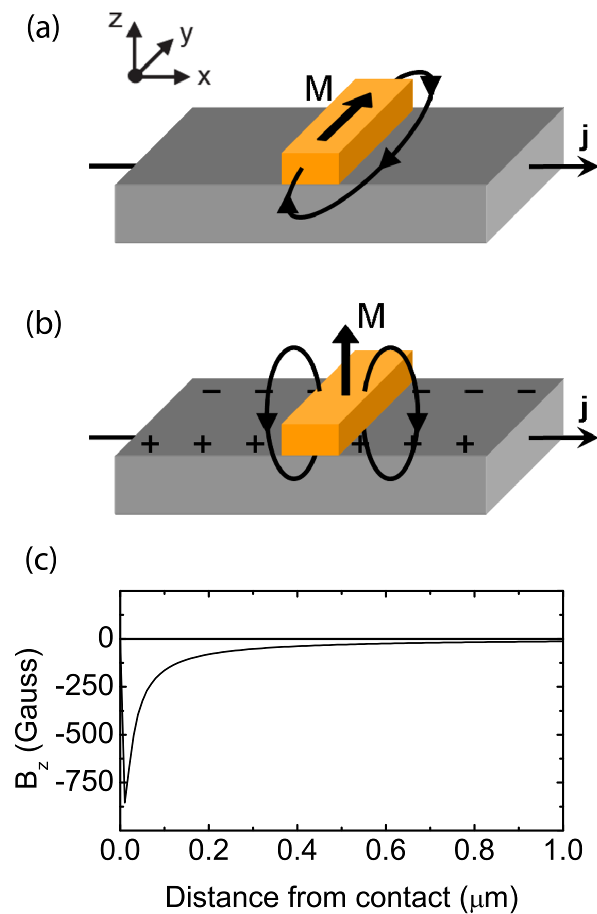

Figure 3.3: (a) Cartoon of fringe fields from a thin ferromagnetic film magnetized in the y-direction. In this configuration, there are minimal local Hall effects. (b) Cartoon of fringe fields from a thin ferromagnetic film magnetized in the z-direction. In this configuration, fringe fields can cause large local Hall effects. (c) Plot of magnetic field vs. distance from contact calculated using Eq. 3.10 for a contact saturated in the z direction.

in the z direction, the ensemble spin polarization can be dephased using the Hanle effect. The field required to dephase the spin polarization is small compared to the out-of-plane saturation field of the ferromagnet, so the magnetization can be considered to be effectively fixed. The resulting Hall voltage as a function of applied magnetic field will have a different characteristic shape depending on the orientation of the contact magnetization, as shown in Fig. 3.4(b) and (c).

Mun Chan from Paul Crowell's group performed numerous measurements on devices structured similar to that depicted in Fig. 3.4(a) [28]. Interestingly, it was found that the measured Hall voltage depended not only on the electron spin polarization, but also on the nuclear spin polarization. The magnitude of the measured effect was approximately 100 times larger than predicted for spin-dependent scattering from Coulomb-like scattering centers in GaAs. A satisfactory theoretical explanation for the microscopic origins of the effect is still elusive. Unfortunately, it is difficult to quantify the spin-orbit coupling without a better understanding of how the nuclear spins determine the spin-dependent transport. Mun Chan's thesis provides an extensive discussion of the experimental results and analysis [28].

3.3 The Direct Spin Hall Effect

In both the anomalous Hall effect and the inverse spin Hall effect, a charge current is induced by the movement of spin polarized electrons. This charge current leads to a potential drop across a sample that can be measured using an ordinary four wire measurement technique. In the spin Hall effect, which results from the term $\gamma\mu\epsilon_{ijk}E_k$ in Eq. 3.7, no such potential drop exists. Instead, there is an opposing gradient in the spin up and spin down electrochemical potentials. This results in a spin accumulation that is opposite in sign at opposite edges of the sample, while the net charge imbalance at the edges of the sample remains zero.

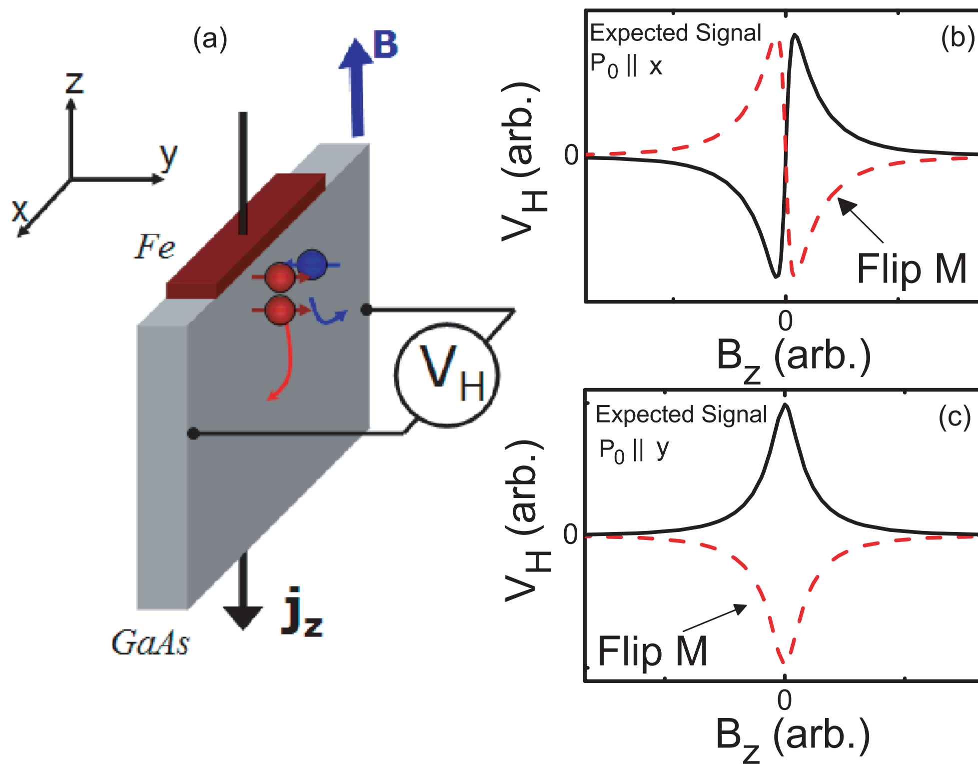

Figure 3.4: (a) Cartoon of device design to detect the inverse spin Hall effect using a vertical device geometry as proposed in [69] and used by Mun Chan [28]. (b) Expected Hall signal as a function of applied field when the magnetization is oriented in the x-direction. (c) Expected Hall signal as a function of applied field when the magnetization is oriented in the y direction.

3.3.1 Spin Orientation From the Direct Spin Hall Effect

In this section we will derive the spatial profile of the spin polarization density that arises due to the direct spin Hall effect, taking Eq. 3.7 from [59] as our starting point. A cartoon representation of the spin Hall effect is shown in Fig. 3.5(a). In the cartoon, an electric field is applied along the x-direction of a non-magnetic Hall bar. Spin dependent scattering then separates electrons with spins oriented along the z direction. In the cartoon, electrons with spins in the $+z$ direction are scattered more strongly into the $+y$ direction, whereas electrons with spins in the $-z$ direction are scattered into the $-y$ direction. Thus, a spin current $q_{y,z}$ is induced by an unpolarized charge current j_x.

In the steady state, $\partial p_j/\partial t = 0$, so from the continuity Eq. 3.9 we see that $\partial q_{y,z}/\partial y = p_z/\tau_s$. Differentiating both sides of Eq. 3.7 with respect to y gives:

$$\frac{\partial q_{y,z}}{\partial y} = -D\frac{\partial^2 p_z}{\partial y^2} = -\frac{p_z}{\tau_s}. \tag{3.11}$$

The solution to this differential equation is easily seen to be of the form:

$$p_z(y) = C_1 e^{+y/L_s} + C_2 e^{-y/L_s}, \tag{3.12}$$

where $L_s = \sqrt{D\tau_s}$, and where we have taken $y = 0$ to be the center of the sample. By symmetry, we know that $C_2 = -C_1$. At the sample boundaries, $q_{y,z}$ must go to zero. From this boundary condition we can determine:

$$C_1 = \frac{\gamma\mu n E_x L_s}{2D\cosh\left(\frac{w}{2L_s}\right)}. \tag{3.13}$$

Finally, we arrive at the following expression for $p_z(y)$:

$$p_z(y) = \frac{\gamma\mu n E_x L_s}{D}\frac{\sinh\left(\frac{y}{L_s}\right)}{\cosh\left(\frac{w}{2L_s}\right)} = q_{y,z}\frac{\tau_s}{L_s}\frac{\sinh\left(\frac{y}{L_s}\right)}{\cosh\left(\frac{w}{2L_s}\right)}. \tag{3.14}$$

where $q_{y,z} = \gamma\sigma_{xx}E_x/e$ is the spin current generated by the SHE. An expression identical to Eq. 3.14 was derived by Zhang in 2000 by solving a semiclassical

Boltzmann equation using the two spin channel model in a ferromagnetic metal, then generalizing the result to a non-magnetic metal [70]. Because the problem is symmetric, we know $\mu_\uparrow = -\mu_\downarrow$ for all y. The polarization density $p_z(y)$ can be related to the spin up and spin down electrochemical potentials using the Eq. 1.11. The resulting spin accumulation is plotted in Fig. 3.5(b) for the case of $w = 10L_s$.

3.3.2 Optical Measurement of the Direct Spin Hall Effect

The spin Hall effect was first detected optically in GaAs by Kato *et al.* in 2004 [71]. Hall bars were fabricated from n-doped GaAs and $In_{0.07}Ga_{0.93}As$ wafers doped at $n = 3 \times 10^{16}$ cm^{-3}. Both samples were grown on (001) semi-insulating GaAs substrates by on molecular beam epitaxy. A 2 μm thick undoped $Al_{0.4}Ga_{0.6}As$ buffer layer was grown on each substrate before the channel growth. In the GaAs sample, the n-doped channel was 2 μm thick, and in the $In_{0.07}Ga_{0.93}As$ sample the n-doped layer was 500 nm thick and capped with a 100 nm undoped GaAs layer. Electrical contact to the n-doped layers was made by annealing Au/Ge/Ni electrodes. A schematic of the device geometry and measurement scheme is shown in Fig. 3.6(a). An electric field is applied along the y direction, creating a spin current $q_{x,z}$ due to spin-orbit coupling. This leads to an an accumulation of out-of-plane spins at the sample edges that is opposite in sign at opposite edges of the sample. A linearly polarized beam tuned to an energy just below the band gap is incident normal to the sample. The reflected beam's polarization is then rotated due to the magneto-optical Kerr effect, as discussed in Chapter 1. A measurement of the Kerr rotation of the reflected beam can be directly related to the spin polarization in the GaAs. A magnetic field is then applied along the x direction to precess and dephase the spin accumulation via the Hanle effect. Figure 3.6(b) shows the resulting Kerr signal as a function of applied field for two locations on opposite edges of the GaAs sample. As is expected for the SHE, the two curves are opposite in sign. The solid lines are fits to a Lorentzian function

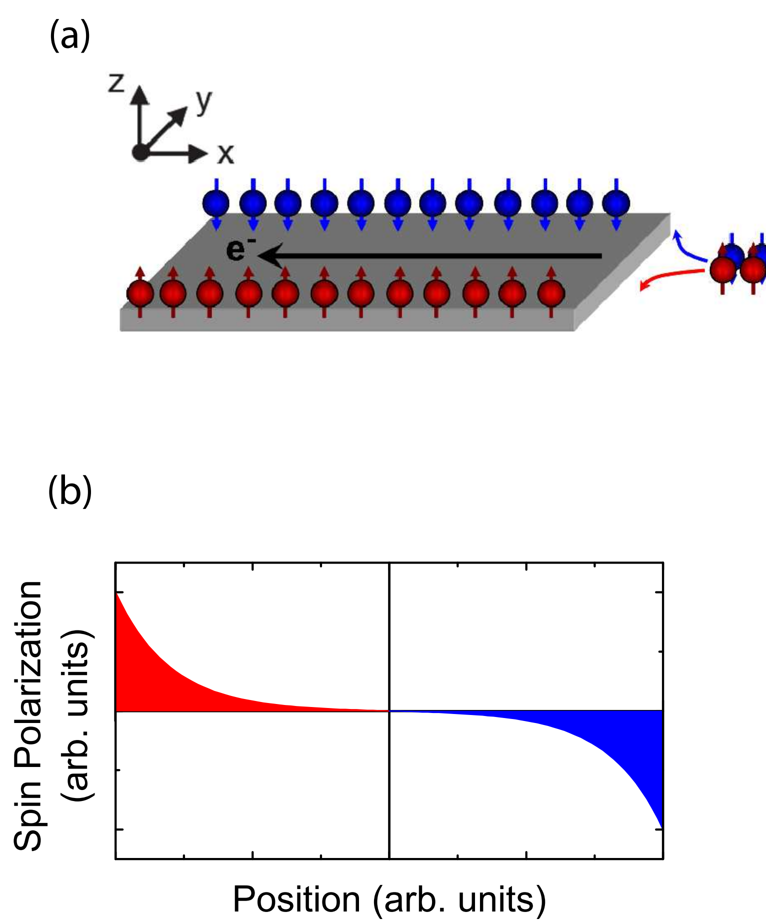

Figure 3.5: (a) Cartoon representation of the spin Hall effect. (b) Expected spin accumulation as a function of distance from sample edges.

of the form:

$$A(B_x) = \frac{A_0}{(\Omega_L \tau_s)^2 + 1}, \tag{3.15}$$

where A_0 is the peak Kerr rotation, $\Omega_L = g^* \mu_B B_x / \hbar$ is the Larmor precession frequency, and τ_s is the spin lifetime, as discussed in Chapter 1. A two-dimensional map of the spin accumulation as a function of position was made by scanning the beam across the sample, shown in Fig. 3.6(c). Interestingly, the authors found that the half-widths of the Lorentzian curves were narrower further away from the sample edges, which the authors interpreted as an increase in τ_s (see Fig. 3.7(b)). This apparent increase in τ_s, by as much as a factor of 5, was not well understood at the time.

Figure 3.7(a) shows a plot of the Kerr signal vs position for a line scan across the GaAs sample. By fitting the position dependence of $p_z(y)$ to the equation $p_z(x) = p_0 \sinh\left(\frac{x}{L_s}\right) / \cosh\left(\frac{w}{2L_s}\right)$, where p_0 and L_s were free parameters, the authors were able to determine the spin diffusion length and the spin polarization at the sample edge, which reached a maximum value of approximately 0.1%. This information, along with the value of τ_s determined from the Lorentzian fits to $A(B_x)$, allowed the authors to calculate the spin Hall conductivity, defined as $\sigma_{SH} = q_{x,z}/E_y$. It was found that $|e\sigma_{SH}| = 0.5\ \Omega^{-1}\text{m}^{-1}$ for the $\text{In}_{0.07}\text{Ga}_{0.93}\text{As}$ sample, which had a charge conductivity $\sigma_{xx} \approx 3000\ \Omega^{-1}\text{m}^{-1}$. From this, one can calculate $|\gamma| = |e\sigma_{SH}|/\sigma_{xx} \approx 2 \times 10^{-4}$. Following the experiment by Kato *et al.*, there have been a number of papers studying the SHE with similar optical techniques [72–75].

Unfortunately, it is extremely difficult to determine λ_{SO}^{eff} from γ. The total spin Hall angle γ includes contributions from both skew scattering and side-jump scattering. We will see in the following sections that these two terms are actually opposite in sign for attractive impurity potentials. Although $\gamma \propto \lambda_{SO}^{eff}$, it is impossible to determine the coefficient of proportionality without knowing both the skew and side-jump contributions. In the remainder of this chapter we will discuss an all-electrical measurement of the direct spin Hall effect, and we will

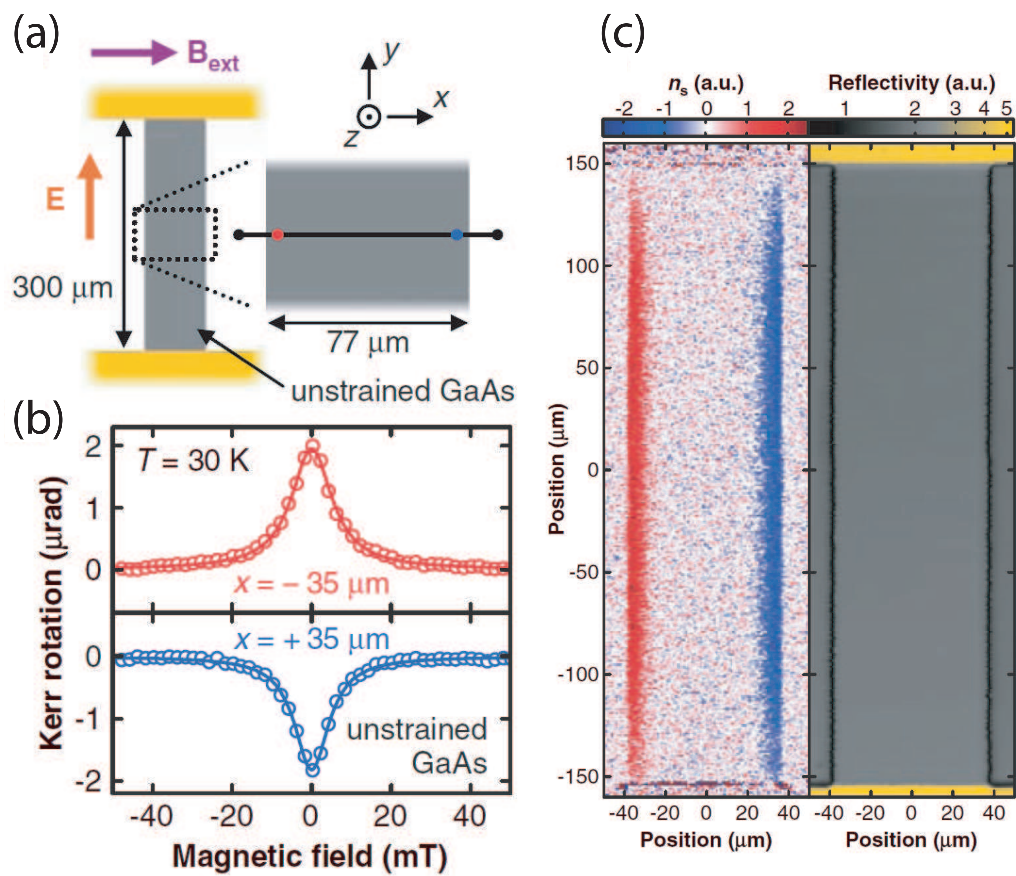

Figure 3.6: (a) Schematic of measurement geometry used by Kato *et al.* [71]. (b) Plot of Kerr rotation vs applied magnetic field shows dephasing of spin polarization via the Hanle effect. (c) Two-dimensional mapping of spin accumulation shows a decay of P_z away from the sample edges.

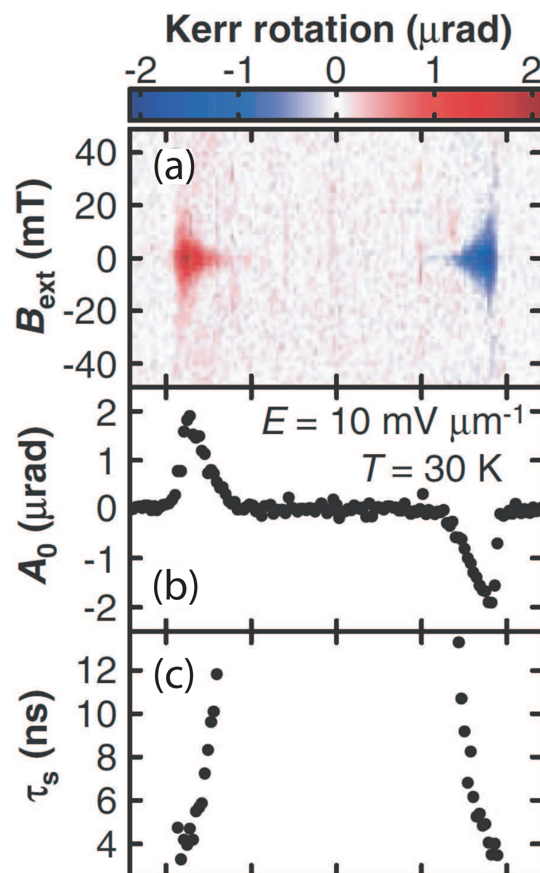

Figure 3.7: (a) Plot of $A(B_x)$ (see Eq. 3.15) vs position for the GaAs sample shows narrower half width away from the sample edges. (b) Plot of Kerr signal vs position for a line scan across the GaAs sample studied by Kato *et al.* [71]. (c) Plot of lifetime vs position as determined by fit $A(B_x)$ to a Lorentzian function.

show that it is possible to determine the skew and side-jump contributions to the spin Hall conductivity independently by analyzing the spin Hall conductivity as a function of the sample's charge conductivity.

3.4 All-Electrical Measurement of the Direct Spin Hall Effect

3.4.1 Device Design and Measurement Procedure

The use of ferromagnetic contacts to detect spin polarizations in GaAs electrically was discussed in Chapter 1. We will show that it is possible to implement those techniques to detect the spin Hall effect electrically by utilizing a suitable device geometry. A cartoon schematic of such a device is shown in Fig. 3.8. Four different $In_xGa_{1-x}As$ heterostructures were studied with In concentrations $x = 0.00, 0.03, 0.05$, and 0.06. Heterostructures were grown by molecular beam epitaxy on semi-insulating (001) GaAs substrates. First, a 500 nm GaAs buffer layer was grown, followed by a 2.5 μm thick n-doped channel, doped at 5×10^{16} cm^{-3} for all four samples. After the growth of the n-doped channel, the doping is ramped up from $n = 5 \times 10^{16}$ cm^{-3} to $n^+ = 5 \times 10^{18}$ cm^{-3} over a 15 nm thickness, then a 15 nm thick highly doped Schottky tunnel barrier is grown at $n^+ = 5 \times 10^{18}$ cm^{-3}. Next, a 5 nm thick epitaxial iron layer is grown, followed by a two-layer cap of aluminum and finally gold, to prevent sample oxidation. The In concentration was determined by X-ray diffraction measurements on a piece from each wafer.

These wafers are cleaved into pieces and processed into devices using the fabrication techniques discussed in Chapter 1 and detailed in appendix A. There are 4 separate devices patterned on each 5×5 mm^2 chip. Pairs of iron electrodes, each of which is nominally 4×50 μm^2, are patterned such that the long axis of the contact is the [110] direction ($\hat{x}$), which is along the ferromagnetic easy axis. The centers of the iron contacts are 2, 6, and 10 μm from the channel edges. Each

device has two sets of contacts with the same spacing from the edge, to ensure that the spin signal detected from the SHE is spatially uniform along the edges of the channel. A 30 μm wide conductive channel is defined by wet-etching the n-doped $In_xGa_{1-x}As$ layer. Current injection electrodes are also made of iron because of the challenges involved in fabricating efficient ferromagnetic spin injection contacts and ohmic contacts, which typically require annealing at high temperatures, on the same device. The current injection contacts are located > 250 μm ($\gg L_s$) away from the Hall detection contacts to ensure that the charge current is unpolarized.

To measure the spin Hall effect a current is applied down the length of the channel, and the voltage is measured between two iron contacts on opposite edges of the channel, as illustrated in Fig. 3.8(a). The spin Hall effect generates a spin accumulation at the sample edges that is oriented along [001] ($\hat{z}$). In order to measure a non-zero spin signal a magnetic field B_y is applied along $[1\bar{1}0]$, which precesses the out-of-plane spins into the ferromagnetic easy axis. This will produce a signal which is expected to be odd in B_y, showing an increase in voltage at small fields, extrema of opposite sign on opposite sides of zero, and a decay to zero signal at large fields due to dephasing. Because the magnetic field is applied along the ferromagnetic hard axis, $[1\bar{1}0]$, the magnetization of the iron will rotate as the applied field is increased. The hard axis saturation field is $B_{sat} \approx 1.5$ kOe. In order to ensure that the magnetization of the iron is in a well known state, the ferromagnetic contacts are first saturated in the $+\hat{x}$ direction by applying a large field (≈ 1 kOe). The field is then ramped back down to 0 Oe, and the sample is rotated so that the field can be applied along the $\hat{y}$ direction. The magnetic field is then swept from 0 to +2 kOe. The saturation procedure is then repeated, and the magnetic field is swept from 0 to −2 kOe. The entire measurement procedure is then repeated with the ferromagnetic contacts saturated in the $-\hat{x}$ direction, which will flip the sign of the spin-dependent part of the signal. Because the field sweeps must be taken in multiple segments, highly repeatable magnetostatics and milli-Kelvin level temperature control are crucial. Figure 3.9(a) shows a plot of

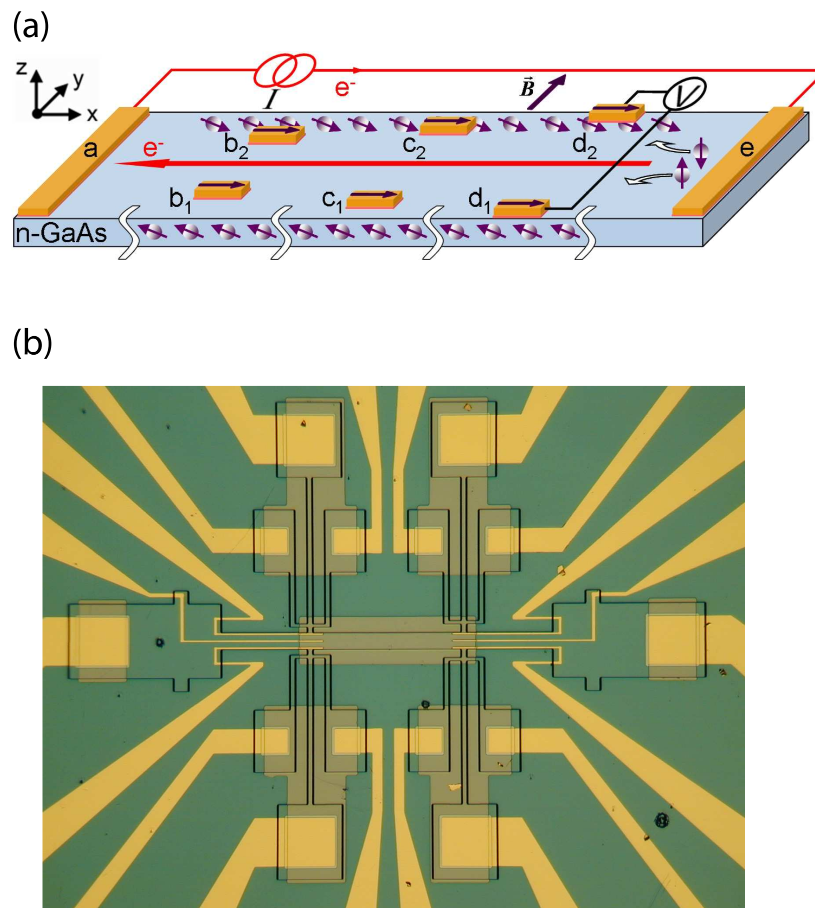

Figure 3.8: (a) Schematic diagram (not to scale) of the device layout and SHE measurement. Ferromagnetic spin detection contacts are placed at varying distances from the channel edge. In the actual experiment, contacts at different edge separations are on different devices on the same chip, and each device has two pairs of identical detection contacts to ensure that the detected spin Hall signal is spatially uniform along the edges of the channel. The current injection contacts are located $> 250\ \mu$m away from the Hall measurement contacts. (b) Photomicrograph of a finished device. Semiconductor Hall arms (not shown in the schematic) are used for measurements of ordinary charge transport. These are used to determine the carrier concentration from Hall measurements, as well as to isolate local Hall effects in measurements of the spin Hall effect.

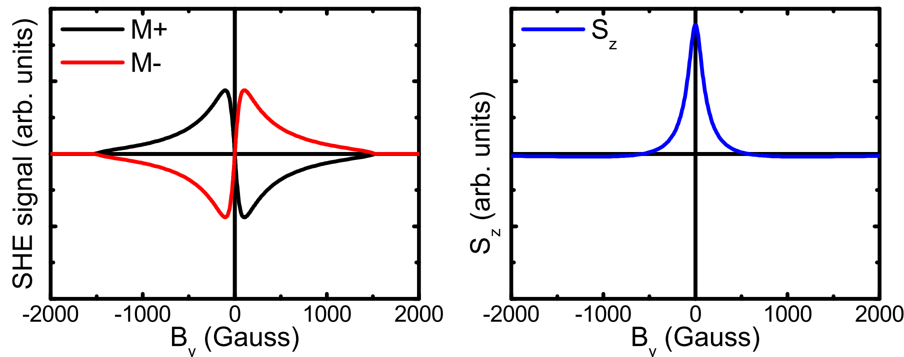

Figure 3.9: (a) Plot of expected signal as a function of applied magnetic field for a measurement of the spin Hall effect. (b) Plot of expected spin polarization as a function of applied magnetic field.

the expected signal vs applied field for both magnetization directions. Based on the optical measurements performed by Kato *et al.*, and the relationship between spin polarization and voltage discussed in Chapter 1 (Eq. 1.11), the expected voltage signal is on the order of 1 μV.

3.4.2 Background Subtraction and Fitting

In practice, the spin Hall signal is obscured by several spin-independent background effects, similar in some respects to the background effects in the non-local measurements discussed in Chapter 1. Raw data from a measurement of the spin Hall effect on the GaAs sample with $j_x = \pm 5.7\times10^3$ A/cm^2 is shown in Fig. 3.11(a) and (b). Unlike the non-local measurements, there is a large charge current flowing beneath the measurement contacts in the measurement of the spin Hall effect. This leads to a background voltage that is more than an order of magnitude larger than in the non-local measurements, meaning that all background effects from ordinary charge transport will be comparably larger. In this section we will show that it is possible to separate the spin Hall signal from the background signals based on the symmetries of the spin Hall effect.

There are three significant backgrounds: 1) the ordinary Hall effect and ordinary magnetoresistance, 2) local Hall effects resulting from the fringe fields of the ferromagnetic contacts, and 3) voltages due to a small fraction of the current (0.1%) shunting through the Hall measurement contacts. In the non-local measurements discussed earlier, only the first of these effects is present. The first background can be removed by taking the difference of the two field sweeps with the magnetizations oriented in the $+\hat{x}$ and $-\hat{x}$ directions, because the ordinary Hall effect and ordinary magnetoresistance do not depend on the magnetization direction of the contacts. In contrast, the spin-dependent part of the signal will change sign with the reversal of the magnetization.

The background voltages due to local Hall effects are quite large (of same order of magnitude as the spin Hall signal), due to the charge current flowing underneath the measurement contacts and the rotation of the magnetization due to the field applied along the hard axis. Unfortunately, the local Hall effects will also change sign when the magnetization is reversed, because they are due to fringe fields from the ferromagnetic contacts. Voltages from the local Hall effects are due predominantly to the x-component of the magnetization, and the corresponding fringe fields, which point in the $\pm\hat{z}$ direction, are *even* with respect to B_y (see Fig. 3.10). The spin Hall signal, on the other hand, is *odd* with respect to B_y. Local Hall effects can therefore be removed by retaining only the components of signal that are odd with respect to B_y. Measurements of the Hall voltage using the semiconductor Hall arms confirm that the local Hall effects are even with respect to B_y. Figure 3.11(c) and (d) show data taken on the GaAs sample with a channel current $j_x = \pm 5.7 \times 10^3$ A/cm^2 at $T = 30$ K after the removal of the first two backgrounds. As is expected from the spin Hall effect, the signal changes sign when the current direction is reversed.

There are, however, additional features near ± 1 kOe that do not reverse sign when the current is reversed, and hence cannot be due to a Hall effect. These features are due to a small fraction ($R_{SC}/R_{Schottky} \approx 0.001 = 0.1\%$) of the current shunting through the ferromagnetic contacts. This current has a component out of

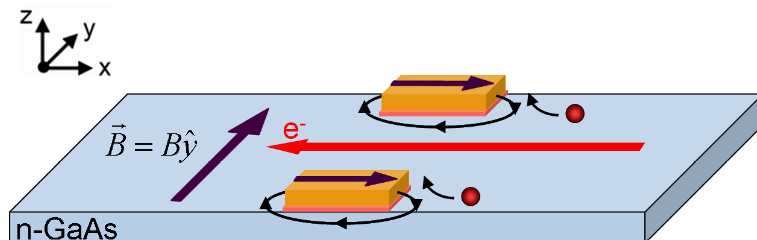

Figure 3.10: Deflection of charge current at the measurement electrodes occurs due fringe fields from the x-component of the magnetization. As the applied field is increased along the y-direction the magnetization rotates, changing the charge current path in the channel.

the plane when it tunnels through the Schottky barrier, which is highly rectifying. The Schottky barrier at the ferromagnet/semiconductor interface is known to exhibit tunneling anisotropic magnetoresistance (TAMR) that depends strongly on the angle between the magnetization and the [110] direction [12]. To check this, independent measurements of the interfacial voltage at the Schottky barrier were performed with current flowing directly into the ferromagnetic contact. Current densities of approximately 1 A/cm^2 produced a TAMR signal similar to that seen in the background of the spin Hall effect. This final background can be minimized by subtracting the measured Hall voltage for the two current directions. The resulting data, with all three background effects removed, are shown in Fig. 3.11(e). We find that the observed voltage maxima correspond to a spin polarization of $\approx 1.3\%$, using expression 1.11 to convert the measured voltage to a spin polarization. Determining the spin polarization at zero magnetic field requires a full fit to $P(B_y)$ in order to properly account for spin precession, diffusion, and relaxation.

Additionally, we also performed the same measurements with the ferromagnetic contacts on opposite edges of the channel initialized into the anti-parallel states $\uparrow\downarrow$ and $\downarrow\uparrow$. These data are shown as the solid line in Fig. 3.11(e). This curve shows zero Hall signal, demonstrating that the spin accumulation at opposite sample edges is opposite in sign.

Data taken at different contact separations on the $x = 0.00, 0.03, 0.05,$ and 0.06

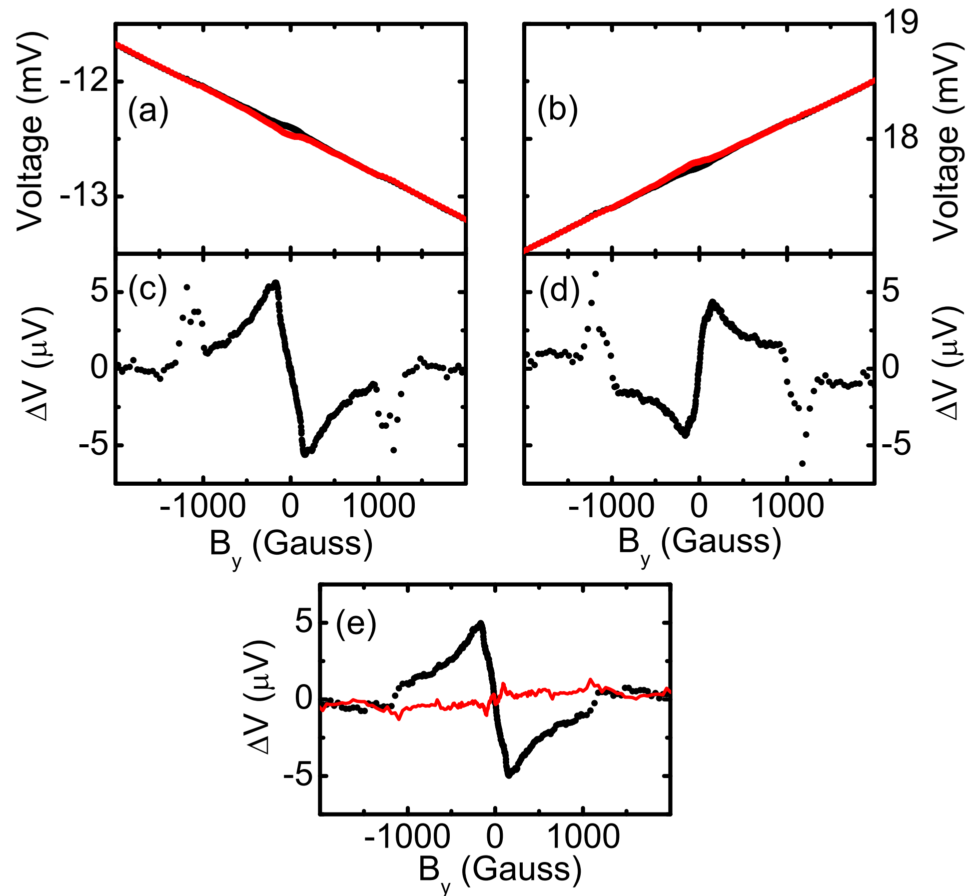

Figure 3.11: (a) Raw data for a measurement of the spin Hall effect with $j_x = +5.7 \times 10^3$ A/cm^2. (b) Raw data with $j_x = -5.7 \times 10^3$ A/cm^2. (c) Voltage vs field for $j_x = +5.7 \times 10^3$ A/cm^2 after removing ordinary and local Hall effects. (d) Voltage vs field for $j_x = -5.7 \times 10^3$ A/cm^2 after removing ordinary and local Hall effects. (e) Voltage vs field for $j_x = \pm 5.7 \times 10^3$ A/cm^2 after subtracting curves of opposite current direction with the two Hall contacts in the parallel state (points) and anti-parallel state (line). As expected, the curve with the Hall contacts in the anti-parallel state shows zero Hall signal.

samples with $j_x = \pm 2.9 \times 10^3$ A/cm^2 at $T = 30$ K are shown in Fig. 3.12. The voltage measured at contacts further in from the sample edges shows qualitatively similar features, with smaller signal sizes and narrower half-widths, similar to observations by Kato *et al.* [71]. Samples with higher indium concentrations show that the detected signal decays away more rapidly with increasing distance from the sample edges. For each device, we find that data from all contact separations can be fit to a single set of parameters using a slightly modified version of the drift diffusion model discussed in Chapter 1. In Sec. 3.3.1 we derived expression 3.14 for the spin accumulation as a function of position for the spin Hall effect. We note that in the limit of $w \gg L_s$ this reduces to:

$$p_z(y) = q_{y,z}\frac{\tau_s}{L_s}e^{-\frac{w}{2L_s}}\left[e^{\frac{y}{L_s}} - e^{-\frac{y}{L_s}}\right]. \tag{3.16}$$

If we now transform the coordinate system such that $y' = y + w/2$, so that the left edge of the sample corresponds to $y' = 0$, we find:

$$p_z(y) = p_0 e^{-\frac{y'}{L_s}}, \tag{3.17}$$

where $p_0 = q_{y,z}\frac{\tau_s}{L_s}$ is the polarization density at the sample edge. This expression is exactly equivalent to the expression for 1D spin diffusion away from a point source, where in this case the source can be taken as the sample edge. We therefore use the drift diffusion model discussed in Chapter 1 to model $P(B_y)$, taking into account the out-of-plane spin accumulation at zero applied field by taking the odd component with respect to precession, which is equivalent to S_x. We also take into account the rotation of the magnetization of the detection electrodes by multiplying the spin accumulation at a given field by $M_x/M_s = \sqrt{1 - M_y^2/M_s^2}$, where M_s is the saturation magnetization and $M_y = M_s \times B_y/B_{sat}$. The hard axis saturation field, B_{sat} is determined by independent magneto-resistance measurements. We further constrain the fits by calculating the diffusion constant D, from the channel conductivity σ_{xx} and the carrier concentration n, using a modified Einstein relation [30] to account for the effect of degenerate doping on the Fermi level in a semiconductor. The channel conductivity and carrier concentration are determined from independent resistance and Hall measurements,

respectively. The g-factor is fixed for each sample using the value calculated from the 8×8 Kane model, discussed in Sec. 2.3.2. This leaves P_0, the polarization at the sample edge in zero magnetic field, and τ_s, the spin lifetime, as the only free fitting parameters. The solid lines in Fig. 3.12(a-d) are fits to the data. The principal features of the data are captured by the fitting, including the decrease in signal with increasing distance from the edges and the location of the extrema. The narrower widths of the Hanle curves observed at increased distance from the edge can be interpreted as an increase in the time it takes for spins to diffuse from the sample edge to the measurement contacts. Despite the increased g-factor, the curves for the $In_xGa_{1-x}As$ samples are broader than for the GaAs sample. This reflects the shorter spin relaxation times in samples with higher In concentration, which will be discussed in more detail below. The decay of the spin polarization from the sample edges is shown in Fig. 3.12(e) for all four samples, normalized to P_0. The spin diffusion length decreases with increasing In concentration, from $L_s \approx 4$ μm in the GaAs sample to $L_s \approx 1$ μm in the $x = 0.06$ sample. We note that, for the GaAs sample with the longest spin diffusion length, $w \approx 7L_s$. Our assumption that $w \gg L_s$ is therefore found to be valid, since the spin accumulation from the opposite edge is suppressed exponentially.

Non-local Hanle measurements, as described in Chapter 1, were performed on companion devices processed on another chip from the same wafer for the $x = 0.00, 0.03, 0.05$ and 0.06 samples. These measurements also showed a trend of decreasing spin diffusion lengths for increasing x. Figure 3.14(a) shows the spin lifetimes extracted from both the non-local Hanle and the dSHE measurements on each heterostructure. The spin lifetime as determined from non-local Hanle measurements shows a decreasing trend with increasing In concentration, except for the $x = 0.06$ sample. The measured carrier concentration for the $x = 0.06$ sample was $n \approx 3 \times 10^{16}$ cm^{-3}, which is significantly lower than the others (all near $n = 5 \times 10^{16}$ cm^{-3}, see Fig. 3.16(b)). It is well known that the spin lifetime increases with smaller dopings in this range (see Eqs. 3.19 and 1.10) [26, 63, 76]. The lifetimes determined from the spin Hall fits also show a decreasing trend with

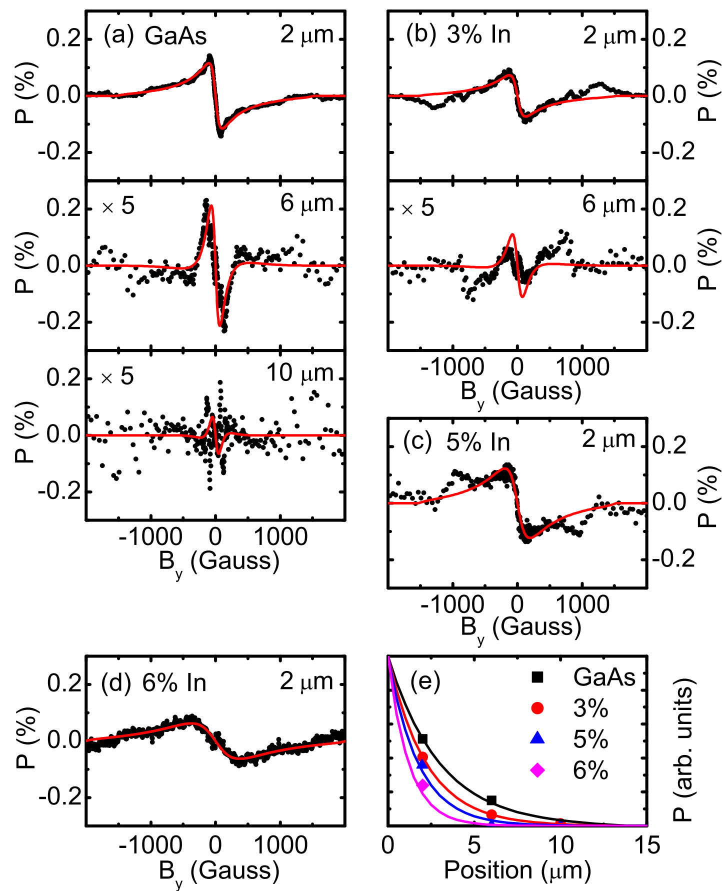

Figure 3.12: Spin Hall effect observed in $In_xGa_{1-x}As$ samples: (a) GaAs sample ($x = 0.00$) (b) $x = 0.03$ (c) $x = 0.05$ (d) $x = 0.06$ (e) Plot of $P(y)/P_0$ as determined from fit parameters for all 4 samples. All data were taken at $T = 30$ K, at a current bias of $j_x = \pm 2.9 \times 10^3$ A/cm^2.

increasing In concentration, but they are smaller than those determined from non-local Hanle measurements. We attribute this to the high current bias conditions of the spin Hall measurement, which makes the effective electron temperature higher than in a non-local experiment (see Sec. 3.4.4 for a detailed discussion) [63, 71, 76–78]. The spin relaxation time is related to the strength of spin-orbit coupling, so we can estimate the spin-orbit coupling strength from the value of τ_s determined from the fit.

The D'yakonov-Perel mechanism of spin relaxation is known to be the dominant contribution to spin relaxation in III-V semiconductors like GaAs and InAs, which lack inversion symmetry due to the fact that there are two distinct atoms in the Bravais lattice [76, 79]. Due to the spin-orbit Hamiltionian (Eq. 2.6), this leads to an intrinsic **k**-dependent magnetic field, $\mathbf{B}_{int}(\mathbf{k}) \propto \mathbf{k} \times \boldsymbol{\nabla} V$ that is odd with respect to **k**. This is referred to as the Dresselhaus spin-orbit interaction, and it will be discussed in further detail in Chapter 4. The strength of the Dresselhaus spin-orbit interaction is roughly βk_f^3, where β must be derived from the full 14×14 extended Kane model. For GaAs and InAs, $\beta \approx 27$ eVÅ^3.

To understand the influence of the intrinsic magnetic field on the spin lifetime, we recognize that electrons will precess about this field at an average frequency Ω_{av} that depends on the momentum distribution. Because the magnetic field $\mathbf{B}_{int}(\mathbf{k})$ is **k**-dependent, the direction of precession will change with each scattering event, on a timescale of τ_p. This is illustrated schematically in Fig. 3.13. If $\tau_p \Omega_{av} \lesssim 1$, then with each scattering event the electron will precess through an angle $\delta\phi \approx \Omega_{av}\tau_p$. Over a time t, the phase of the electron spin performs a random walk, traversing a total angle of $\phi(t) \approx \delta\phi\sqrt{t/\tau_p}$. Defining τ_s such that $\phi(\tau_s) = 1$, we find:

$$\frac{1}{\tau_s} = \Omega_{av}^2 \tau_p. \tag{3.18}$$

Pikus and Titkov calculated Ω_{av} in bulk III-V semiconductors and obtained the following expression for $1/\tau_s$ [63]:

$$\frac{1}{\tau_s} = \frac{32}{105} \gamma_3^{-1} \tau_p \frac{E_{\mathbf{k}}^3}{\hbar^2 E_g} \alpha^2, \tag{3.19}$$

where γ_3 is a dimensionless parameter that depends on the scattering mechanism and α is a dimensionless parameter related to the spin-orbit coupling strength. For the degenerate case, $E_{\mathbf{k}}$ is replaced by E_f. The parameter γ_3 is related to the efficiency with which a particular scattering mechanism randomizes $\mathbf{k}$. For impurity scattering, $\gamma_3 \approx 6$. For acoustic and polar optical phonon scattering, $\gamma_3 = 1$ and $\gamma_3 = 41/6$, respectively. Using the above expression we can calculate upper and lower bounds for α from the experimentally determined values of τ_s, τ_p, and E_f. The quantity α is related to the spin-orbit coupling strength by the following expression [49, 63]:

$$\lambda_{SO}^{eff} = \alpha \frac{\hbar^2}{8E_g} \frac{m_{cv}^*}{(m^*)^2} \frac{2-\xi}{\sqrt{1-\xi/3}}, \tag{3.20}$$

where m_{cv}^* is an effective mass describing the interband coupling between the bands in the 8×8 Kane model and the additional bands in the extended 14×14 Kane model [63]. As in Chapter 2, $\xi = \Delta_{SO}/(E_g + \Delta_{SO})$. The dependence of E_g, Δ_{SO}, and the effective mass on Indium concentration is well known [47, 48, 80]. From Ref. [63], the theoretical value of m_{cv}^* can be written as:

$$m_{cv}^* = \frac{1}{\beta} \frac{8\hbar^3}{3\sqrt{2m^* E_g}} \frac{\xi}{\sqrt{1-\xi/3}}. \tag{3.21}$$

For GaAs, we find $m_{cv}^* \approx 0.87 m_0$.

Using Eqs. 3.19, 3.20, and 3.21 we can calculate the spin-orbit coupling parameter from the spin lifetime τ_s. Figure 3.14(b) shows the resulting spin-orbit coupling parameter as a function of Indium concentration using spin lifetimes determined from both non-local Hanle measurements and spin Hall effect measurements on all four samples. Also plotted is the spin-orbit coupling parameter as predicted by the 8×8 Kane model. To estimate a lower bound for λ_{SO}^{eff} we take $\gamma_3 = 1$ for acoustic phonon scattering. The values of λ_{SO}^{eff} calculated are larger by a factor of $\gamma_3^{1/2} \approx 2.5$ if we assume instead that the dominant scattering mechanism is impurity scattering or polar optical phonon scattering.

For GaAs we find a lower bound for the experimentally determined value of λ_{SO}^{eff} is approximately a factor of 4 larger than the theoretically predicted value of

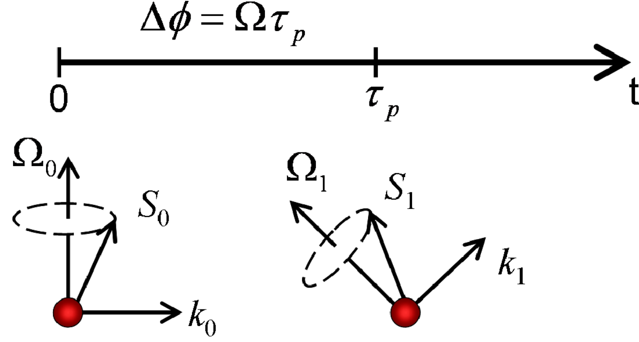

Figure 3.13: Cartoon illustrating D'yakonov-Perel spin relaxation. Electrons precess about a **k**-dependent magnetic field for a time τ_p between each scattering event. During each scattering event the direction of **k** is randomized, and thus so is $\Omega(\mathbf{k})$. Therefore, spin relaxation occurs after several momentum scattering events.

5.3 Å^2, as calculated from both the non-local and spin Hall lifetimes. We see that the 8×8 Kane model predicts relatively little change in the spin-orbit coupling parameter at low indium concentrations, due it its quadratic dependence on E_g and Δ_{SO}. However, we find that λ_{SO}^{eff} increases significantly with increasing In concentration, even for the small In concentrations studied here. The value of λ_{SO}^{eff} calculated from the spin Hall lifetimes is higher than that calculated from the non-local lifetimes, especially for the $x = 0.05$ and $x = 0.06$ samples. It may be that the large electric field applied in the spin Hall measurements influences spin relaxation in a way that is not captured by Eq. 3.19.

3.4.3 Determining the Spin Hall Conductivity

Here we will determine the spin Hall conductivity, defined as $\sigma_{SH} = q_{y,z}/E_x$ in Sec. 3.3.2, from the measured SHE signal. The first step is to determine the spin current $q_{y,z}$ from the measured polarization at the sample edges. Solving Eq. 3.17 for $q_{y,z}$ we find:

$$q_{y,z} = nP_0 \frac{L_s}{\tau_s}. \tag{3.22}$$

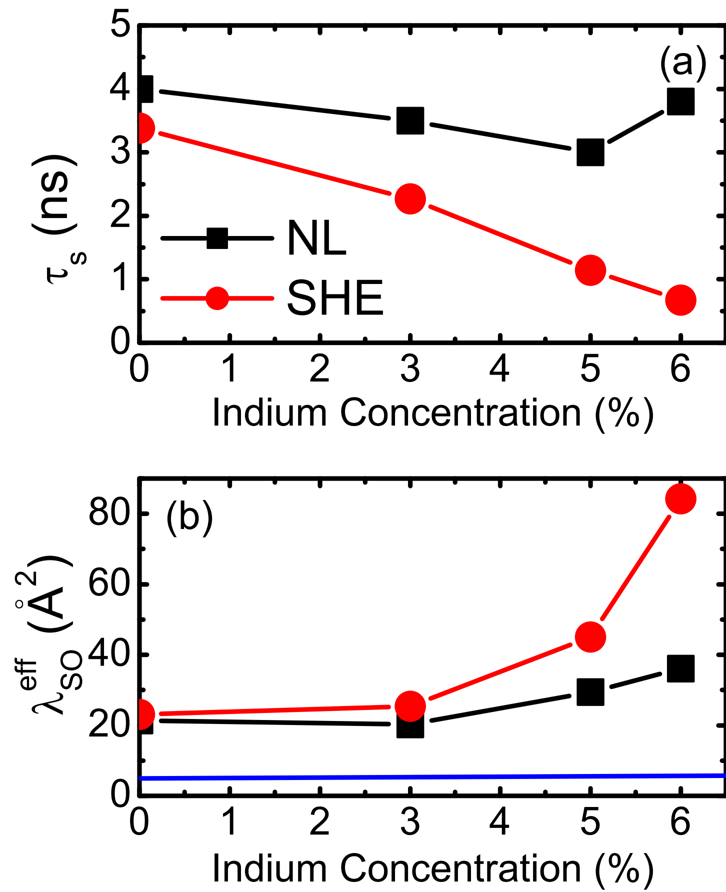

Figure 3.14: (a) Plot of spin lifetimes as determined from both non-local Hanle measurements at T = 60 K and spin Hall measurements at T = 30 K (see Fig. 3.12). (b) Plot of λ_{SO}^{eff} as determined from τ_s (points), assuming $\gamma_3 = 1$, in comparison to theoretically predicted change in λ_{SO}^{eff} from 8×8 Kane model (line).

Thus, the spin current can be calculated using the parameters P_0 and τ_s determined from the fit, and the values of D and n determined from transport measurements. For the GaAs sample, from the data shown in Fig. 3.12, we find $\sigma_{SH} = 3.0\ \Omega^{-1}\text{m}^{-1}$ which is of the same order as has been estimated from Kerr microscopy measurements performed by Kato *et al.* [71]. Using the measured charge conductivity of $\sigma_{xx} = 3600\ \Omega^{-1}\text{m}^{-1}$ we calculate $e\sigma_{SH}/\sigma_{xx} \approx 8 \times 10^{-4}$. To perform a more extensive analysis, we will compare our calculated value of the spin Hall conductivity to a theoretical calculation published by Engel *et al.* in 2005, which considered contributions from both skew and side-jump scattering [43].

Using a spin-dependent Boltzmann equation, Engel *et al.* calculated the dimensionless scattering angle γ_{SS} due to skew scattering to be:

$$\gamma_{SS} = \frac{1}{2} \frac{\int d\Omega I(\theta) S(\theta) \sin(\theta)}{\int d\Omega I(\theta)(1 - \cos(\theta))}, \tag{3.23}$$

where $S(\theta)$ is the Sherman function discussed in Sec. 2.2.2 and $I(\theta)$ is the spin-independent part of the scattering cross section. (Note that the factor of 1/2 in this expression that differs from the one in Ref. [43] is due the fact that the definition of γ in Eq. 3.6 and 3.7 is 1/2 that used by Engel *et al.*) Here they determined $I(\theta)$ using a screened coulomb potential, assuming Thomas-Fermi screening. For $S(\theta)$, they used the exact expression for an unscreened potential. They note that $S(\theta)$ is controlled by the small parameter $(Z\alpha^*)^2 = 4\lambda_{SO}^{eff}/(a_B^*)^2$, where $a_B^* = 103$ Å^2 is the effective Bohr radius (for Si donors) and $\alpha^* = e^2/\hbar c^*$ is a renormalized "fine structure constant" defined such that: $\lambda_{SO}^{GaAS} = \hbar^2/4(m^* c^*)^2 = 5.3$ Å^2. They find that angles near $\pi/2$ made the dominant contribution to the integral so that [40, 42, 43]:

$$\gamma_{SS} \approx S(\theta)/2 \approx \frac{2\lambda_{SO}^{eff}}{(a_B^*)^2}. \tag{3.24}$$

The contribution of skew scattering to the spin current is then:

$$\sigma_{SS} = \gamma_{SS} \frac{\sigma_{xx}}{e} = \frac{2\lambda_{SO}^{eff}}{(a_B^*)^2} \frac{\sigma_{xx}}{e}. \tag{3.25}$$

Engel *et al.* calculate the side-jump contribution by considering the "anomalous velocity" due to corrections to the velocity operator resulting from the spin-orbit interaction during scattering. This anomalous velocity can be written as [81]:

$$\delta\dot{\mathbf{r}} = \frac{\mathbf{i}}{\hbar}\left[H_{SO}, \mathbf{r}\right] = \lambda_{SO}^{eff}\left(\frac{\boldsymbol{\nabla} V}{\hbar} \times \boldsymbol{\sigma}\right). \tag{3.26}$$

To first order, $\boldsymbol{\nabla} V/\hbar = -\delta\dot{\mathbf{k}}$. Integrating with respect to time, we find: $\delta\mathbf{r} = \lambda_{SO}^{eff}(\boldsymbol{\sigma} \times \delta\mathbf{k})$. In addition to this term, there is another term that is identical in sign and magnitude which results from corrections to the position operator. Thus, the total side-jump $\delta\mathbf{r}$ is:

$$\delta\mathbf{r}_{tot} = 2\lambda_{SO}^{eff}(\boldsymbol{\sigma} \times \delta\mathbf{k}). \tag{3.27}$$

Using the fact that anomalous Hall charge current is $j_{AH}^{\uparrow,\downarrow} = -en^{\uparrow,\downarrow}\delta\mathbf{r}/\tau_p$ and the fact that the total momentum dissipated per scattering collision is on average $\hbar\delta\mathbf{k} = -e\mathbf{E}\tau_p$, we find the total side-jump contribution to the spin Hall conductivity to be:

$$\sigma_{SJ} = -\frac{j_{AH}^{\uparrow} - j_{AH}^{\downarrow}}{eE_x} = -2n\lambda_{SO}^{eff}\frac{e}{\hbar}. \tag{3.28}$$

By adding the contributions from skew and side-jump scattering, we arrive at an expression for the total spin Hall conductivity:

$$\sigma_{SH} = \sigma_{SS} + \sigma_{SJ} = \frac{2\lambda_{SO}^{eff}}{(a_B^*)^2}\frac{\sigma_{xx}}{e} - 2n\lambda_{SO}^{eff}\frac{e}{\hbar}. \tag{3.29}$$

A similar expression was derived by Tse and Das Sarma using diagramatic perturbation theory [82]. For the GaAs sample, at the value of j_x used for the data in Fig. 3.12, $\sigma_{xx} = 3600\ \Omega^{-1}\mathrm{m}^{-1}$. Using a value of $\lambda_{SO}^{GaAs} = 5.3$ Å^2 in Eq. 3.29 we calculate $e\sigma_{SS} = 3.6\ \Omega^{-1}\mathrm{m}^{-1}$ and $e\sigma_{SJ} = -1.2\ \Omega^{-1}\mathrm{m}^{-1}$, giving a theoretical estimate of the total spin Hall conductivity, $e\sigma_{SH}^{Thy} = 2.4\ \Omega^{-1}\mathrm{m}^{-1}$. This is a factor of 20% smaller than the experimentally determind value of $e\sigma_{SH}^{Exp} = 3.0\ \Omega^{-1}\mathrm{m}^{-1}$. We note that for the case of electrons scattering from positively charged impurities

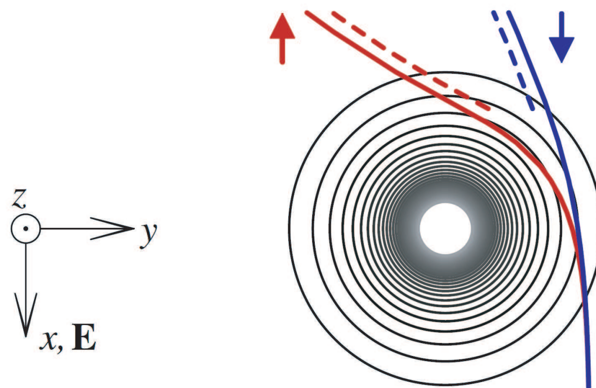

Figure 3.15: Cartoon of skew scattering (solid lines) and side-jump scattering (dashed lines). These two effects are opposite in sign and of similar magnitude in GaAs, making it difficult to determine λ_{SO}^{eff} from σ_{SH}. Figure is derived from Engel *et al.* [43].

(in this case, Si donors), the skew and side-jump contributions to the spin Hall conductivity are opposite in sign and approximately the same magnitude. Thus, making an accurate experimental estimate of λ_{SO}^{eff} requires the determination of both the skew and side-jump contributions to the total spin Hall conductivity.

3.4.4 Bias Dependence of the Spin Hall Conductivity

In Eq. 3.29 the skew term depends on channel conductivity, whereas the side-jump term is a constant. Therefore, by varying the channel conductivity, it is possible to determine both σ_{SS} and σ_{SJ}. Due to field assisted activation of donors, it is possible to tune the mobility, and hence σ_{xx} by approximately 25% by varying the applied electric field. Figure 3.16(a) shows a plot of the channel conductivity vs electric field. The change in σ_{xx} with electric field can be interpreted as an increase in the electron temperature. It has been shown that when $n \gtrsim 5 \times 10^{10}$ cm^{-3}, electron-electron collisions occur frequently enough that it is legitimate to consider an electron temperature T_e that may be out of equilibrium with the lattice temperature [77, 83].

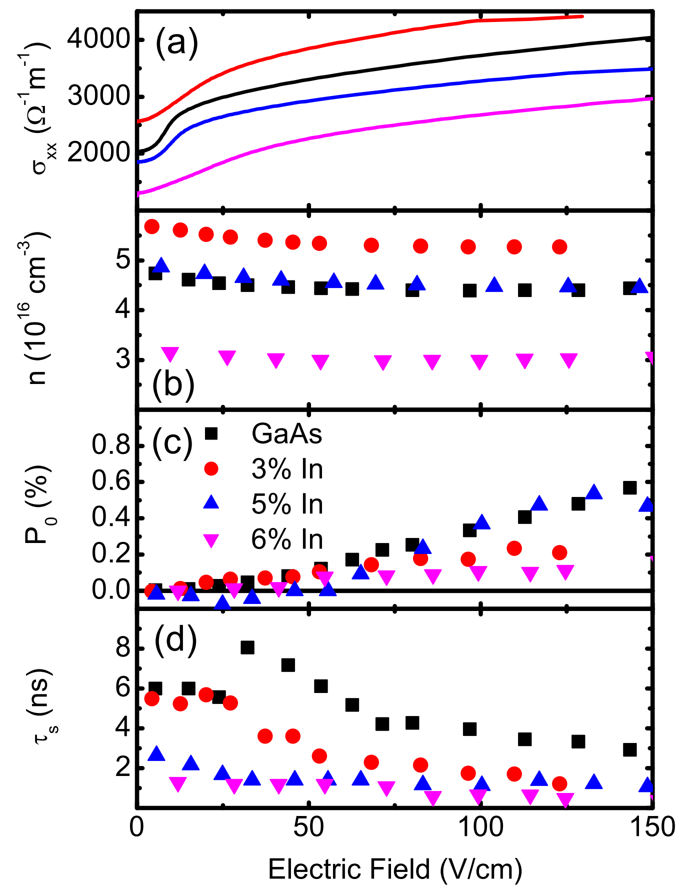

Figure 3.16: (a) Plot of channel conductivity vs electric field E_x. (b) Plot of carrier concentration vs electric field. (c) Plot of spin polarization P_0 at the sample edge vs electric field E_x as determined from fits. (d) Plot of spin lifetime τ_s vs electric field E_x as determined from fits. All data in this figure were taken at $T = 30$ K.

It is clear from Fig. 3.16(a) that there are three regimes. Here we will follow the arguments of Ref [77] to understand these effects. At relatively small electric fields ($E_x < 10$ V/cm), the conductivity increases approximately as (valid for $\delta \lesssim 1$):

$$\sigma_{xx} \approx ne\mu_0(1 + \delta z), \tag{3.30}$$

here $\delta = (T_e - T_L)/T_L$, where T_L is the lattice temperature. The dimensionless constant z relates the momentum scattering time to the electron energy by the relation $\tau_p \propto E^z$. The value of δ can be determined by equating the energy gained from the applied electric field to the average energy loss per collision:

$$e\mu E_x^2 = \left\langle \frac{dE}{dt} \right\rangle_c . \tag{3.31}$$

At low temperatures ($T \lesssim 30$ K) and low electric fields, Sladek [84] found that piezoelectric scattering was the dominant mechanism for energy loss, resulting in the following expression for δ:

$$\left\langle \frac{dE}{dt} \right\rangle_{PE} = \frac{3s^2}{\mu_L}\delta, \tag{3.32}$$

where $s \approx 5 \times 10^5$ cm/s is the speed of sound in GaAs and $\mu_L \approx 4 \times 10^5$ cm^2/Vs is the lattice mobility. Thus, for small electric fields, the conductivity increases quadratically with applied electric field.

Near $E_x \approx 10$ V/cm, there is a sharp rise in σ_{xx} that is associated with donor impact ionization [77, 78]. This occurs when the energy the electrons gain from the electric field is approximately the donor binding energy. Figure 3.17 shows a cartoon depicting a electron localized to a donor atom being ejected from its bound state. The critical field can be estimated by:

$$e\mu E_{x,critical}^2 = \frac{3s^2}{\mu_L}\frac{E_b}{T_L}, \tag{3.33}$$

where $E_b = 5.4$ meV is the donor binding energy. This expression results in $E_x \approx 10$ V/cm at $T = 10$ K. This results in a rapid increase in σ_{xx} as electrons localized on donors are activated into the conduction band, resulting in an increase

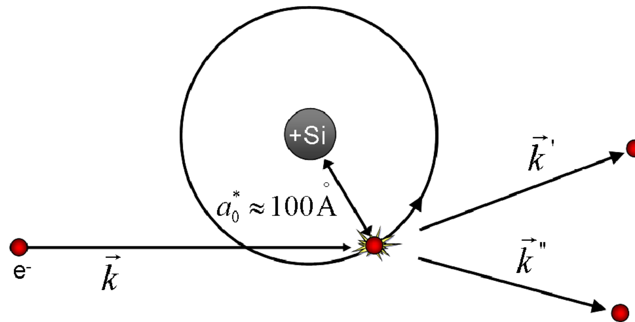

Figure 3.17: Cartoon Illustration of Donor Impact Ionization Event.

in both n and in μ. The carrier concentration determined from Hall measurements is shown in Fig. 3.16(b). Counter-intuitively, the carrier concentration as determined by Hall measurements appears to increase slightly as E_x decreases. This occurs because fewer electrons are participating in conduction band transport, which results in a larger Hall signal. It is difficult to interpret Hall voltages for electron transport in the hopping regime [85–87]. The smaller mobility for localized electrons may help explain the small spin Hall effect signals observed at electric fields near or below the donor impact ionization threshold, although it is important to note that noise on the order of $100\text{nV}/\sqrt{\text{Hz}}$ also limits the measurement resolution at these electric fields.

At electric fields above $E_x = 10$ V/cm, the carrier concentration is nearly constant. The mobility continues to increase with applied electric field, however Eq. 3.30 is no longer a valid approximation because δ is now significantly larger than 1. From transport data we estimate $T_e \approx 70$ K at the highest current bias applied in our measurements of the bias dependence of the spin Hall effect at $T =$ 30 K. Above $T_e \approx 30$ K, polar optical phonon scattering is the dominant energy loss mechanism. Optical phonon scattering is far more efficient at transferring energy to the lattice, and increases with increasing T_L and T_e [77]. This explains the smaller increase in mobility above $E_x = 10$ V/cm, and its eventual saturation at high bias. Most of the measurements of the spin Hall effect are in this regime, where the mobility is increasing slowly with applied electric field. We are limited

by the cooling power of the cryostat at electric fields above $\approx$ 150 V/cm due to Joule heating. We will show that the increase in mobility we attain ($\approx$ 25%) is sufficient to determine both the skew and side-jump contributions to the spin Hall conductivity.

Figure 3.18 shows a plot of the spin Hall conductivity vs the channel conductivity. We see clear evidence for both the skew and side-jump contributions to the total spin Hall conductivity. All four samples show a negative intercept, indicating the correct sign of the side-jump term. The slopes and intercepts are given in Table 3.1. The skewness parameter γ_{SS} obtained for GaAs is about 4 times larger than the prediction of $\gamma_{SS}^{GaAs,thy} = 1 \times 10^{-3}$. We can estimate λ_{SO}^{eff} from either the skew scattering term or the side-jump term. From the skew scattering term, for GaAs we find $\lambda_{SO}^{eff,SS} \approx 21$ Å^2, in good agreement with the lower bound that was estimated from the spin lifetime in Sec. 3.4.2. We can also compare our results with the expected ratio of σ_{SJ}/γ_{SS}, which is independent of the spin-orbit coupling parameter:

$$\frac{\sigma_{SJ}}{\gamma_{SS}} = -\frac{(a_B^*)^2 ne}{\hbar}. \tag{3.34}$$

We note that there are significant systematic errors in the conversion from a Hall voltage to a polarization, and then to a spin Hall conductance, due particularly to the assumption of a Pauli-like density of states in Eq. 1.11 and a fixed $\eta = 0.5$. These errors, however, do not impact the ratio σ_{SJ}/γ_{SS}, which is about a factor of 2.5 larger than the expected value for all four samples, as shown in Table 3.1. This discrepancy likely reflects the small parameter assumption made in calculating γ_{SS} in Eq. 3.23 and Eq. 3.24. The theoretically calculated value of γ_{SS} will be smaller if the integrals in Eq. 3.23 are evaluated without making a small parameter assumption [43]. This would make the predicted ratio σ_{SJ}/γ_{SS} larger. This would also increase the value of $\lambda_{SO}^{eff,SS}$ as calculated from the skew scattering term, bringing it closer to the value of $\lambda_{SO}^{eff,SJ}$ calculated from the side-jump term.

Figure 3.18(b) shows the values of λ_{SO}^{eff} as calculated from both the skew and side-jump contributions to the spin Hall conductivity. Also plotted are the values

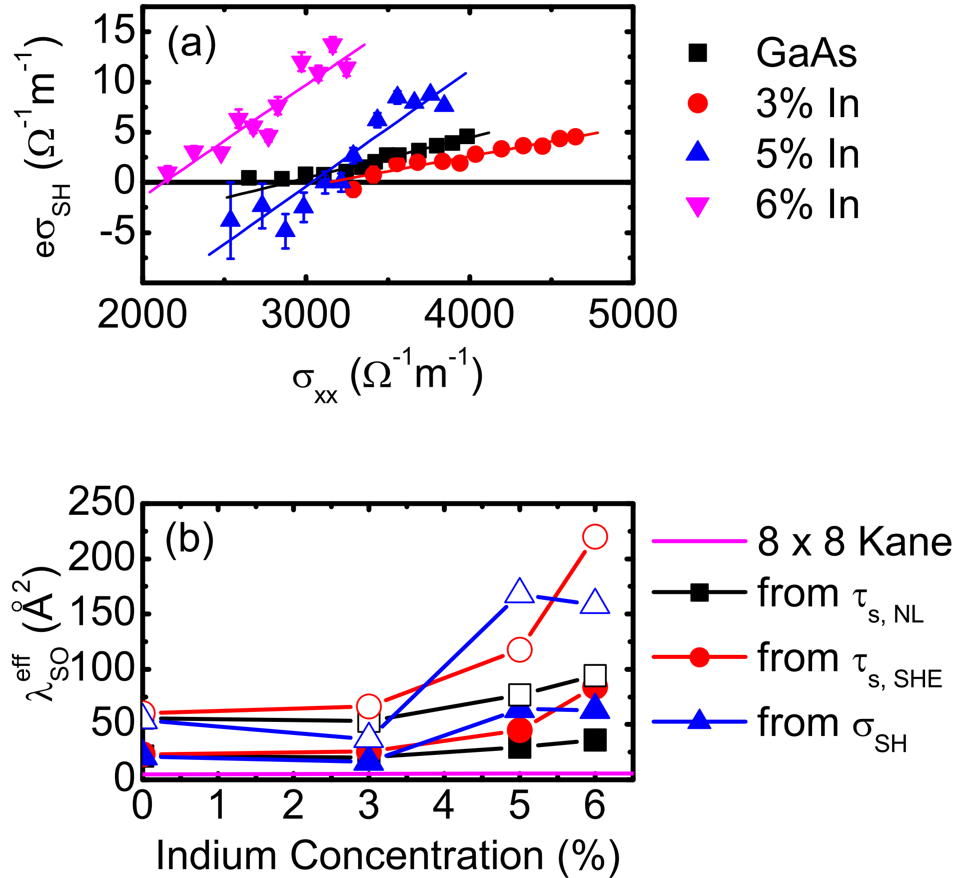

Figure 3.18: Plot of spin Hall conductivity vs channel conductivity for all four samples at T = 30 K. Solid lines are linear fits to the data. Skew and side-jump parameters extracted from the fits are shown in Table 3.1. (b) Plot of the spin-orbit coupling parameter vs. indium concentration as calculated from the skew and side-jump contributions to the spin Hall conductivity (solid and open triangles, respectively). Also plotted is the spin-orbit coupling parameter as determined from the spin lifetimes from fits to non-local and spin Hall Hanle data for $\gamma_3 = 1$ (solid squares and circles) and $\gamma_3 = 41/6$ (open squares and circles). The solid line shows the theoretically predicted value of λ_{SO}^{eff} from the 8×8 Kane model.

$\sigma_{SH} = \gamma_{SS}\sigma_{xx}/e + \sigma_{SJ}$	0% In	3% In	5% In	6% In
γ_{SS}	0.004	0.003	0.012	0.013
$e\sigma_{SJ}$ (Ω^{-1}m^{-1})	-12	-9	-35	-28
Meas. $e\sigma_{SJ}/\gamma_{SS}$ (10^3 Ω^{-1}m^{-1})	-3.0	-3.0	-2.9	-2.2
Pred. $e\sigma_{SJ}/\gamma_{SS}$ (10^3 Ω^{-1}m^{-1})	-1.1	-1.4	-1.2	-0.8
$\lambda_{SO}^{eff,SS}$ (Å^2)	21	16	64	63
$\lambda_{SO}^{eff,SJ}$ (Å^2)	54	37	168	158

Table 3.1: Fit parameters for σ_{SH} vs. σ_{xx}.

of λ_{SO}^{eff} calculated from the spin lifetimes, as discussed in Sec. 3.4.2, for both the cases of dominant acoustic scattering ($\gamma_3 \approx 1$) and polar optical phonon scattering ($\gamma_3 \approx 41/6$). Strikingly similar results are seen for the values of λ_{SO}^{eff} as calculated from either the spin Hall conductivity or the spin lifetime. Both methods give an approximate lower bound of λ_{SO}^{eff} for GaAs that is approximately 4 times the predicted value $\lambda_{SO}^{GaAs,thy} = 5.3$ Å^2.

Both methods also show significant evidence that λ_{SO}^{eff} is above this lower bound. It is clear that both impurity scattering ($\gamma_3 \approx 6$) and optical phonon scattering ($\gamma_3 \approx 41/6$) are important, so γ_3 in Eq. 3.19 is likely larger than 1, which will increase λ_{SO}^{eff} as calculated from τ_s by a factor of $\gamma_3^{1/2}$. Additionally, it is likely that the value of λ_{SO}^{eff} is being underestimated when calculated from the skew scattering contribution to σ_{SH}, due to the small parameter assumption made in Eq. 3.24.

Finally, we note that even the lower bound estimate for λ_{SO}^{eff} shows a larger increase with increasing In concentration than is predicted by the 8×8 Kane model. The 8×8 Kane model predicts approximately a 15% increase in λ_{SO}^{eff} between GaAs and 6% $In_xGa_{1-x}As$. Our results suggest that λ_{SO}^{eff} is more than 50% larger for the 6% sample than for the GaAs sample.

3.4.5 Temperature Dependence of the Spin Hall Conductivity

We studied the temperature dependence of the SHE over the range $T = 30-150$ K in all four samples. Figure 3.19 shows the experimentally determined spin Hall conductivity as a function of temperature (solid points). The solid lines show the predicted temperature dependence of σ_{SH} using the values of γ_{SS} and σ_{SJ} determined at $T = 30$ K from the fits in Fig. 3.18 and the measured values of $\sigma_{xx}(T)$ and $n(T)$. Reasonably good agreement is seen between the measured spin Hall conductivity and the predicted temperature dependence over the temperature range we studied. We find that σ_{SH} actually increases over the temperature range of $T = 30 - 100$ K due to the increase in electron mobility over this temperature range. These data suggest that γ_{SS} and σ_{SJ} are relatively temperature independent, and that they are insensitive to phonon scattering. Unfortunately, we are unable to experimentally determine the spin Hall conductivity at temperatures above ≈ 120 K, where effects due to phonon scattering would be most prominent. At temperatures above ≈ 120 K our measurement resolution is limited by the rapid decrease of τ_s with increasing temperature. This suppresses the spin Hall signal even if σ_{SH} is approximately constant.

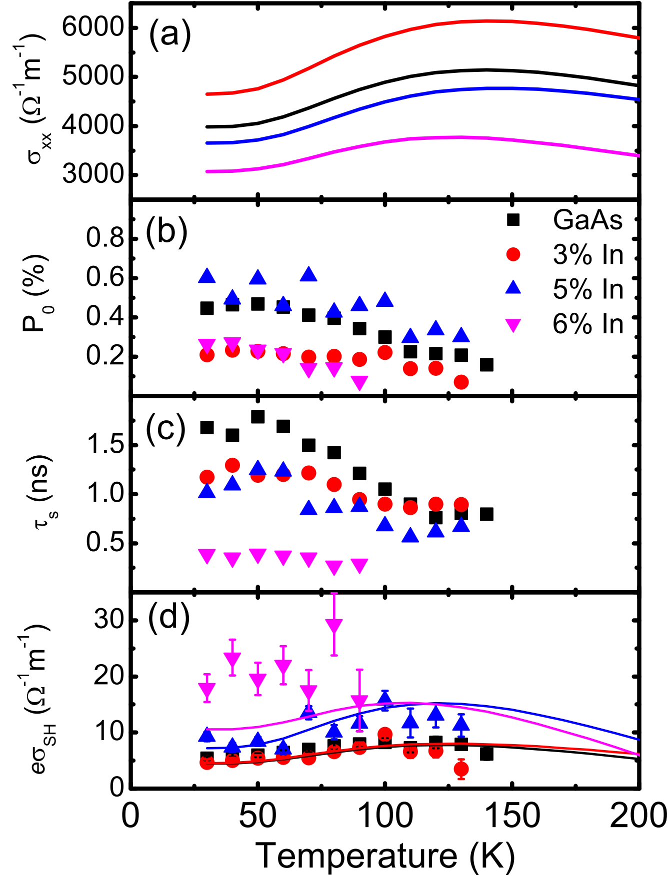

Figure 3.19: (a) Plot of σ_{xx} vs temperature shows an increase from $T = 30 - 120$ K due to the increase in electron mobility. The carrier concentration $n(T)$ is relatively constant over this temperature range, increasing by only $\approx 10\%$. (b) Plot of spin polarization vs temperature as determined from fits. (c) Plot of spin lifetime vs temperature as determined from fits. (d) Plot of spin Hall conductivity vs temperature. Solid points are experimentally determined values from fit parameters. Curves show the predicted temperature dependence of the spin Hall conductivity as estimated from the values of γ_{SS} and σ_{SJ} determined from the bias dependence measurements at $T = 30$ K and the measured values of $\sigma_{xx}(T)$ and $n(T)$. All data in this figure were taken with a current bias of $j_x = \pm 5.7 \times 10^3$ A/cm^2.

Chapter 4

Intrinsic Effects and Future Spintronic Devices

In Chapter 3 our analysis of the extrinsic spin Hall effect allowed us to quantitatively determine the spin orbit coupling parameter in $In_xGa_{1-x}As$ heterostructures. In this chapter we will see that the spin-orbit Hamiltonian given in Eq. 2.6 is associated not only with spin-dependent scattering from impurities, but also with a set of "intrinsic" effects which arise due to the inherent band structure in crystalline materials. Much of the recent interest in the spin Hall effect has been focused on these intrinsic effects [88–93], and several proposals for potential spintronic devices rely on the exploitation of these effects [2–4].

4.1 Intrinsic Spin-Orbit Effects

In the general form of the spin-orbit Hamiltonian in Eq. 2.6, we see that there must be a potential gradient $\boldsymbol{\nabla} V$ for spin-orbit effects to exist. This gradient need not come from an impurity potential; any potential gradient will lead to spin-orbit effects. Here we will discuss two different intrinsic effects arising due to inversion asymmetry in the crystal potential: the Dresselhaus effect, which arises due to bulk inversion asymmetry (BIA) and the Rashba effect, which arises due

to structural inversion asymmetry (SIA) [94, 95]. To consider these effects, it is helpful to rewrite the spin-orbit Hamiltonian in the following form:

$$H_{SO} = -\boldsymbol{\mu}_s \cdot \mathbf{B}_{int}(\mathbf{k}), \tag{4.1}$$

where $\mathbf{B}_{int}(\mathbf{k})$ can be thought of as a $\mathbf{k}$ dependent spin-orbit field that is intrinsic to the crystal structure. This effective field defines the ground energy spin state as a function of $\mathbf{k}$.

Bulk inversion asymmetry occurs in III-V zinc blende semiconductors like GaAs because there are two distinct atoms in the Bravais lattice (see Fig. 4.1(a)). This leads to an intrinsic $\mathbf{k}$-dependent magnetic field, $\mathbf{B}_{int}(\mathbf{k}) \propto \mathbf{k} \times \boldsymbol{\nabla} V$ that is odd with respect to $\mathbf{k}$. This is referred to as the Dresselhaus spin-orbit term. The derivation of the Dresselhaus term requires the inclusion of bands beyond those in the 8×8 Kane model. In bulk GaAs it is cubic in $\mathbf{k}$ to leading order, and can be written as [49, 96]:

$$H_D = \beta \left[k_x(k_y^2 - k_z^2)\sigma_x + k_y(k_z^2 - k_x^2)\sigma_y + k_z(k_x^2 - k_y^2)\sigma_z \right], \tag{4.2}$$

where $\beta = 27$ eVÅ^3 for GaAs as derived from the 14×14 extended Kane model. It is this term that gives rise to the $\mathbf{k}$ dependent magnetic field responsible for the D'yakonov-Perel spin relaxation mechanism discussed in Sec. 3.4.2 [79].

The Dresselhaus term is somewhat easier to visualize in the two-dimensional limit. If a two dimensional electron gas (2DEG) is formed by confining the electrons in the $\hat{z}$-direction in a quantum well of thickness d, then we have $< k_z >= 0$ and $< k_z^2 > \approx (\pi/d)^2$. Because $< k_z^2 >$ is large for small d, we can reduce the Dresselhaus term to:

$$H_{D,2D} \approx \beta_{2D}(k_x\sigma_x - k_y\sigma_y), \tag{4.3}$$

where $\beta_{2D} = -\beta(\pi/d)^2$. Figure 4.1(b) shows a plot of the effective magnetic field as a function of k_x and k_y due to the Dresselhaus term.

Structural inversion asymmetry can also give rise to an effective spin-orbit field, but it is not present in bulk III-V semiconductors. The effective spin-orbit field for

electrons confined in a 2DEG in the $\hat{z}$ direction by an asymmetric quantum well is illustrated in Fig. 4.1(d). For a constant gradient in the $\hat{z}$ direction $\partial V/\partial z = -eE_z$, from Eq. 2.6 we find [49, 96]:

$$H_R = \alpha_R(k_y\sigma_x - k_x\sigma_y), \tag{4.4}$$

where $\alpha_R = eE_z\lambda_{SO}^{eff}$. The effective magnetic field due to the Rashba term always points perpendicular to **k** and $\hat{z}$, so it will curl in the azimuthal direction in **k**-space as illustrated in Fig. 4.1(d). Unlike the Dresselhaus Hamiltonian, for which β is a fixed parameter which depends on the material, the magnitude of α in the Rashba Hamiltonian can be tuned by varying E_z, which can be achieved by either modifying the heterostructure doping profile or by applying a gate voltage across the quantum well.

Strain can also give rise to either bulk inversion asymmetry or structural inversion asymmetry. The details of the strain spin-orbit Hamiltonian depend on the components of the strain tensor, and it is discussed further in Ref. [92]. For the samples discussed in Chapter 3 of this thesis, there is a lattice mismatch between $In_xGa_{1-x}As$ and the GaAs substrate. However, at the In concentrations studied ($x \leq 0.06$) the strain is negligible ($< 0.5\%$). We also note that any strain in the $In_xGa_{1-x}As$ layer, which is 2.5 μm thick, is expected to relax over many atomic layers.

Our discussion of the extrinsic spin Hall effect in Chapter 2 and Chapter 3 relied on the force exerted on an electron when scattering due to the Zeeman-like interaction with the spin-orbit field from a charged impurity. Intrinsic spin orbit effects can also give rise to a spin Hall effect, although the mechanism is somewhat different as it does not rely on impurity scattering. To illustrate the intrinsic spin Hall effect, we will consider a 2DEG with a Rashba spin orbit field as pictured in Fig. 4.1(c) and (d). When an electric field is applied in the $\hat{x}$-direction, the electrons are accelerated at a rate $\hbar\dot{\mathbf{k}} = -eE_x$, shifting the center of the Fermi surface by $\delta k_x = -eE_xt/\hbar$ (see Fig. 4.2). This causes a shift in the spin-orbit field

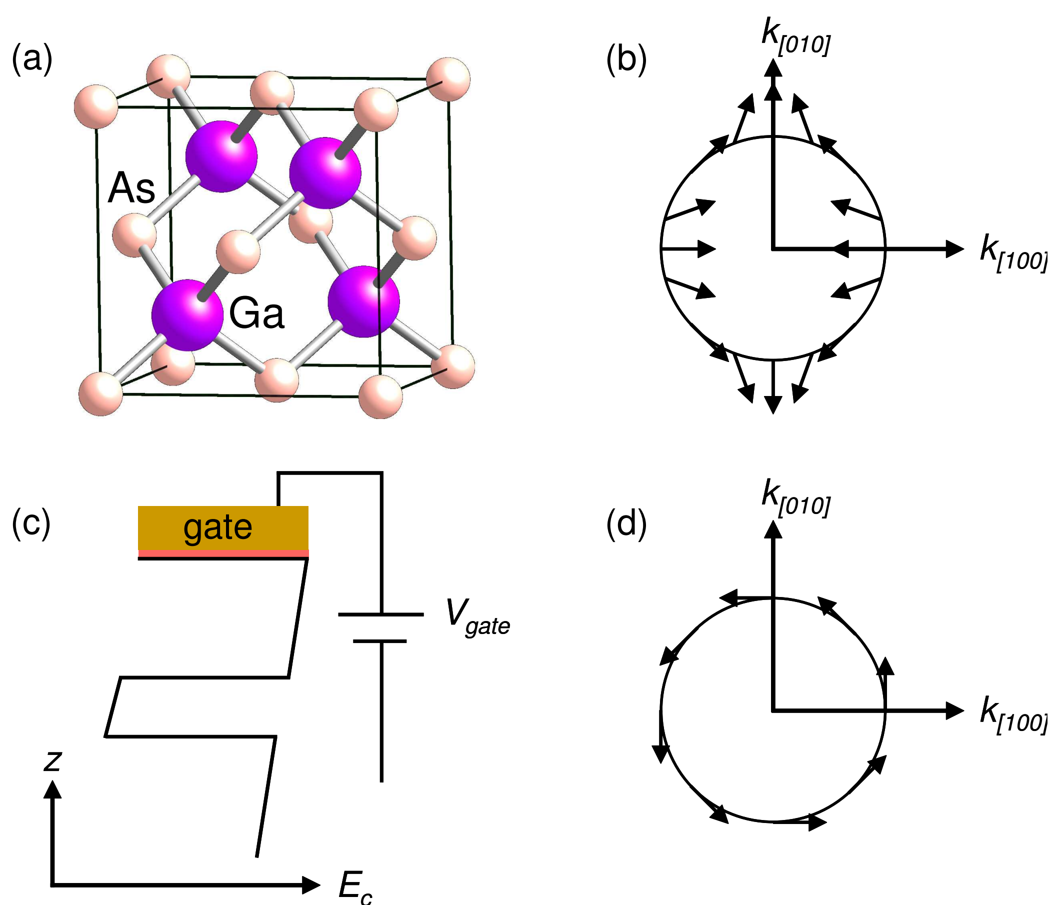

Figure 4.1: (a) Cartoon of the zinc blende structure shows bulk inversion asymmetry. (b) Plot showing direction of effective magnetic field in the xy plane due to the Dresselhaus interaction. (c) Cartoon of structural inversion asymmetry in a quantum well with a gradient in the $\hat{z}$ direction. (d) Plot of effective magnetic field in the xy plane due to the Rashba interaction.

[88]:

$$\mathbf{B}_{int}^{R} = \frac{2\alpha_R}{g^* \mu_B} \left[(\mathbf{k} + \delta k_x \hat{x}) \times \hat{z} \right] . \tag{4.5}$$

To lowest order the spins adiabatically rotate to follow the spin-orbit field, however there will be a non-adiabatic correction due to spins precessing about the spin-orbit field. Spins will precess in different directions depending upon the sign of k_y , thereby inducing a z-polarized spin current flowing in the y-direction, as shown in Fig. 4.2. It turns out that when impurity scattering is included to allow the charge carriers to reach a steady state, the deceleration due to scattering exactly cancels this effect for spin-orbit coupling which is linear in **k**, such as the first-order Rashba spin-orbit field we have considered here [89, 90]. However, terms which are cubic in **k**, such as the Dresselhaus term or higher order Rashba terms, survive even after deceleration due to impurity scattering is taken into account [96].

The contribution of the cubic Dresselhaus term to the spin Hall conductivity in bulk GaAs was estimated by Bernevig and Zhang to be $e\sigma_{SH}^{D,dirty} \approx 0.02\ \Omega^{-1}\text{m}^{-1}$ in the 'dirty' limit for samples with mobilities near 10^4 cm^2/Vs [91]. This is a negligible contribution to the total spin Hall conductivity determined in Sec. 3.4.3. We also estimate the possible contribution to the spin Hall conductivity from strain, using the arguments presented by Bernevig and Zhang in Ref. [91] and [92]. If we make the unrealistic assumption that the $\text{In}_x\text{Ga}_{1-x}\text{As}$ layer is fully strained, we estimate $e\sigma_{SH}^{strain,dirty} \approx 1\ \Omega^{-1}\text{m}^{-1}$ for the $x = 0.06$ sample. This is still significantly smaller than the contributions from skew and side-jump scattering discussed in Sec. 3.4.3.

Bernevig and Zhang also calculated the Dresselhaus contribution to the spin Hall conductivity in the clean limit, where $\beta k_F^3 \gg \hbar/\tau_p$ [91]. In this case, they estimated that $e\sigma_{SH}^{D,clean} \approx 200\ \Omega^{-1}\text{m}^{-1}$. This extremely large spin Hall conductivity could potentially be achieved in a high mobility 2DEG, where momentum scattering times longer than 10 ps have been observed. In addition to the large

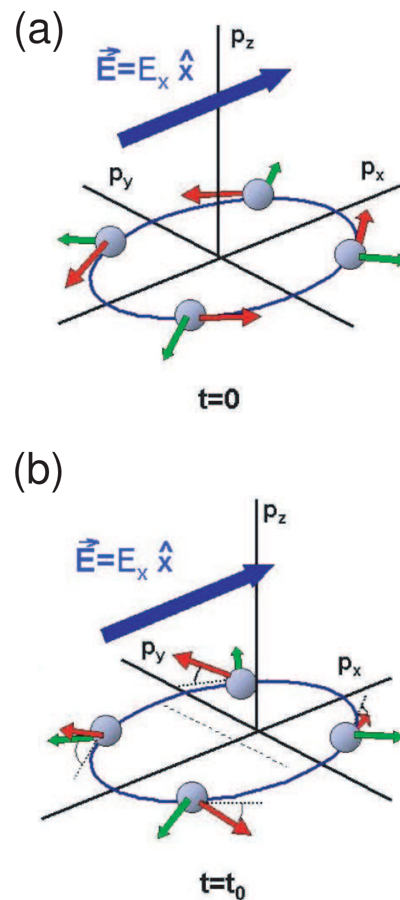

Figure 4.2: (a) Cartoon showing the Fermi surface for a 2DEG with a Rashba spin-orbit field. Momentum direction is illustrated with green arrows; the spin-orbit field is illustrated with red arrows. (b) Acceleration due to applied electric field changes the direction of B^R_{int}, causing spins to precess out of the plane in different directions depending on k_y. This figure is derived from Sinova *et al.* [88].

predicted spin Hall conductivity, these intrinsic spin-orbit fields could also be exploited to manipulate spins in other ways, which will be discussed in the next section.

4.2 Spin Field Effect Transistor Designs

One of the major limitations of current spin-based logic devices is the need to apply a magnetic field to change the device state, as is done in today's magnetic storage technologies. The spin-orbit interaction provides a means to manipulate the electron's spin state by applying electric fields rather than magnetic fields. One of the candidates for future spintronic devices is the spin field effect transistor or spin FET. Similar to a traditional MOSFET, in which a charge current is modulated by applying a voltage to a gate electrode, the operating principle of a spin FET is to modulate a spin current by applying a gate voltage. The operating frequency of a spin FET is limited by the spin precession time, which can be as short as ≈ 1 ps, potentially allowing operating frequencies in the hundreds of GHz. Furthermore, in a traditional MOSFET there exists a tradeoff between the barrier height in the off state and the gate voltage required to turn the device on, which limits the on/off power ratio. In a spin FET, the gate voltage affects only the spin precession frequency, and the on/off ratio is determined by the TMR ratio at the source and drain and the spin relaxation rate in the channel [4, 97]. Here we will discuss two different design proposals for a spin FET device. Both of these devices rely on the ability to manipulate the effective magnetic field through the Rashba spin-orbit interaction.

Datta and Das first proposed a spin FET device based on the modulation of the spin-orbit interaction in 1990 [2]. Figure 4.3 shows a schematic of their proposed device structure. The device consists of two ferromagnetic electrodes on top of a 2DEG channel. Both electrodes have their magnetization oriented in the $+\hat{x}$ direction. Between the two ferromagnetic electrodes is a gate electrode that is used to tune E_z. Electrons are injected from FM1 into the 2DEG, with their spin

oriented parallel to the magnetization, and travel toward the drain electrode FM2. As the electrons travel toward FM2 with drift momentum k_x, they experience an effective magnetic field:

$$B^R_{int} = \frac{2eE_z\lambda^{eff}_{SO}k_x}{g^*\mu_B}. \tag{4.6}$$

This field is perpendicular to the spin of the electrons, so they precess about it at the frequency $\Omega_L = g^*\mu_B B^R_{int}/\hbar$. When the electrons reach the drain electrode, they will have precessed through a total angle:

$$\theta = \Omega_L t = \frac{g^*\mu_B B^R_{int}}{\hbar}\frac{m^*L}{\hbar k_x}, \tag{4.7}$$

where L is the distance between FM1 and FM2. In the above expression, it is clear that changing the applied gate voltage to tune E_x will modulate the angle of the spins arriving at the detector electrode. It is also interesting that the total angle precessed does not depend on k_x, due to the cancellation between the Rashba spin-orbit field and the transit time.

The preceding analysis makes two significant assumptions. First, it assumes that the quantum well thickness d is small enough such that mixing between different bound states can be neglected, which requires $\hbar^2/2m^*d^2 \gg \alpha_R k_x$. Secondly, it assumes that electrons travel ballistically between FM1 and FM2, and that the electrons have $k_y = 0$. In high mobility 2DEGs, with $\mu \approx 10^6$ cm^2/Vs, mean free paths longer than 1 μm have been observed at low temperature ($\approx$ 10 K) [98, 99]. An order of magnitude calculation shows that an electric field of $\approx 10^5$ V/cm is required in order to achieve a π rotation in a GaAs 2DEG, assuming $\lambda^{GaAs}_{SO} \approx 5.3$ Å^2. Assuming a gate electrode is within 100 nm of the 2DEG, this corresponds to a gate voltage of $V_{gate} \approx 5$ V, which is achievable. Our results from Chapter 3 suggest that λ^{GaAs}_{SO} is approximately a factor of 4 larger than 5.3 Å^2, which would reduce the required gate voltage. The gate voltage is further reduced by approximately an order of magnitude if an InAs quantum well is used instead. Optical measurements of gated control of spin precession were published by Studer *et al* in a GaAs/AlGaAs quantum well [100]. Results suggesting spin injection and gated

control of spin precession in an InAs 2DEG were recently published by Koo *et al.* [101], although many unresolved questions remain. Further studies should be performed on similar structures to confirm their results and to better quantify the spin-orbit coupling parameter and spin relaxation time.

A different design for a spin FET, termed a resonant spin lifetime transistor (RSLT), was proposed by Cartoixà *et al.* in 2003 [3, 102]. As the name suggests, the proposed device operates by controlling the spin lifetime in the 2DEG channel. The geometry is similar to the Datta-Das proposal, however the device is designed to operate in the diffusive regime. This significantly eases the processing and operating temperature constraints of the Datta-Das transistor. As was discussed in Sec. 3.4.2 and Sec. 4.1, the Dresselhaus spin-orbit term is the dominant factor in determining spin lifetimes in III-V semiconductors with no Rashba spin-orbit interaction. In a 2DEG, however, both the Rashba and Dresselhaus terms may be present. This is an advantage rather than a disadvantage. The total spin-orbit Hamiltonian in an (001) quantum well can be written as:

$$H_{SO} = H_R + H_{D,2D} = \sigma_x(\alpha_R k_y + \beta_{2D} k_x) - \sigma_y(\alpha_R k_x + \beta_{2D} k_y). \tag{4.8}$$

If we rotate our coordinate system by 45 degrees, along the [110] and [$\bar{1}$10] directions rather than [100] and [010], we find:

$$H_{SO} = \sigma_{110}(\alpha_R - \beta_{2D})k_{\bar{1}10} - \sigma_{\bar{1}10}(\alpha_R + \beta_{2D})k_{110}, \tag{4.9}$$

where $\sigma_{110} = (\sigma_x + \sigma_y)/\sqrt{2}$, $\sigma_{\bar{1}10} = (-\sigma_x + \sigma_y)/\sqrt{2}$, and $k_{110} = (k_x + k_y)/\sqrt{2}$, $k_{\bar{1}10} = (-k_x + k_y)/\sqrt{2}$. Cartoixà *et al.* proposed that by tuning the gate voltage such that $\alpha_R = \beta_{2D}$, spin relaxation will be greatly suppressed for spins pointed parallel to the [$\bar{1}$10]. It is clear from inspection of Eq. 4.9 that if $\alpha_R = \beta_{2D}$, then the effective spin-orbit field is parallel to the [$\bar{1}$10] direction regardless of the value of **k** (see Fig. 4.4(b) and (d)). Therefore, spins parallel to [$\bar{1}$10] will not experience D'yakonov-Perel spin relaxation because they will always be in an energy eigenstate of the spin-orbit Hamiltonian. Averkiev and Golub calculated that the D'yakonov-Perel spin relaxation rate is proportional to $(\alpha - \beta_{2D})^2$ [103,

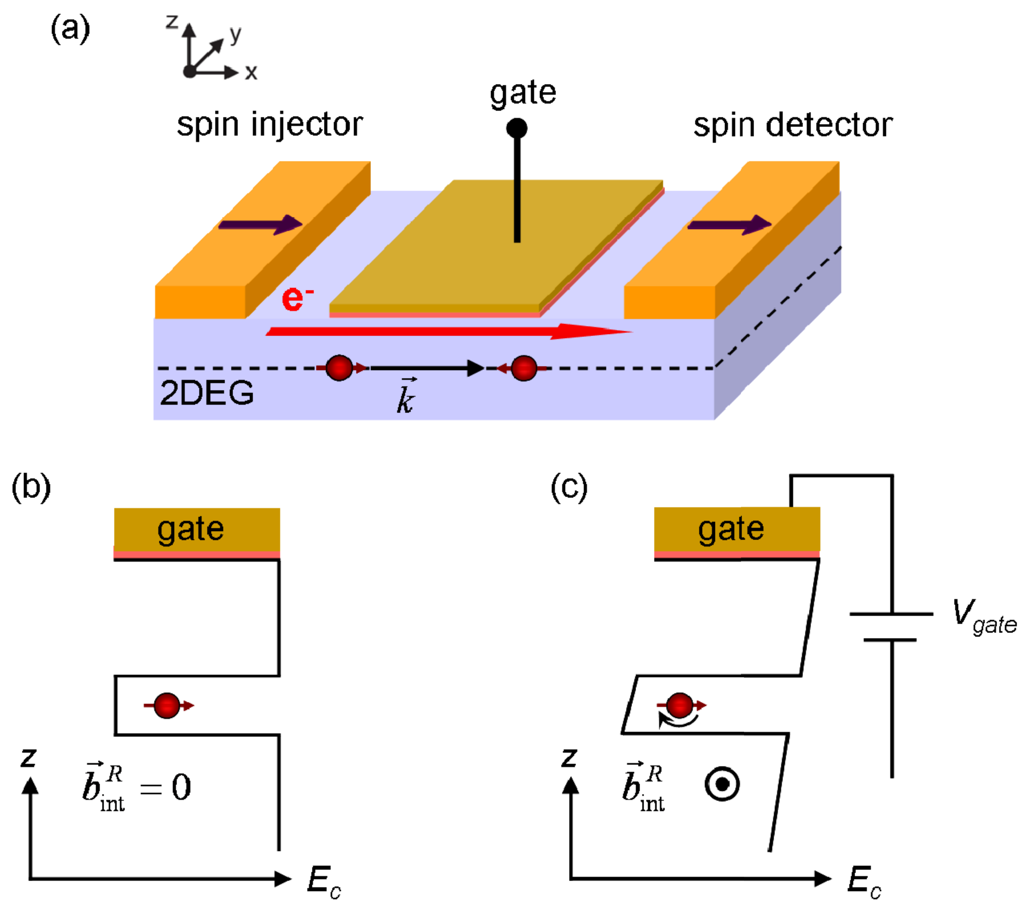

Figure 4.3: (a) Cartoon schematic of the spin FET proposed by Datta and Das [2]. (b) If zero gate voltage is applied, $E_z \approx 0$, and thus $B^R_{int} \approx 0$. Therefore spins remain oriented in the same direction as they travel from injector to detector. (c) If a gate voltage is applied across the 2DEG, spins precess around the induced spin-orbit field $B^R_{int}(E_z)$. If the gate voltage is tuned appropriately, spins can be made to precess 180 degrees by the time they reach the detector.

104]; thus, the spin lifetime can be increased by many orders of magnitude for α_R sufficiently close to β. The spin lifetime, of course, will still be finite, due to higher order terms in the spin-orbit Hamiltonian which we have neglected, or other mechanisms of spin relaxation that we have not considered, such as Elliott-Yafet mechanism, hyperfine coupling, or electron-hole exchange interactions [63, 76, 105–108].

The proposed operation of the resonant spin lifetime transistor is as follows (see Fig. 4.4(a) and (c)): Spin polarized electrons are injected into the 2DEG by FM1, and they diffuse toward FM2. If the gate voltage is tuned such that $\alpha_R = \beta_{2D}$, the spins will retain their polarization state when they arrive at FM2. If, however, the gate voltage is tuned such that $\alpha_R \neq \beta_{2D}$, the spin information will be lost due to spin relaxation as the spins diffuse from FM1 to FM2. For this reason, in order to function properly, the RLST *must* operate in the diffusive regime. This makes the RSLT much better suited for potential room temperature operation. Furthermore, it has been suggested that if α_R is kept sufficiently close to β_{2D} it may be possible to demonstrate control of spin precession in the diffusive regime rather than the ballistic regime due to the suppression of D'yakonov-Perel spin relaxation [109].

There have been some optical measurements showing enhanced spin lifetimes due to the suppression of D'yakonov-Perel spin relaxation in quantum wells along different crystal axes [110, 111] and in asymmetrically doped quantum wells where $\alpha_R \approx \beta_{2D}$ [112–114]. Additionally, D'yakonov-Perel spin relaxation has been shown to be suppressed in 2DEG nanowires by measurements of weak anti-localization effects [115–117] and optical pump-probe measurements [118]. This suppression occurs, even when the electrical transport is still two-dimensional, when the wire width is smaller than the spin-orbit length $L_{SO} = \hbar^2/2\beta_{2D}m^* \approx 1\ \mu$m. The spin-orbit length is the approximate distance traveled before a full precession. The suppression of the spin lifetime occurs because the phase shift the spin acquires from precession about $\mathbf{B}_{int}(\mathbf{k})$ is reduced for components of $\mathbf{k}$ perpendicular to the wire axis [119]. Recent measurements of weak anti-localization

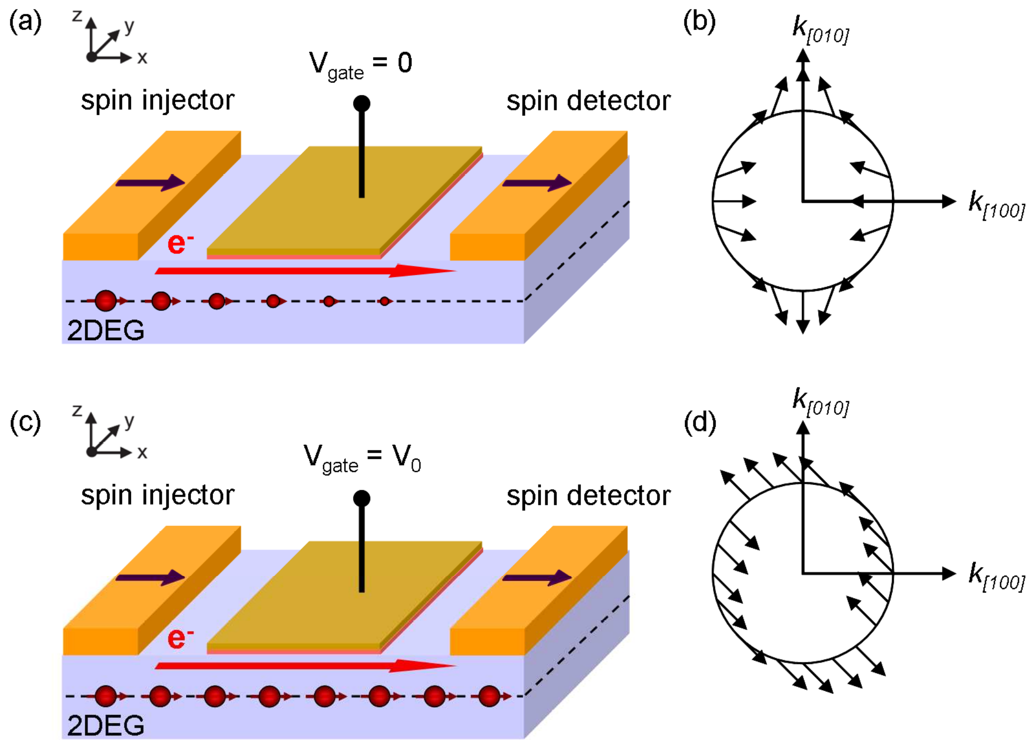

Figure 4.4: (a) Cartoon schematic of the resonant spin lifetime transistor proposed by Cartoixà *et al.* [3]. When $E_z = 0$ spins relax in the channel before arriving at the detector. (b) Plot showing the direction of the effective magnetic field due to the Dresselhaus interaction when $E_z = 0$. (c) When V_{gate} is tuned such that $\alpha_R = \beta_{2D}$, spin relaxation is suppressed and spins can travel from the injector to the detector without relaxing. (d) Plot showing the direction of the effective magnetic field when $\alpha_R = \beta_{2D}$. Because the effective magnetic field is parallel to the $[\bar{1}10]$ direction for all $\mathbf{k}$, spin relaxation is suppressed.

in gated $In_{0.53}Ga_{0.47}As$ nanowires have shown suppression of spin relaxation due to both dimensional confinement and the tuning of $\alpha_R \approx \beta_{2D}$ [120].

4.3 A Path to Future Experiments

Many challenges must still be overcome to demonstrate a fully functional spin FET. Here we outline a potential path for future experiments to move towards this goal. The first challenge is to demonstrate electrical spin injection and detection in a high mobility 2DEG. The approach used for injecting spin polarized electrons into bulk GaAs, by tunneling through a Schottky barrier at the Fe/GaAs interface, needs to be modified for spin injection into a high mobility 2DEG heterostructure. Designing a high mobility 2DEG requires remote doping in a heterostructure, such that the donor atoms can be kept sufficiently far away from the 2DEG transport layer to minimize coulomb scattering. In the Fe/GaAs samples studied up to this point, the high doping used to form the Schottky barrier near the Fe/GaAs interface creates a degenerately doped low mobility 2DEG in the ≈ 15 nm $n^+ \rightarrow n$ transition region (see Sec. 1.4 and Sec. 1.6).

It is possible to create a tunnel barrier of appropriate height and thickness for efficient spin injection by designing a heterostructure of lattice matched semiconductor alloys with different band gaps. For example, from Table 2.1 we see that AlAs has a lattice constant very similar to GaAs ($< 1\%$ lattice mismatch), but a much larger band gap. A barrier of height $\phi_B \approx 1$ eV and width $d \approx 10$ nm can be engineered using a $Al_{0.3}Ga_{0.7}As$/GaAs heterostructure. It is proposed to approach the problem of spin injection into a 2DEG in two steps. First, one can demonstrate efficient spin injection through an engineered heterostructure barrier into bulk n-GaAs. This allows the tunnel barrier parameters to be optimized in a spin transport environment that is already well understood. Second, the transport layer can be changed from bulk n-GaAs to a modulation doped $Al_xGa_{1-x}As/GaAs/Al_xGa_{1-x}As$ 2DEG. The charge transport properties of the

2DEG, such as the carrier concentration and mobility, can be characterized using traditional electron transport measurements. From these measurements one can make a reasonable estimate of the spin lifetime and spin diffusion length in the 2DEG, as described in Sec. 3.4.2 and Sec. 4.1. Figure 4.5 shows the calculated band structure of three different devices: (a) the Fe/GaAs structure discussed in Sec. 1.4, (b) an Fe/$Al_{0.3}Ga_{0.7}As$/n-GaAs heterostructure, and (c) an Fe/$Al_{0.3}Ga_{0.7}As$/GaAs/$Al_{0.3}Ga_{0.7}As$ modulation doped 2DEG [121]. The same approach can be used to engineer barriers in materials with larger spin-orbit coupling. For example, $In_{0.52}Al_{0.48}As$ could be used to obtain a barrier of height $\phi_B \approx 1$ eV for tunneling into $In_{0.53}Ga_{0.47}As$. $In_{0.52}Al_{0.48}As$ and $In_{0.53}Ga_{0.47}As$ are both lattice matched to InP.

The spin lifetime is expected to be substantially shorter in the GaAs 2DEG than in bulk GaAs, because for D'yakonov-Perel spin relaxation $\tau_s \propto 1/\tau_p$. Qi Hu's first attempts to grow a remotely doped 2DEG yielded a mobility near 10^5 cm^2/Vs, approximately an order of magnitude larger than in bulk GaAs. This corresponds to a momentum scattering time $\tau_p \approx 1$ ps. We therefore find a zeroth order estimate of the spin lifetime to be $\tau_s^{QW} \approx 100$ ps. The spin diffusion length $L_s = \sqrt{D\tau_s}$, on the other hand, should remain roughly constant because $D \propto \mu$. These estimates suggest that non-local measurements may still be feasible in a high mobility AlGaAs/GaAs/AlGaAs 2DEG at micron length scales. Three terminal Hanle measurements, as discussed in Sec. 1.8 may also be a useful tool for probing the spin lifetime in a 2DEG system. The anticipated half-width of a Hanle curve will be substantially larger due to the shorter spin lifetime and transit time in the 2DEG. We estimate $B_{1/2} \sim 1$ kG, which is still smaller than the 2.1 T out-of-plane saturation field of the Fe contacts. However, it is clear that as the mobility increases, the assumptions made in our estimates of τ_s and L_s are no longer valid as τ_p approaches τ_s. We therefore take τ_p and L_p to be lower bounds for τ_s and L_s in the high mobility limit. We note that there is currently not a well established theoretical interpretation of a non-local voltage measurement in the ballistic regime.

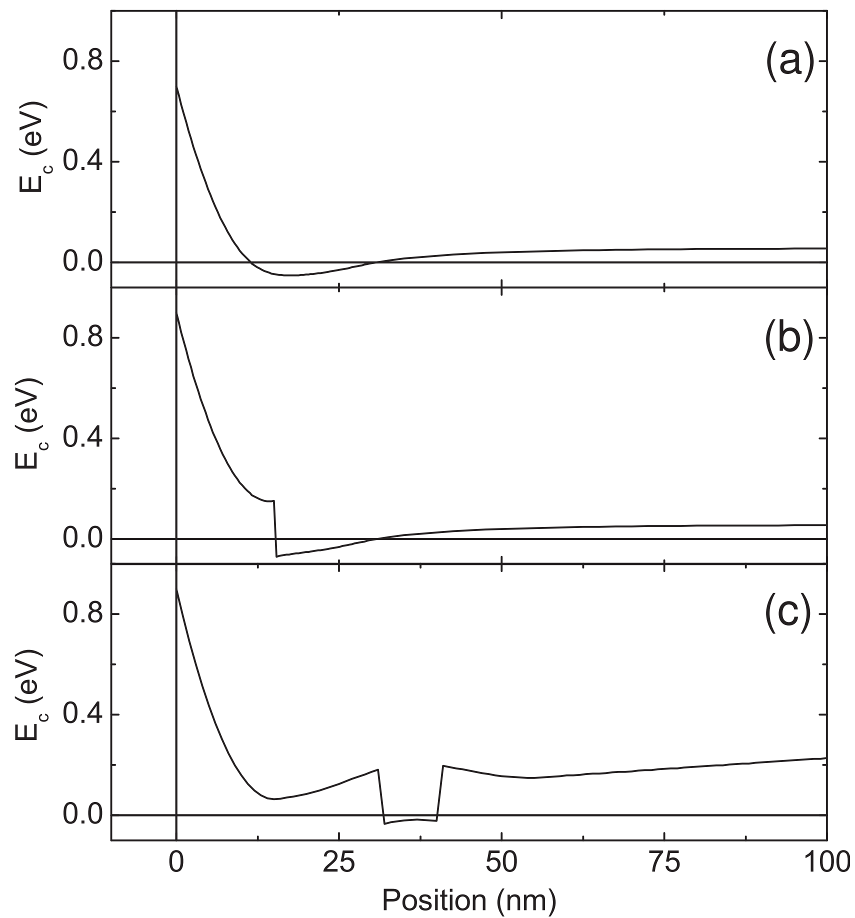

Figure 4.5: (a) Bulk n-GaAs sample with 15 nm highly doped layer and 15 nm transition layer, as discussed in Sec. 1.4.1. (b) Bulk n-GaAs sample with 15 nm highly doped $Al_{0.3}Ga_{0.7}As$ barrier with a 15 nm transition layer. (c) $Al_{0.3}Ga_{0.7}As/GaAs/Al_{0.3}Ga_{0.7}As$ remote doped 2DEG sample. Figure 4.6 lists the detailed sample structure for samples shown in panels (a)-(c).

(a)

Thickness (nm)	material	Doping (cm^{-3})
15	GaAs	5×10^{18}
15	GaAs	5×10^{18} transition 5×10^{16}
2500	GaAs	5×10^{16}
100	GaAs	undoped

(b)

Thickness (nm)	material	Doping (cm^{-3})
15	$Al_{0.3}Ga_{0.7}As$	5×10^{18}
15	GaAs	5×10^{18} transition 5×10^{16}
2500	GaAs	5×10^{16}
100	GaAs	undoped

(c)

Thickness (nm)	material	Doping (cm^{-3})
15	$Al_{0.3}Ga_{0.7}As$	5×10^{18}
10	$Al_{0.3}Ga_{0.7}As$	5×10^{17}
6	$Al_{0.3}Ga_{0.7}As$	undoped
10	GaAs	undoped
6	$Al_{0.3}Ga_{0.7}As$	undoped
10	$Al_{0.3}Ga_{0.7}As$	5×10^{17}
100	$Al_{0.3}Ga_{0.7}As$	undoped

Figure 4.6: Detailed sample structures corresponding to the calculated band diagrams shown in Fig. 4.5. (a) Bulk n-GaAs sample with 15 nm highly doped layer and 15 nm transition layer, as discussed in Sec. 1.4.1. (b) Bulk n-GaAs sample with 15 nm highly doped $Al_{0.3}Ga_{0.7}As$ barrier with a 15 nm transition layer. (c) $Al_{0.3}Ga_{0.7}As$/GaAs/$Al_{0.3}Ga_{0.7}As$ remote doped 2DEG sample.

The fabrication procedure described in Sec. 1.4.1 will need to be modified for the processing of 2DEG samples, primarily because the 2DEG transport layer is quite close to the sample surface. Using Ar ion milling to define the iron contacts would probably destroy the 2DEG layer. It will likely be necessary to use selective wet etching to define the Fe contacts. There is a large body of literature on the selective etching of metals [122, 123]. Solutions of either HCl:H_2O or I_2:KI:H_2O can be used to etch Fe without also etching GaAs.

Figure 4.7 shows both an overhead and cross-sectional view of a proposed device structure to measure spin transport in a 2DEG. Aside from the use of wet etching to define the iron contacts, the processing procedure would be similar to that outlined in Sec. 1.4.1. The shape of the iron contacts has been modified from the device pictured in Fig. 1.5 so that a gate can be defined over the 2DEG channel. An insulating layer of SiN is deposited over the 2DEG channel and the central portion of the Fe contacts. A gate electrode is then deposited over the 2DEG channel when the bonding pads are deposited. The 2DEG can be grown on top a heavily doped n^+ GaAs substrate and insulated from the n^+ layer by an undoped $Al_{1-x}Ga_xAs$ barrier. A voltage can be applied across the 2DEG between the gate electrode and the substrate to vary the strength of the Rashba spin-orbit field. This device geometry could be shrunk significantly if e-beam lithography is used to define the Fe contacts instead of photolithography. Traditional photolithography would still be adequate for all other processing steps. Wet etching of $Al_{1-x}Ga_xAs$ can be made sufficiently slow that it could be used to create 2DEG channels with widths ~ 100 nm. Such a device could potentially be used to study either of the two spin FET designs discussed in Sec. 4.2. If the geometry was modified such that the Fe contacts ran along the edges of the 2DEG channel (similar to Fig. 3.8), it could also be used to study the intrinsic spin Hall effect.

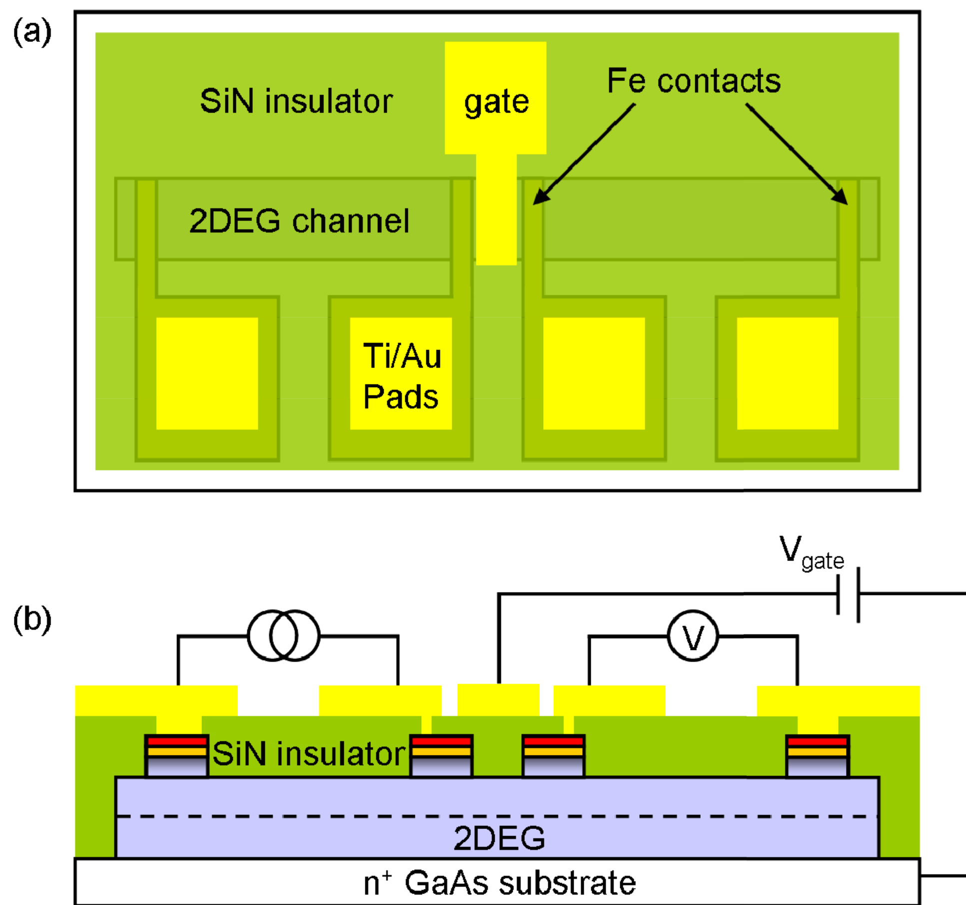

Figure 4.7: (a) Overhead view of proposed 2DEG device. (b) Cross-Sectional view of a proposed 2DEG device.

Chapter 5

Summary

This thesis has presented the results of spin transport measurements on a series of ferromagnet/semiconductor heterostructures using all-electrical measurement techniques. The devices used in these experiments are lateral Fe/$In_xGa_{1-x}As$ heterostructures with highly doped Schottky barriers at the Fe/$In_xGa_{1-x}As$ interface. Two classes of measurements have been performed: non-local spin injection and detection measurements, and electrical measurements of the spin Hall effect. These measurements address questions about the fundamental requirements for the use of the electron's spin degree of freedom in information processing devices.

The measurements presented in Chapter 1 focused on non-local spin injection and detection in Fe/GaAs heterostructures to better characterize the spin-dependent properties of the Fe/GaAs interface. The bias dependence of spin injection was found to be extremely non-linear on all devices studied. The spin accumulation in the GaAs was found to correspond to Fe majority spin electrons under both large forward and large reverse bias. It was found that the spin detection sensitivity of a biased detector electrode could be understood in terms of spin-dependent tunneling at the Fe/GaAs interface and charge transport effects in the GaAs channel. Devices from multiple heterostructures were found to have strikingly similar spin injection and detection properties, despite the fact that bias dependence of spin injection and detection are extremely non-linear.

The extrinsic spin Hall effect was measured electrically in Fe/$In_xGa_{1-x}As$ heterostructures. By fitting the data to a model including diffusion, precession, and relaxation we determined the magnitude of the spin accumulation and the spin lifetime. Both skew scattering and side-jump scattering were found to contribute to the total spin Hall conductivity. We found that the temperature dependence of the spin Hall conductivity can be understood in terms of the temperature dependence of the charge conductivity. The spin-orbit coupling parameter as calculated from both the spin lifetime and the spin Hall conductivity was found to be larger than theoretically predicted for GaAs. Additionally, the spin-orbit coupling parameter increases with increasing In concentration faster than is predicted by the 8×8 Kane model.

Finally, we also discussed intrinsic spin-orbit effects arising from either bulk or structural inversion asymmetry. Although these effects are small in bulk n-GaAs, they have numerous interesting applications in high mobility 2DEGs, including extremely large spin Hall conductivities and the potential for providing a means to manipulate spin polarized electrons to create spin field effect transistors. Order of magnitude calculations showed that a these intrinsic effects could be studied with a gated device structure using lattice matched III-V semiconductor alloys.

References

[1] Semiconductor Industry Association, Tech. Rep., Semiconductor Industry Association, San Jose, CA, http://public.itrs.net. (2009).

[2] S. Datta and B. Das, Appl. Phys. Lett. **56**, 665 (1990).

[3] X. Cartoixà, D. Z.-Y. Ting, and Y. C. Chang, Appl. Phys. Lett. **83**, 1462 (2003).

[4] K. C. Hall and M. E. Flatté, Appl. Phys. Lett. **88**, 162503 (2006).

[5] M. N. Baibich, J. M. Broto, A. Fert, F. N. V. Dau, and F. Petroff, Phys. Rev. Lett. **61**, 2472 (1988).

[6] G. Binasch, P. Grünberg, F. Saurenbach, and W. Zinn, Phys. Rev. B **39**, 4828 (1989).

[7] M. Julliere, Phys. Lett. A **54**, 225 (1975).

[8] G. Schmidt, Phys. Rev. B **62**, 4790(R) (2000).

[9] E. I. Rashba, Phys. Rev. B **62**, 16267(R) (2000).

[10] A. T. Hanbicki, B. T. Jonker, G. Itskos, G. Kioseoglou, and A. Petrou, Appl. Phys. Lett. **80**, 1240 (2002).

[11] J. J. Strand, Ph.D. thesis, School of Physics and Astronomy, University of Minnesota (2004).

[12] J. Moser, A. Matos-Abiague, D. Schuh, W. Wegscheider, J. Fabian, and D. Weiss, Phys. Rev. Lett. **99**, 056601 (2007).

[13] C. Gould, C. Ruster, T. Jungwirth, E. Girgis, G. M. Schott, R. Giraud, K. Brunner, G. Schmidt, and L. W. Molenkamp, Phys. Rev. Lett. **93**, 117203 (2004).

[14] M. Johnson, B. R. Bennett, M. J. Yang, M. M. Miller, and B. V. Shanabrook, Appl. Phys. Lett. **71**, 974 (1997).

[15] M. Johnson and R. H. Silsbee, Phys. Rev. Lett. **55**, 1790 (1985).

[16] F. J. Jedema, A. T. Filip, and B. J. van Wees, Nature **410**, 345 (2001).

[17] F. J. Jedema, H. B. Heersche, A. T. Filip, J. J. A. Baselmans, and B. J. van Wes, Nature **416**, 713 (2002).

[18] S. O. Valenzuela and M. Tinkham, Appl. Phys. Lett. **85**, 5914 (2004).

[19] S. O. Valenzuela, D. J. Monsma, C. M. Marcus, V. Narayanamurti, and M. Tinkham, Phys. Rev. Let **94**, 196601 (2005).

[20] S. Garzon, I. Zutic, and R. A. Webb, Phys. Rev. Lett. **94**, 176601 (2005).

[21] T. Kimura, Y. Otani, and J. Hamrle, Phys. Rev. Lett. **96**, 037201 (2006).

[22] M. V. Costache, M. Zaffalon, and B. J. van Wees, Phys. Rev. B **74**, 012412 (2006).

[23] Y. Ji, A. Hoffmann, J. E. Pearson, and S. D. Bader, Appl. Phys. Lett. **88**, 052509 (2006).

[24] X. Lou, C. Adelmann, S. A. Crooker, E. S. Garlid, J. Zhang, K. S. M. Reddy, S. D. Flexner, C. J. Palmstrøm, and P. A. Crowell, Nature Physics **3**, 197 (2007).

[25] X. Lou, Ph.D. thesis, School of Physics and Astronomy, University of Minnesota (2007).

[26] R. I. Dzhoiev, K. V. Kavokin, V. K. Korenev, M. V. Lazarev, B. Y. Meltser, M. N. Stepanova, B. P. Zakharchenya, D. Gammon, and D. S. Karzer, Phys. Rev. B **66**, 245204 (2002).

[27] X. Lou, C. Adelmann, M. Furis, S. A. Crooker, C. J. Palmstrøm, and P. A. Crowell, Phys. Rev. Lett. **96**, 176603 (2006).

[28] M. K. Chan, Ph.D. thesis, School of Physics and Astronomy, University of Minnesota (2010).

[29] C. Adelmann, X. Lou, J. Strand, C. J. Palmstrøm, and P. A. Crowell, Phys. Rev. B **71**, 121301 (2005).

[30] M. E. Flatte and J. M. Byers, Phys. Rev. Lett. **84**, 4220 (2000).

[31] S. A. Crooker, M. Furis, X. Lou, C. Adelmann, D. L. Smith, C. J. Palmstrøm, and P. A. Crowell, Science **309**, 2191 (2005).

[32] S. A. Crooker, E. S. Garlid, A. N. Chantis, D. L. Smith, K. S. M. Reddy, Q. O. Hu, T. Kondo, C. J. Palmstrøm, and P. A. Crowell, Phys. Rev. B **80**, 041305 (2009).

[33] H. Dery and L. J. Sham, Phys. Rev. Lett. **98**, 046602 (2007).

[34] A. N. Chantis, K. D. Belashchenko, D. L. Smith, E. Y. Tsymbal, M. van Schilfgaarde, and R. C. Albers, Phys. Rev. Lett. **99**, 196603 (2007).

[35] D. L. Smith and R. N. Silver, Phys. Rev. B **64**, 045323 (2001).

[36] M. Furis, D. L. Smith, S. Kos, E. S. Garlid, K. S. M. Reddy, C. J. Palmstrøm, P. A. Crowell, and S. A. Crooker, New Journal of Physics **8**, 347 (2007).

[37] L. H. Thomas, Nature **117**, 574 (1926).

[38] R. Shankar, *Principles of Quantum Mechanics* (Springer, 1994).

[39] N. F. Mott, Proc. R. Soc. London, Ser. A **124**, 425 (1929).

[40] N. F. Mott and H. S. W. Massey, *Theory of Atomic Collisions* (Oxford, 1933).

[41] N. Sherman, Phys. Rev. **103**, 1601 (1956).

[42] J. W. Motz, H. Olsen, and H. W. Koch, Rev. Mod. Phys. **36**, 881 (1964).

[43] H.-A. Engel, B. I. Halperin, and E. I. Rashba, Phys. Rev. Lett. **95**, 166605 (2005).

[44] P. Y. Yu and M. Cardona, *Fundamentals of Semiconductors, 2nd Edition* (Springer, 1999).

[45] E. O. Kane, J. Phys. Chem. Solids **1**, 249 (1957).

[46] J. H. Davies, *The Physics of Low Dimensional Semiconductors* (Cambridge University Press, 1998).

[47] O. Madelung, ed., *Semiconductors-Basic Data* (Springer, New York, 1996).

[48] W. Porod and D. K. Ferry, Phys. Rev. B **27**, 2587(R) (1983).

[49] R. Winkler, *Spin-Orbit Coupling Effects in Two-Dimensional Electron and Hole Systems* (Springer, 2003).

[50] P. A. M. Dirac, Proc. R. Soc. Lond. A **133**, 60 (1931).

[51] L. M. Roth, B. Lax, and S. Zwerdling, Phys. Rev. **114**, 90 (1959).

[52] E. H. Hall, Philos. Mag. **10**, 301 (1880).

[53] A. W. Smith and R. W. Sears, Phys. Rev. **34**, 1466 (1929).

[54] E. M. Pugh and N. Rostoker, Rev. Mod. Phys. **25**, 151 (1953).

[55] C. L. Chien and C. R. Westgate, eds., *The Hall Effect and Its Applications* (Plenum Press, 1980).

[56] A. Perrier, Helv. Phys. Acta **3**, 317 (1930).

[57] J. Smit, Physica **24**, 39 (1958).

[58] L. Berger, Phys. Rev. B **2**, 4559 (1970).

[59] M. I. D'yakonov and V. I. Perel, Phys. Lett. A **35**, 459 (1971).

[60] M. I. D'yakonov, Phys. Rev. Lett. **99**, 126601 (2007).

[61] A. A. Bakun, B. P. Zakharchenya, A. A. Rogachev, M. N. Tkachuk, and V. G. Fleisher, JETP Lett **40**, 1294 (1984).

[62] S. O. Valenzuela and M. Tinkham, Nature **42**, 176 (2006).

[63] F. Meier and B. P. Zakharchenya, eds., *Optical Orientation* (North-Holland, 1984).

[64] P. Hammar, B. R. Bennett, M. J. Yang, and M. Johnson, Phys. Rev. Lett. **83**, 203 (1999).

[65] B. J. van Wees, Phys. Rev. Lett. **84**, 5023 (2000).

[66] A. T. Filip, B. H. Hoving, F. J. Hedema, and B. J. van Wees, Phys. Rev. B **62**, 9996 (2000).

[67] F. G. Monzon, H. X. Tang, and M. L. Roukes, Phys. Rev. Lett. **84**, 5022 (2000).

[68] P. R. Hammar, B. R. Bennett, M. J. Yang, and M. Johnson, Phys. Rev. Lett. **84**, 5024 (2000).

[69] S. Zhang, J. of Appl. Phys. **89**, 11 (2001).

[70] S. Zhang, Phys. Rev. Lett. **85**, 393 (2000).

[71] Y. K. Kato, R. C. Myers, A. C. Gossard, and D. D. Awschalom, Science **306**, 1910 (2004).

[72] J. Wunderlich, B. Kaestner, J. Sinova, and T. Jungwirth, Phys. Rev. Lett. **94**, 047204 (2005).

[73] V. Sih, R. C. Myers, Y. K. Kato, W. H. Lau, A. C. Gossard, and D. D. Awschalom, Nature Physics **1**, 31 (2005).

[74] N. P. Stern, S. Ghosh, G. Xiang, M. Zhu, N. Samarth, and D. D. Awschalom, Phys. Rev. Lett. **97**, 126603 (2006).

[75] S. Matsuzaka, Y. Ohno, and H. Ohno, Phys. Rev. B **80**, 241305(R) (2009).

[76] I. Zutic, J. Fabian, and S. D. Sarma, Rev. Mod. Phys. **76**, 323 (2004).

[77] D. J. Oliver, Phys. Rev. **127**, 1045 (1962).

[78] M. Furis, D. L. Smith, S. A. Crooker, and J. L. Reno, Appl. Phys. Lett. **89**, 102102 (2006).

[79] M. I. D'yakonov and V. I. Perel, Sov. Phys. Solid State **13**, 3023 (1971).

[80] K. H. Goetz, D. Bimberg, G. Jurgensen, J. Selders, A. V. Solomonov, G. F. Glinskii, and M. Razeghi, J. Appl. Phys. **54**, 4543 (1983).

[81] P. Nozieres and C. Lewiner, J. Phys. (Paris) **34**, 901 (1973).

[82] W. K. Tse and S. D. Sarma, Phys. Rev. Lett. **96**, 056601 (2006).

[83] H. Frohlich and B. V. Paranjape, Proc. Phys. Soc. (London) **B69**, 21 (1956).

[84] R. J. Sladek, Phys. Rev. **120**, 1589 (1960).

[85] D. C. Look, D. C. Walters, M. O. Manasreh, J. R. Sizelove, C. E. Stutz, and K. R. Evans, Phys. Rev. B **42**, 3578 (1990).

[86] D. W. Koon and T. G. Castner, Phys. Rev. B **41**, 12054 (1990).

[87] M. Pope and C. E. Swenberg, *Electronic Processes in Organic Crystals and Polymers* (Oxford University, New York, 1999).

[88] J. Sinova, D. Culcer, Q. Niu, N. A. Sinitsyn, T. Jungwirth, and A. H. MacDonald, Phys. Rev. Lett. **92**, 126603 (2004).

[89] J. Schliemann and D. Loss, Phys. Rev. B **69**, 165315 (2004).

[90] J.-I. Inoue, G. E. W. Bauer, and L. W. Molenkamp, Phys. Rev. B **70**, 041303(R) (2004).

[91] B. A. Bernevig and S.-C. Zhang, http://arxiv.org/abs/cond-mat/0412550 (2004).

[92] B. A. Bernevig and S.-C. Zhang, Phys. Rev. B **72**, 115204 (2005).

[93] B. A. Bernevig and S.-C. Zhang, Phys. Rev. Lett. **96**, 106802 (2006).

[94] G. Dresselhaus, Phys. Rev. **100**, 580 (1955).

[95] E. I. Rashba, Sov. Phys. Solid State **2**, 1109 (1960).

[96] H.-A. Engel, E. I. Rashba, and B. I. Halperin, *Theory of Spin Hall Effects in Semiconductors in Handbook of Magnetism and Advanced Magnetic Materials* (John Wiley and Sons Ltd, Chichester, UK, 2007).

[97] K. C. Hall, W. H. Lau, M. E. F. K. Gündoğdu, and T. F. Boggess, Appl. Phys. Lett. **83**, 2937 (2003).

[98] B. J. van Wees, H. van Houten, C. W. J. Beenakker, J. G. Williamson, L. P. Kouwenhoven, D. van der Marel, and C. T. Foxon, Phys. Rev. Lett. **60**, 848 (1988).

[99] P. J. Burke, I. B. Spielman, J. P. Eisenstein, L. N. Pfeiffer, and K. W. West, Appl. Phys. Lett. **76**, 745 (2000).

[100] M. Studer, G. Salis, K. Ensslin, D. C. Driscoll, and A. C. Gossard, Phys. Rev. Lett **103**, 027201 (2009).

[101] H. C. Koo, J. H. Kwon, J. Eom, J. Chang, S. H. Han, and M. Johnson, Science **325**, 1515 (2009).

[102] J. Schliemann, J. C. Egues, and D. Loss, Phys. Rev. Lett. **90**, 146801 (2003).

[103] N. S. Averkiev and L. E. Golub, Phys. Rev. B **60**, 15582 (1999).

[104] N. S. Averkiev, L. E. Golub, and M. Willander, J. Phys.: Condens. Matter **14**, R271 (2002).

[105] R. J. Elliott, Phys. Rev. **96**, 266 (1954).

[106] Y. Yafet, *Solid State Physics, Vol. 14* (Academic, New York, 1963), p. 2.

[107] G. L. Bir, A. G. Aronov, and G. E. Pikus, Sov. Phys. - JETP **42**, 705 (1976).

[108] M. Z. Maialle, E. A. de Andrada e Silva, and L. J. Sham, Phys. Rev. B **47**, 15776 (1993).

[109] M. Ohno and K. Yoh, Phys. Rev. B **77**, 045323 (2008).

[110] Y. Ohno, R. Terauchi, T. Adachi, F. Matsukura, and H. Ohno, Phys. Rev. Lett. **83**, 4196 (1999).

[111] S. Döhrmann, D. Hägele, J. Rudolph, M. Bichler, D. Schuh, and M. Oestreich, Phys. Rev. Lett. **93**, 147405 (2004).

[112] B. A. Bernevig, J. Orenstein, and S.-C. Zhang, Phys. Rev. Lett. **97**, 236601 (2006).

[113] C. P. Weber, J. Orenstein, B. A. Bernevig, S.-C. Zhang, J. Stephens, and D. D. Awschalom, Phys. Rev. Lett. **98**, 076604 (2007).

[114] J. D. Koralek, C. P. Weber, J. Orenstein, B. A. Bernevig, S.-C. Zhang, S. Mack, and D. D. Awschalom, Nature (London) **458**, 610 (2009).

[115] T. Schäpers, V. A. Guzenko, M. G. Pala, U. Zülicke, M. Governale, J. Knobbe, and H. Hardtdegen, Phys. Rev. B **74**, 081301(R) (2006).

[116] P. Lehnen, T. Sch apers, N. Kaluza, N. Thillosen, and H. Hardtdegen, Phys. Rev. B **76**, 205307 (2007).

[117] A. Wirthmann, Y. S. Gui, C. Zehnder, D. Heitmann, C.-M. Hu, and S. Kettemann, Physica E **34**, 493 (2006).

[118] A. W. Holleitner, V. Sih, R. C. Myers, A. C. Gossard, and D. D. Awschalom, New Journal of Physics **9**, 342 (2007).

[119] S. Kettemann, Phys. Rev. Lett. **98**, 176808 (2007).

[120] Y. Kunihashi, M. Kohda, and J. Nitta, Phys. Rev. Lett **102**, 226601 (2009).

[121] D. W. Winston, *Simwindows band structure simulator v1.5.0*, http://www.simwindows.com (1999).

[122] R. E. Williams, *Modern GaAs Processing Methods* (Artech House Publishers, 1990).

[123] J. M. Köhler, *Etching in Microsystem Technology* (Wiley-VCH, 1999).

Appendix A

Details of Spin Transport Device Fabrication

This appendix explains the detailed processing procedure I used to fabricate the spin transport devices studied in this thesis. A general overview of the process is discussed in Chapter 1, Sec. 1.4.1. Spin transport devices were fabricated in the Nanofabrication Center (NFC) at the University of Minnesota using standard semiconductor processing techniques: photolithography, wet etching, dry etching, and thin film deposition.

A.1 Sample Preparation

Before beginning the fabrication process, the 10×20 mm^2 wafers must first be cleaved into a piece of appropriate size; the devices studied in this thesis were approximately 5×5 mm^2.

1. Before cleaving, it is critical to note the [110] direction on the wafer, as the easy axis of the Fe contacts will lie along the [110] direction.

2. Remove any excess indium from the back of the wafer using a razor blade. This will ensure that the sample lies flat, which is critical for achieving good

alignment during the photolithography steps.

3. The wafer can be cleaved very easily along the [110] and [1$\bar{1}$0] directions. To cleave the wafer, make a very light scratch on the surface of the wafer at the desired cleave location using a diamond tipped scribe. Flip the wafer over and apply a slight pressure to the back of the wafer at the location of the scratch. It should take *very* little force to cleave the wafer.

4. Mount the cleaved sample on to a glass slide using mounting wax, which melts at $\approx$ 105 °C. Gently press down on the sample at the corners to ensure it lies flat on the glass slide. Be sure to note the [110] direction.

5. Clean any excess wax using acetone, methanol, and isopropanol solvents, then blow dry with the nitrogen gun. Bake the sample at 115 °C for 2 minutes to evaporate any solvents left on the sample. In the remainder of this appendix, I will refer to this step as a Solvent Clean.

A.2 Details of the Device Fabrication Procedure

I. Define Fe contacts:

   1. Spin Hexamethyldisilazane (HMDS) on the sample at 4000 rpm for 20 seconds. HMDS is used to prime the sample surface and enhance the photoresist bonding with the sample surface.

   2. Spin Shipley 1813 photoresist (PR) on the sample at 4000 rpm for 30 seconds. This results in a PR thickness of ≈ 1 μm.

   3. Bake the sample at 115 °C for 2 minutes.

   4. Put the aligner into soft contact mode, set the alignment gap to 35 μm, and set the exposure time to 5 seconds. Load and align the sample so that the [110] direction will be parallel to the long axis of the Fe contacts, then expose the sample. The exposure

time required depends on the resist thickness, and it may need to be adjusted slightly.

5. Develop the sample using a mixture of Shipley Micro Dev and deionized water (DI H_2O) with a 1:1 ratio. The developing time is ≈ 30 seconds, but can vary slightly with exposure time. Rinse the sample with DI water for 30 seconds, then blow dry with the nitrogen gun.
6. Bake the sample at 120 °C for 2 minutes. Steps 1 through 6 represent a complete photolithography cycle, which transfers a pattern from a mask to the photoresist on the sample. In the remainder of this appendix, I will use Photolithography to refer to these steps.
7. Use Kapton tape on the corners of the samples to affix the samples to the glass slides, then use tape to mount the glass slides in to the Ar ion mill. It is necessary to tape the samples to the glass slides because the sample temperature may rise high enough to melt the mounting wax.
8. Etch through the Au and Al capping layers, the Fe layer, and the highly doped layer using the Ar ion mill. The etch time required depends on several factors, including the layer thicknesses and the ion beam current. Using a beam current of ≈ 100 mA, a 30 minute etch at an angle of 20°, followed by a 5 minute etch at 60°, should be adequate to etch through the necessary layers. The 5 minute etch at 60° removes any fencing effects from the 30 minute etch. It is important to etch all the way through the highly doped layer. It is not problematic if $\lesssim 100$ nm of the n-GaAs channel is also etched away.
9. Remove the baked on photoresist using the O_2 clean program in the STS etcher; a 30 minute O_2 clean should remove all of the

photoresist.

II. Define n-GaAs channel:

1. Perform Photolithography to transfer the GaAs mesa pattern to the sample.
2. Measure the height of the PR using the Dektak.
3. Mix NH_4OH:H_2O_2:DI H_2O at a ratio of 1:1:100 to use as the GaAs etchant. This mixture will etch GaAs at ≈ 0.15 μm per minute, although the etch rate will decrease the longer the mixture is exposed to air. (Note: This mixture will also etch $In_xGa_{1-x}As$ for low concentrations of In ($x \lesssim 0.05$), although the etch rate will be slower. To etch $In_xGa_{1-x}As$ with higher concentrations of In, use H_2SO_4:H_2O_2:DI H_2O mixed at a ratio of 1:1:100. The etch rate will depend on the In concentration; for $x \lesssim 0.10$ the etch rate is ≈ 0.10 μm per minute.
4. Put the samples in the etchant solution for approximately 10 minutes, then remove the samples and rinse them in DI water for 1 minute.
5. Measure the height of the mesa and photoresist. Subtract the previously measured height of the photoresist to estimate the mesa height. Calculate the estimated etch time required to etch completely through the n-GaAs layer.
6. Put the samples back in the etchant solution for the time calculated. When the etch is finished, rinse the samples in DI water for 1 minute.
7. Measure the height of the mesa and photoresist in the Dektak again. Calculate the mesa height. If more etching time is required, put the samples back in the etchant solution. If the etch

is finished, remove the photoresist from the samples by doing a Solvent Clean.

8. Measure the final mesa height using the Dektak. Also measure the height of the Fe contacts, so that the total thickness of the n-GaAs channel can be calculated.

III. Define SiN insulator:

1. Perform Photolithography to transfer the SiN pattern to the sample. Because the SiN deposition is isotropic, lift-off can sometimes be problematic. For this step, it is recommended to spin a double layer of Shipley 1818 PR at 3000 rpm rather than a single layer of 1813 PR at 4000 rpm. The first layer of 1818 will help to planarize the surface of the sample. The second layer of 1818 will ensure that there the PR thickness is at least 1.8 μm across the surface of the sample. The UV exposure time will need to be lengthened to $\approx$ 20 seconds to ensure the resist is fully exposed. There are no critically small features in the SiN step, so overexposing certain portions of the resist is not a concern.
2. Deposit the SiN layer using the SiN100 process in the PECVD. Let the deposition step of the process run for 10 minutes. This results in a $\approx$ 200 nm thick SiN layer.
3. Lift-off the excess SiN and PR using 1165 photoresist stripper. Put the samples in beakers of 1165 heated to 90 °C on a hot plate in a fume hood. The 1165 may dissolve the mounting wax, so each sample should be placed in its own beaker to avoid any confusion. Leave the samples in the 1165 for 10 minutes.
4. Sonicate the samples for 1-2 minutes to lift-off the unwanted SiN.
5. Remove any residual 1165 by doing a Solvent Clean

6. Check the sample under the microscope to ensure that the lift-off procedure successfully removed all the unwanted SiN. If unwanted SiN still remains, return to step 3.
7. If the samples were dismounted during the lift-off process, re-mount and clean the samples.

IV. Define Au leads and bonding pads:

1. Perform Photolithography to transfer the Ti/Au bonding pad pattern to the sample. The Ti/Au is deposited using the lift-off fixture in one of the e-beam evaporators. The Ti/Au is nearly normally incident on the sample surface, so lift-off is usually much easier than the SiN lift-off. To achieve small feature sizes, it is therefore recommended to use a single layer of 1813 spun at 4000 rpm.
2. After the final bake of the PR, put the samples in the STS etcher and run the O_2 clean program for 30 seconds. This will remove any residual PR over the Fe contacts, which will ensure good electrical contact between the Fe contacts and the Ti/Au bonding pads.
3. Use Kapton tape on the corners of the samples to tape the samples to the glass slides, then load the samples into one of the e-beam evaporators. Be sure to use the lift-off fixture. It is necessary to tape the samples to the glass slides because the sample temperature may rise high enough to melt the mounting wax.
4. Deposit 10 nm Ti and 100 nm Au.
5. Lift-off the excess Ti/Au using 1165 photoresist stripper. Put the samples in beakers of 1165 heated to 90 °C on a hot plate in a fume hood. The 1165 may dissolve the mounting wax, so each

sample should be placed in its own beaker to avoid any confusion. Leave the samples in the 1165 for 10 minutes.

6. Sonicate the samples for 1-2 minutes to lift-off the unwanted Ti/Au.
7. Remove any residual 1165 by doing a Solvent Clean
8. Check the sample under the microscope to ensure that the lift-off procedure successfully removed all the unwanted Ti/Au. If unwanted Ti/Au still remains, return to step 5.
9. Take pictures of all of the contacts using a microscope.

Once the samples have been fabricated, they should be stored under vacuum until they are going to be measured.

Appendix B

Glossary

B.1 List of Abbreviations

Table B.1: List of Abbreviatons

Abbreviation	Meaning
2DEG	Two Dimensional Electron Gas
3T	Three Terminal
AC	Alternating Current
AHE	Anomalous Hall Effect
$Al_xGa_{1-x}As$	Aluminum Gallium Arsenide
AMR	Anisotropic Magneto-resistance
DC	Direct Current
DI	Deionized
DOS	Density of States
dSHE	Direct Spin Hall Effect
FM	Ferromagnet
FWHM	Full-Width at Half Maximum
GaAs	Gallium Arsenide

Continued on next page

Table B.1 – continued from previous page

Abbreviation	Meaning
GMR	Giant Magneto-resistance
HCl	Hydrochloric Acid
HMDS	Hexamethyldisilazane
H_2O_2	Hydrogen Peroxide
$In_xAl_{1-x}As$	Indium Aluminum Arsenide
InAs	Indium Arsenide
$In_xGa_{1-x}As$	Indium Gallium Arsenide
iSHE	Inverse Spin Hall Effect
IV	Current vs. Voltage Measurement
KI	Potassium Iodide
MOSFET	Metal-Oxide-Semiconductor Field Effect Transistor
NH_4OH	Ammonium Hydroxide
NM	Normal Metal
NL	Non-Local
NLSV	Non-local Spin Valve
PECVD	Plasma Enhanced Chemical Vapor Deposition
PPMS	Physical Property Measurement System
PR	Photoresist
QW	Quantum Well
SC	Semiconductor
SHE	Spin Hall Effect
SiN	Silicon Nitride
Spin-FET	Spin Field Effect Transistor
Spin-LED	Spin Light Emitting Diode
TAMR	Tunneling Anisotropic Magneto-resistance
TMR	Tunneling Magneto-resistance

B.2 List of Symbols

Table B.2: List of Symbols

Symbol	Definition
$\uparrow$ ($\downarrow$)	Up(down) spin band
$T(E)$	Tunneling probability at energy E
$N(E)$	Density of states at energy E
$f(E)$	Fermi-Dirac distribution at energy E
V_b	Bias voltage
e	Fundamental charge
$\mathbf{j}$	Charge current density vector
H_{exch}	Exchange Hamiltonian
J	Exchange coupling constant
$\mathbf{S}$	Electron spin vector
n	Density of electrons or doping concentration
d	Tunnel barrier thickness or quantum well thickness
ϵ	Dielectric constant
ϕ_B	Barrier height
ρ_{FM}	Resistivity of a ferromagnet
ρ_{SC}	Resistivity of a semiconductor
ρ_{sf}	Spin-flipping resistivity
$q_{i,j}$	Spin current density flowing in the i dir. of spins in the j dir.
v_d	Drift velocity
L_s	Spin diffusion length
D	Diffusion constant
τ_s	Spin lifetime
n^+	Heavily doped
B_{sat}	Hard axis saturation field

Continued on next page

Table B.2 – continued from previous page

Symbol	Definition
M_s	Saturation magnetization
$\mathbf{B}$	Magnetic field vector
B_x,B_y,B_z	The $\hat{x}$, $\hat{y}$, and $\hat{z}$ components of magnetic field $\mathbf{B}$
η	Zero bias spin detection sensitivity
P_{Fe}	Spin polarization of Fe
P_{SC}	Spin polarization in semiconductor
E_F	Fermi energy
$\Delta\mu$	Electrochemical potential shift
V	Voltage
$V_{\uparrow\uparrow}$	Voltage in the parallel magnetization state
$V_{\uparrow\downarrow}$	Voltage in the anti-parallel magnetization state
V_{NL}	Non-local voltage
V_d	Detector bias voltage
V_{int}	Voltage drop at the Fe/GaAs interface
V_{3T}	3T voltage signal
ΔV_i	Spin dependent voltage in measurement configuration i
$\hbar$	Plank's constant
m_0	Electron rest mass in the vacuum
m^*	Effective mass of conduction band electrons
g_0	Electron g-factor in the vacuum
g^*	Effective g-factor of conduction band electrons
μ_B	Bohr Magneton
$\mathbf{\Omega}_L$	Larmor precession frequency
$P(t)$	Probability distribution of the spin arrival time t
t	Spin arrival time
L	Separation between injector and detector
$B_{1/2}$	Full width at half maximum of a Hanle curve

Continued on next page

Table B.2 – continued from previous page

Symbol	Definition
S_0	Spin injection rate
k	Electron wavevector
$k_\uparrow$	Electron wavevector for spin up electrons
$k_\downarrow$	Electron wavevector for spin down electrons
$n_\uparrow$	density of spin up electrons
$n_\downarrow$	density of spin down electrons
$G_\uparrow$	Interface tunnel conductance for spin up electrons
$G_\downarrow$	Interface tunnel conductance for spin down electrons
$j_\uparrow$	Spin up charge current
$j_\downarrow$	Spin down charge current
P_j	Current spin polarization
p_i	Polarization density of spins pointing in the i direction
μ	Electron mobility
$\mathbf{E}$	Electric field
H	Hamiltonian
$\mathbf{p}$	Momentum vector
$\Phi(r)$	Electric potential at position r
$\mathbf{v}$	Velocity vector
$\mathbf{B}_{SO}$	Effective spin-orbit magnetic field
c	Speed of light in the vacuum
H_{SO}	Spin-orbit Hamiltonian
$V(r)$	Potential energy at position r
$\boldsymbol{\mu}_s$	Magnetic moment of the electron
$\mathbf{L}$	Orbital angular momentum of the electron
$\boldsymbol{\sigma}$	Pauli spin matrix
λ_{SO}^{eff}	Effective spin-orbit coupling parameter
λ_{SO}^{i}	Effective spin-orbit coupling parameter in material i

Continued on next page

Table B.2 – continued from previous page

Symbol	Definition
Z	Atomic number
Ψ	Wavefunction
$\mathbf{F}$	Force vector
I	Scattering intensity
$S(\theta)$	Sherman function
$E_n(\mathbf{k})$	Energy as a function of wavevector $\mathbf{k}$ for band n
$\mathbf{P}_{nn'}$	Optical matrix element between band n and n'
E_g	Energy gap between the valence and conduction bands
Δ_{SO}	Energy splitting of the split-off hole band
Δ_A	Atomic spin-orbit splitting of the cation in a binary SC
Δ_B	Atomic spin-orbit splitting of the anion in a binary SC
ξ	Dimensionless parameter equal to $\Delta_{SO}/(E_g + \Delta_{SO})$
f_i	ionicity
ρ_{AH}	Anomalous Hall resistivity
ρ_{xy}	Hall resistivity
ρ_{xx}	Longitudinal resistivity
R_0	Ordinary Hall constant
R_S	Anomalous Hall constant
$\mathbf{M}$	Magnetization vector
M_x,M_y,M_z	The $\hat{x}$, $\hat{y}$, and $\hat{z}$ components of $\mathbf{M}$
T	Temperature
T_c	Curie temperature
σ_{AH}	Anomalous Hall conductivity
σ_{xx}	Longitudinal conductivity
γ_{AH}	Anomalous Hall angle
γ_{SS}	Skew scattering angle
γ_{SJ}	Side-jump scattering angle

Continued on next page

Table B.2 – continued from previous page

Symbol	Definition
L_p	Electron mean free path
ρ_{SJ}	Side-jump contribution to anomalous Hall resistivity
σ_{SJ}	Side-jump contribution to anomalous Hall conductivity
γ	Phenomenological spin-orbit angle
A	Kerr Rotation
R_{SC}	Resistance of semiconductor
$R_{Schottky}$	Resistance of Schottky barrier
w	Channel width
$\mathbf{B}_{int}(\mathbf{k})$	Intrinsic spin-orbit magnetic field at wavevector **k**
Ω_{av}	Average spin precession frequency about $\mathbf{B}_{int}(\mathbf{k})$
τ_p	Momentum scattering time
γ_3	Dimensionless parameter related to scattering mechanism
α	Dimensionless parameter proportional to spin-orbit coupling
m^*_{cv}	Effective mass coupling 8×8 bands to 14×14 bands
P_0	Spin polarization at sample edge in dSHE measurement
σ_{SH}	Spin Hall conductivity
a^*_B	Effective Bohr radius
α^*	Renormalized fine structure constant
c^*	Renormalized velocity used in α^*
σ_{SS}	Skew scattering contribution to the spin Hall conductivity
T_e	Electron temperature
T_L	Lattice temperature
δ	Dimensionless parameter equal to $(T_e - T_L)/T_L$
z	Dimensionless constant defined by $\tau_p \propto E^z$
E	Energy
μ_L	Lattice mobility
s	Speed of sound

Continued on next page

Table B.2 – continued from previous page

Symbol	Definition
E_b	Donor binding energy
H_D	Dresselhaus spin-orbit Hamiltonian
β	Dresselhaus spin-orbit parameter
$H_{D,2D}$	Dresselhaus spin-orbit Hamiltonian in 2 dimensional limit
β_{2D}	Dresselhaus spin-orbit parameter in 2 dimensional limit
H_R	Rashba spin-orbit Hamiltonian
α_R	Rashba spin-orbit parameter
L_{SO}	Spin-orbit length